Design and Optimisation of Radio-Frequency Probes for High Field Magnetic Imaging

by

Amany Ali Alsuraihi

Abstract

This thesis addresses the in-homogeneity and the high SAR values associated with the state-of-art 7T high field MR system. The high signal to noise ratio associated with such high field systems $\geq$ 7 T is a continuous driver to use such systems where high resolution images are acquired at short acquisition time. However, these systems come with many challenges. The central brightening effect in MR images indicates a B_1 degraded field uniformity. For example, at 7 T with an operational electromagnetic frequency of 298 MHz the wavelength is about 12 cm in tissues. At such short wavelengths, circuit and electromagnetic theory will be invalid an analytical solution and is no longer feasible to predict magnetic field distribution.

In this thesis the full wave method, Transmission Line Modelling (TLM) technique is used in conjunction with Tikhonov regularisation inverse method in order to optimise phases and amplitude of elementary drive currents of four different coils for optimal uniformity and low SAR values. Two dimensional 8 and 16 rungs birdcage-like coils were first optimised. Then the optimisation was carried out for the three dimensional problem for 8 and 16 rungs birdcage-like coils and then compared to 32 and 64 multi-element coils.

The travelling wave approach is a recent approach to over come field in-homogeneity and high SAR values. An Antenna is used to couple head/body to a travelling wave RF signal. Using Finite Difference Time Domain (FDTD) method, a patch antenna has been designed, and the effect of using matching load for maximising the power flow in the magnet bore, field uniformity and reducing SAR values in the head have been explored. An end tapered waveguide has been designed for local imaging and tested on the 7 T philips Acheiva system. Further developments have been suggested for the end tapered waveguide by suggesting the design of a dielectric transformer. It is envisaged that the waveguide approach is ideally suited for a multi-transmit system which would employ a number of waveguide ports.

Acknowledgements

First of all, all praise and thanks are due to Allah, and peace and blessings be upon his messenger. This research project would not have been possible without the support of many people. It is a pleasure to convey my gratitude to them all in my humble acknowledgement.

To my parents thank you very much for having confidence in me, and for the love you show me, the support, and the encouragement. I invoke Allah Almighty to enlighten my heart to accept the truth and to grant me success both in this world and on the day of judgement. To Aiman, my dearest brother, my partner in crime and my companion during the years of study in Nottingham words of thanks and gratitude would not be enough to express how much I am grateful to you. My appreciation is extended to all my sisters and brothers for their support and encouragement.

A very special thanks goes out to Dr Paul Glover, for his support and supervision throughout this research project and for his openness to ideas and encouragement to shape my own interest and ideas. I would like to thank professor Trevor Benson and Dr Ana Vukovic for providing the TLM in-house code that I used in a part of this research project. My deepest gratitude goes to my former colleague Arthur Magill for his help and unconditional support and for adjusting the TLM in-house code to be MRI compatible. I would also like to show my gratitude to my colleague Daniel Lee (Dan) for his help and support during the last two years and for editing parts of my thesis.

I am indebted to my office mates and friends for providing a stimulating and fun environment, especially, Devasuda Anblagan, Anna Blazejewska, Lin Yan (Yana), Olivier Mougin, Andreas Bungert, Daniel Lee, Waldemar Senczenko, Rosa Sanchez, Elisa Placidi, Anniek Van Der Drift, Gera Bjrk Grmnisdttir, Andre Antunes and Samia Aboushoushah. My gratitude also goes to Peter Roberts and Aaron Hurley for editing chapters from my thesis.

Contents

Chapter 1

Introduction

The Magnetic Resonance Imaging (MRI) technique is considered to be one of the most used methods in medical diagnosis. It has its origin in the physical phenomena Nuclear Magnetic Resonance (NMR). The concept of NMR is based on the magnetic properties of nuclei where the angular momentum vector and magnetic momentum vector interact with the magnetic fields and give rise to the NMR phenomena. The theoretical basis of NMR was formulated during the 1920's when Compton [1] first described the behaviour of the electron as a tiny gyroscope, and then in 1924 with Pauli [3] who postulated the nuclear spin and magnetic moment properties. In the 1930's, scientists started their first attempts to build spectrometers to detect NMR. In 1952, Bloch and Purcell [4] shared the Nobel Prize, for their contribution to NMR. In 1946, they independently detected the NMR signal in water and Paraffin wax, respectively. Since then NMR has become a powerful analytical tool for Chemists and Spectroscopists. However, it was not until the 1970's that NMR become used in imaging. In 1973, Laurterbur and Mansfield [2] developed techniques to generate images of samples using the NMR, since then the term Magnetic Resonance Imaging (MRI) has been used.

Magnetic Resonance Imaging (MRI) has become the driving force for technol-

ogy development in every aspect in the system. There is always a demand for better and accurate images. In the magnetic resonance system, the main magnet supplies the static field which define the axis about which the nuclei precess as well as its use as a reference for the nutation angle of the protons following the application of RF pulse. A range of field strengths have been used for imaging originally 0.1 T but now systems operate at fields strength up to 3T in clinical imaging. System operating at higher magnetic field strength (up to 10 T) are used in research centres. It is argued that the higher the magnetic field strength the better the image as the signal to noise ratio (SNR) will be improved if the engineering challenges that come with such high fields is overcome. Increasing the static magnetic field strength increases the operating frequency of the RF transmitter coil that is necessary to achieve the resonance. The physical size of the biological tissue under investigation becomes comparable to the RF wavelength and the field focusing effect results in field inhomogeneity. There are also the heating effects that are associated with the high RF fields. Therefore, one of the main challenges in the state-of-art high field MRI systems is to design RF coils that are capable of producing a rotating RF field that can be used to acquire high SNR images without exceeding the specific absorption rate (SAR) limits.

The tissue-RF field interactions have been demonstrated and also predicted numerically. With innovation in computer modelling and simulation techniques one can predict the behaviour of such complex systems as well as suggest appropriate design solutions, using suitable optimization techniques.

1.1 Scope of this Thesis

This thesis discusses the feasibility of improving the transmit field homogeneity and reducing the SAR level 298 MHz, the resonant frequency for protons in

at 7 T system. The central brightening artefact is caused by constructive and destructive interference due to the phase shift from multiple elements transmitted in to tissues. Dielectric resonance can also occur in which incident waves interfere with reflected waves at tissues' boundaries with high dielectric properties although the effect is degraded by high electric conductivity. This in turn affects the $|B_1^+|$ homogeneity and therefore the flip angle will vary across tissues. One way to overcome such effect is to independently control the transmit elements' phases and amplitude, RF Shimming. Another way to reduce such artefact is by using the travelling wave MRI devices to excite RF field in the 7 T magnet bore.

Two full wave electromagnetic techniques have been used in this work to model the RF field-tissue interaction. These are the Transmission Line Matrix (TLM) method and the Finite Difference Time Domain (FDTD) method. The TLM method was used in combination with an inverse optimisation technique, Tikhonov regularisation, for determining the RF volume coil shimming. The FDTD method was used to investigate travelling wave MRI approach.

Chapter two introduces the theory of nuclear magnetic resonance and magnetic resonance imaging principles. The chapter ends with a brief review of the MRI system.

Chapter three starts with a discussion of the reciprocity concept in MRI. Then, the LCR circuit concept is described followed by a review of the important parameters for RF probes. Signal to noise ratio and RF field losses are discussed and finally different types of RF coils are described.

At high magnetic field strength 3T, the quasi-static analysis breaks down and it is no longer feasible to determine either the resonant frequency of the probe nor the magnetic field pattern in biological tissues. Chapter four describes two basic full wave methods used in designing RF coils and calculating the field-tissue interactions at such high frequencies. The first method described is the

Finite Difference Time Domain (FDTD) method, the second is the transmission line matrix technique (TLM). The material properties changes, wavelength and penetration depth at high frequencies, as well as the central brightening is also discussed in the chapter. In-house designed TLM code is first used to model a 2D birdcage-like coil loaded with a 2D head slice model. The coil was operated at 64, 128, 171, 256 MHz in linear and quadrature modes. The $|B_1^+|$ field maps, field inhomogeneity and SAR maps were all calculated for the two excitation modes.

Chapter five introduces inverse problems and describes the regularisation technique as a potential solution. In order to optimise the $|B_1^+|$ homogeneity and achieve a uniform flip angle, the Tikhonov regularisation technique was used to determine the optimal drive currents' phases and amplitudes for $|B_1^+|$ shimming. This chapter is divided into two parts: the first part is 2D optimisation for 8 and 16 rungs birdcage-like coil. The second part is 3D optimisation of four coils: 8 rungs birdcage-like coil, 16 rungs birdcage-like coil, 32 and 64 multi-element coils. This is carried out for four different head slices then the optimisation is carried further to cover a large volume using four different neighbouring slices in the brain.

The Finite Difference Time Domain FDTD method (using xFDTD Remcom. commercial software) is used in chapter six in order to investigate the travelling wave MRI approach where the body, magnet bore and excitation travelling wave device is needed to be modelled. The transmit $|B_1^+|$ fields are coupled to body/head tissues through the magnet bore TE_{11} mode. It is believed that such set up improves the field uniformity. However, there are issues to overcome, such as, matching the antenna (travelling wave) to the head and the high demand for amplifier power. In this chapter, a patch antenna has been designed and the effect of different matching loads is studied. In addition, an end tapered wave guide is designed and tested on the 7 T system, and further

---

Chapter 2

Principles of Magnetic Resonance Imaging

2.1 Introduction

This chapter introduces the basics of Nuclear Magnetic Resonance theory. Firstly, an outline of the quantum mechanical description and its analogy in classical mechanics is drawn. Secondly, the application of the phenomena in imaging and the process of image formation is described; including spatially encoding the image after slice selection, and using frequency and phase encoding of the MR data. Finally, the MR system hardware is described.

2.2 Spin Angular Momentum

The physics of Nuclear Magnetic Resonance (NMR) is based on the concept that sub-atomic particles with their associated angular momentum and magnetic moment give rise to spin from a microscopic point of view. Spins can be visualised as spheres of distributed charge rotating about their own axis. The small current resulting from this spinning motion produces a small mag-

netic field called a "magnetic moment" μ. The magnitude of the spin angular momentum is

$$|\bar{P}| = \hbar\sqrt{I(I+1)}, \tag{2.1}$$

where I is the spin quantum number and $\hbar$ is Plank's constant divided by 2π and is equal to $6.626068 \times 10^{-34} m^2 kg/s$. The spin quantum number I is either a multiple of an integer or half integer and there are $(2I+1)$ sub-levels for particles with spin I. In the presence of an electric or magnetic field each sub-level has a different energy. The direction of orientation of the spin represents the spin state of the nucleus and is given by m_l, where

$$m_l = I, (I-1), \ldots, 0, \ldots, -I \quad for\, integer\, spin;$$
$$m_l = I, (I-1), \ldots, \frac{1}{2}, -\frac{1}{2}, \ldots, -I \quad for\, half\, integer\, spin. \tag{2.2}$$

The z-component of spin angular momentum is given as

$$P_z = \hbar m_l. \tag{2.3}$$

On a macroscopic scale only nuclei that have an odd number of protons or neutrons, or both, can exhibit a magnetic moment, such as, ^1H, ^2H, ^{31}P, ^{23}Na, ^{17}O or, ^{13}C. The ^1H, ^{31}P or, ^{13}C elements are the most used commonly in NMR experiments as they have half spin and, are naturally abundant. ^{23}Na, ^{17}O have net spin of 3/2 and 5/2. Figure 2.1 shows the vector representation of a spin angular momentum vector. The nuclear magnetic moment is related to the spin angular momentum by the gyromagnetic ratio γ which is in turn related to the intrinsic properties of the nuclear isotope and is given as

$$\vec{\mu} = \gamma\vec{P}. \tag{2.4}$$

For example, the most imaged nucleus in MRI, ^1H , has a gyromagnetic ratio of 42.58 MHz/T.
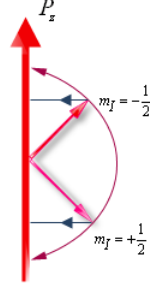
Figure 2.1: *Z-Component of Angular Momentum Vector*

2.3 Energy State "Zeemann Splitting"

In the absence of any magnetic field the proton's magnetic moments tend to align randomly within the sample. Applying a static magnetic field B_0, by convention in the z-direction, causes splitting of the degeneracy of the energy state of the nuclei to $2I+1$ states, which is the well known Zeemen effect. The work done rotating the dipoles in the B_0 field is

$$E = -\mu.B_0, \tag{2.5}$$

and for the longitudinal component,

$$E = -\gamma P_z B_0 = -\gamma \hbar m_l B_0. \tag{2.6}$$

For any spin 1/2 system, there are only two possible energy states, $E_{\pm 1/2}$ which are given as

$$E_{\pm 1/2} = \pm \frac{\gamma}{2} \hbar B_0. \tag{2.7}$$

A transition between energy levels occurs due to absorption or emission of energy equal to the energy difference between them.

$$\Delta E = \hbar \omega = |\gamma \hbar B_0 \Delta m_l|. \tag{2.8}$$

For a spin $1/2$ system, equation 2.8 reduces to

$$\Delta E = \hbar\omega = |\gamma\hbar B_0|, \tag{2.9}$$

thus,

$$\omega = \gamma B_0. \tag{2.10}$$

A transition between energy levels by absorption or emission occurs only at this frequency called the Larmor frequency, as shown by figure 2.2. In other words, when a spin $1/2$ system is irradiated by electromagnetic energy at(the preccesion frequency) the Larmor frequency, the resonance condition is met for absorption or emission.
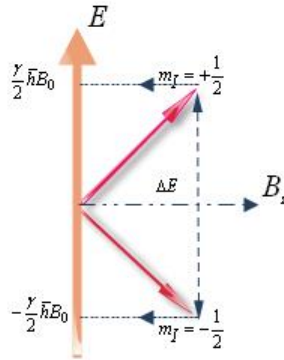
Figure 2.2: *Energy states for spin $1/2$ system*

2.4 Longitudinal Magnetization Vector

In the presence of a static magnetic field, it is usual to deal with the macroscopic magnetic properties of the sample associated with the net number of the

many individual spins within the sample, referred to as the net magnetization. Therefore, for electromagnetic waves to be absorbed or emitted there must be a population difference between the upper and lower spin states. At thermal equilibrium, the spin distribution amongst the upper state, $m_I = -1/2$, designated as $n\uparrow$ and lower state, $m_I = +1/2$, designated as $n\downarrow$ is given by the Boltzmann distribution as

$$\frac{n\downarrow}{n\uparrow} = \exp(\Delta E/kT) = \exp(-\gamma\hbar B_0/kT),\tag{2.11}$$

where k is Boltzmann constant and T is the absolute temperature. If the total number of spins n is $(n\downarrow + n\uparrow)$, then the population difference is given as

$$n\uparrow - n\downarrow = n\frac{1 - \exp(-\gamma\hbar B_0/kT)}{1 + \exp(-\gamma\hbar B_0/kT)} = n\tanh(\gamma\hbar B_0/2kT).\tag{2.12}$$

The net magnetization is destroyed as temperature increases. However, the MR signal can be increased by enhancing the net magnetization through increasing the static magnetic field as shown by Curie's law (for large T)

$$M = C.\frac{B_0}{T},\tag{2.13}$$

where M is the sample magntization and C is the Curie constant.

2.5 Classical Description of Nuclear Magnetization

Although the quantum mechanical description for spins is accurate, the classical description of the bulk magnetization is of great benefit in magnetic resonance studies. The spin magnetization vector $\vec{M}$ experiences a torque as a result of the applied magnetic field $\vec{B}$. This will cause the precession of the magnetization about the applied magnetic field direction in a motion characterised by the Bloch equation

$$\frac{d\vec{M}}{dt} = \gamma\vec{M} \times \vec{B}.\tag{2.14}$$

For a uniform static magnetic field applied in the conventional z direction $\vec{B} = B_0\hat{z}$, equation 2.14 can be broken into three scalar components

$$\frac{dM_x}{dt} = \gamma M_y B_0,$$
$$\frac{dM_y}{dt} = -\gamma M_x B_0, \tag{2.15}$$
$$\frac{dM_z}{dt} = 0.$$

The solutions to these equations are

$$M_x(t) = M_x(0)cos\omega t + M_y(0)sin\omega t,$$

$$M_y(t) = -M_x(0)sin\omega t + M_y(0)cos\omega t, \tag{2.16}$$

$$M_z(t) = -M_z(0).$$

When the system is in thermal equilibrium, under the influence of the static magnetic field B_0 in the z direction, the net magnetization M_0 established by the spins points in the z-direction. This is denoted M_z and is a result of the population difference between the two spin states. There will be no transverse magnetization components as the spins precess with random phases and therefore cancel each other out, leaving only the M_z component.

2.6   Rotating RF field

The application of an RF field oscillating at the same frequency as that of the magnetization vector is a requirement for all MRI experiments. In a quantum mechanical analogue, the electromagnetic radiation of the RF field causes a transition between the two spin states of the sample and therefore absorption and emission can be observed. In a second, equivalent analogue, the resonance condition of the system can be described classically as a result of a torque. The tipping of spins (magnetization) can be easily visualized by considering a rotating frame of reference $(\acute{x}, \acute{y}, \acute{z})$. In this frame, the magnetization and B_1 vectors appears stationary. The $\acute{z}$ component of the magnetization vector is assumed to be stationary, so that $z = \acute{z}$, and the direction of rotation of the
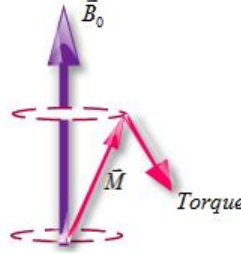
Figure 2.3: *The tipping of the magnetization vector by the application of the B_1 field*

frame is considered to be in a left-hand direction following the magnetization vector. $\acute{x}, \acute{y}$ are related to the laboratory frame of reference as

$$\acute{x} = \hat{i}cos\omega t - \hat{j}sin\omega t,$$
$$\acute{y} = \hat{i}sin\omega t + \hat{j}cos\omega t,$$
(2.17)

where ω is the angular frequency of the frame. In the special case of the frame rotating with frequency equal to the Larmor frequency of the sample, $\omega = \gamma B_0$, then the magnetization vector will appear stationary. Applying an oscillating RF B_1 field, polarized in the x-direction by convention, gives an effective vector around which the magnetization vector precesses, as shown in figure 2.4 and figure 2.5,

$$B_{eff} = \hat{k}(B_0 - \frac{\omega}{\gamma}) + \hat{i}\frac{B_{10}}{2},$$
(2.18)

where B_{10} is the magnitude of B_1 field. The magnetic field component of the RF field is crucial as it couples with the nuclei of the sample. Since B_1 field is of sinusoidal variation, it can be written as

$$\mathbf{B}_1 = \hat{i}B_{10}cos\omega_1 t.$$
(2.19)

If both the rotation frequency and the B_1 field frequency are equal to the

precession frequency of the nuclei at the Laromr frequency, the B_0 field will have no effect on the system and the effective field value, equation 2.18, will reduce to

$$B_{\textit{eff}} = \hat{i}\frac{B_1}{2}. \tag{2.20}$$

By applying an oscillating electromagnetic field with a frequency equal to the Larmor frequency in a rotating frame of reference, the resonance condition is fulfilled and the rotational transmit RF field component of the magnetic field B_1^+ will tip the magnetization vector to precess around the effective magnetic field with the angle, θ,

$$\theta = \gamma B_{\textit{eff}}\tau, \tag{2.21}$$

where $\gamma B_{\textit{eff}} = \omega_{rot}$, the angular frequency of the rotation, and τ is the duration of the RF field in seconds. In practice, by controlling the duration of the applied RF pulse, the magnetization vector can be tipped by 90° or 180°. These are called the "90° pulse" and the "180° pulse". In the laboratory frame of reference the magnetization will appear to precess in the transverse plane.
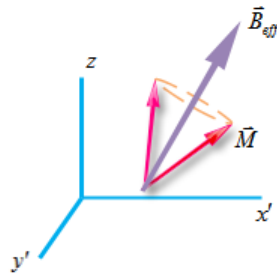
Figure 2.4: *The effective magnetic field in the rotating frame precessing around* $B_{\textit{eff}}$.
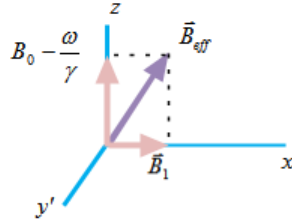
Figure 2.5: *The effective magnetic field vector of an applied RF excitation.*

2.7 Relaxation Mechanisms

Following the RF pulse, a signal is produced in a receive coil in accordance with the Faraday law of induction. The oscillating magnetic field induces an emf signal detected by an RF coil in proximity to the sample. This signal is called the Free Induction Decay (FID), as shown in Figure 2.6. The FID signal decays exponentially as a result of the relaxation mechanism of spins in the MRI system. In order to gain better insight into the relaxation mechanism, it is necessary to revisit the classical behaviour of the bulk magnetization under the influence of a magnetic field.
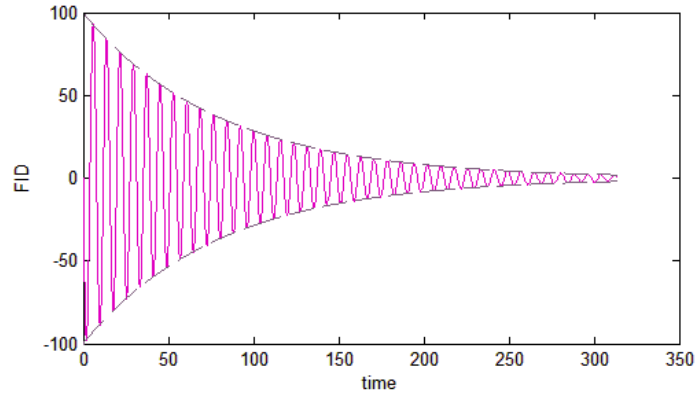
Figure 2.6: *The Free induction decay signal*

The magnetic moments of any sample are randomly oriented in the normal situation where no magnetic field is applied. In such a case there is no net magnetic moment. When the magnetic field is applied at room temperature, the magnetic moments begin to orient themselves with the magnetic field in an attempt to be in the lowest energy state precessing about the +z axis with the Larmor frequency. However, a small fraction will be precessing about -z axis. The excess of the magnetic moments give rise to the bulk magnetization pointing toward +z axis. Energy will be absorbed which enhances transitions between energy states.

After a 90^0 RF pulse, the magnetization begins the process of relaxation. Two types of relaxation take place. One type is "Longitudinal", also called "spin-lattice" relaxation, in which the axial magnetization recovers back to its equilibrium state at a rate given by the longitudinal relaxation rate $R = 1/T_1$. The time T_1 is a characteristic property of tissues, different tissues take different times to release their excess energy to the surrounding lattice and relax back to their equilibrium state.

Therefore, assuming a 90^0 RF pulse has been applied along the transverse plane, such that $\vec{M}(0) = \hat{i}M_0$. There will be no longitudinal component of the magnetization vector ($M_z(0) = 0$). The rate at which the net magnetization

vector relaxes to its equilibrium state is governed by the well known Bloch equation,

$$\frac{dM_z}{dt} = \frac{M_0 - M_z}{T_1}. \tag{2.22}$$

The solution to this equation is,

$$M_z = M_0(1 - \exp(-t/T_1)). \tag{2.23}$$

The other relaxation mechanism is "transverse" relaxation which is also called "spin-spin" relaxation. It represents the rate at which the transverse magnetization decays to zero following the application of an RF pulse. The transverse magnetization decay is quantified by the relaxation time T_2 which is also tissue dependent. One can understand the relaxation process by considering the nuclei at the atomic scale. Each nuclei causes a disturbance to their neighbours by altering the local magnetic field around them. Some nuclei experience slightly higher magnetic field and other experience slightly lower fields, called a spin-spin interaction. This in turn enhances the dephasing of the nuclei and enhances thus the decay of the transverse magnetization to zero when all the nuclei are out of phase. This property is a characteristic property of tissues based on the environment, mobility and bond nature of the protons. Hence, the lost transverse component is irrecoverable.

The decay of the transverse magnetization is modelled by the Bloch equation as

$$\frac{dM_{x,y}}{dt} = \gamma(\vec{M} \times \vec{B})_{x,y} - \frac{M_{x,y}}{T_2}, \tag{2.24}$$

which has the solution

$$M_x = M_0 \exp(-t/T_2) \cos(\gamma B_0 t),$$
$$M_y = -M_0 \exp(-t/T_2) \sin(\gamma B_0 t). \tag{2.25}$$

These two equations represent the shape of the FID signal detected by a well built RF receive coil. However, in practice the envelope of the FID signal does not represent the shape of the T_2 signal. This is due to the imperfection of the

MRI system which cause an additional inhomogeneity in the magnetic field B_0 as well as the susceptibility differences in the tissues which accelerate the decay of the signal. This decay is represented by the decay time T_2'. Therefore, the accurate representation of the transverse magnetization vector decay can be given by the T_2 and T_2' decay as

$$1/T_2^* = 1/T_2 + 1/T_2'. \qquad (2.26)$$

where $1/T_2^*$ is the rate at which the FID signal envelope decays. Since T_2^* is shorter than T_2, see figure 2.7, the Bloch equation is altered to give the representation of the decayed signal as:

$$
\begin{aligned}
M_x &= M_0 \exp(-t/T_2^*) \cos(\gamma B_0 t), \\
M_y &= -M_0 \exp(-t/T_2^*) \sin(\gamma B_0 t).
\end{aligned}
\qquad (2.27)
$$

The decay of the signal due to the system imperfections can only be recovered by using a refocusing technique such as a spin echo, while that caused by susceptibility differences is partially dealt with by shimming process which will be touched upon later in this chapter.
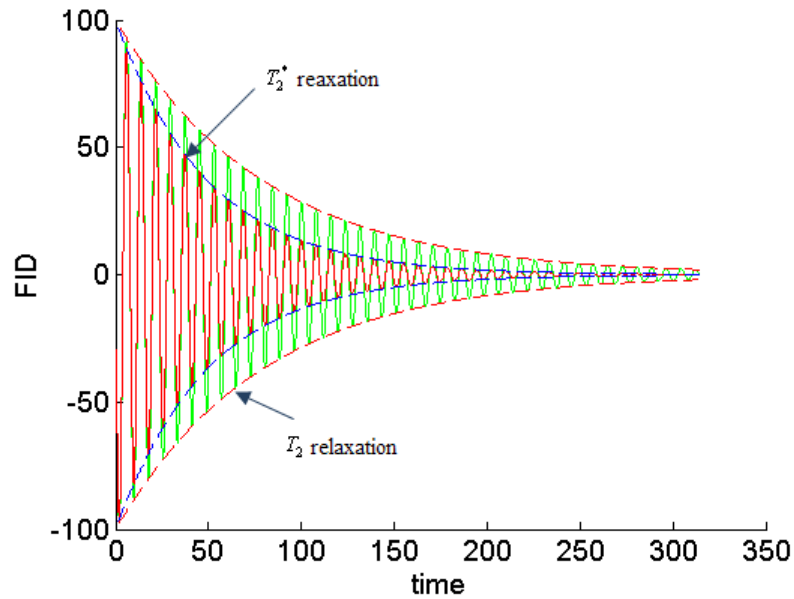
Figure 2.7: *The decay of the magnetization vector as a result of T_2^* and T_2 relaxations*

2.8   Imaging

2.8.1   Introduction

Although the FID signal is the origin of MRI images, one signal from the subject does not provide sufficient information to reconstruct an image. As it is well known from the fundamental equation of precessional frequency, equation 2.10, the frequency of spins is proportional to the static magnetic field B_0. Thus, having the entire spin system resonating at one frequency will provide a single peak on the NMR spectrum which leads to the need of localising NMR signals spatially.

The concept of spatially localising NMR signals was first noted in the early fifties by Gabillard [1] who calculated the proton density projection of the FID signal of water sample in a magnetic gradient. However, the real development of imaging started with Lauterbur [5] who used the back projection method to reconstruct the image of two tubes. The two and three dimensional Fourier transform technique for imaging and spectroscopy was first introduced in 1975 by Kumar et. al. [4] A couple of years later the fastest imaging technique was introduced by Mansfield [6] which he called Echo Planar Imaging (EPI).

2.8.2   Magnetic Field Gradient

A gradient field superimposed on the static magnetic field results in a linear variation in magnetic field. This is in turn causes the resonant frequency to vary as a function of position. The gradient field in all three directions can be written in a tensor form as

$$G = \begin{vmatrix} \hat{i}\hat{i}\dfrac{\partial B_x}{\partial x} & \hat{i}\hat{j}\dfrac{\partial B_x}{\partial y} & \hat{i}\hat{k}\dfrac{\partial B_x}{\partial z} \\ \hat{j}\hat{i}\dfrac{\partial B_y}{\partial y} & \hat{j}\hat{j}\dfrac{\partial B_y}{\partial y} & \hat{i}\hat{k}\dfrac{\partial B_y}{\partial z} \\ \hat{k}\hat{i}\dfrac{\partial B_z}{\partial x} & \hat{k}\hat{j}\dfrac{\partial B_z}{\partial y} & \hat{k}\hat{k}\dfrac{\partial B_z}{\partial z} \end{vmatrix}. \tag{2.28}$$

Since the resonant frequency of spins is only affected by the gradient compo-
nent of the same direction as the static magnetic field then the gradient tensor,
G, may be reduced to

$$\vec{G} = \frac{\partial B_z}{\partial x}\hat{i} + \frac{\partial B_z}{\partial y}\hat{j} + \frac{\partial B_z}{\partial z}\hat{k}, \tag{2.29}$$

and the resultant field at any point in z direction

$$B = (B_0 + G \cdot r)\hat{k}. \tag{2.30}$$

These gradient fields are used in slice selection, frequency and phase encoding
and are used in MRI imaging to reconstruct 2D and 3D images of a sample.

2.8.3   Slice Selection

The first step in acquiring 2D MR images is to excite spins within a selective
region of interest, i.e. to select a slice. This is accomplished by a linear
magnetic field gradient added to the static magnetic field B_0 and which is
applied by convention in the z-direction for this discussion.

Applying a 90^0 RF pulse at a single frequency will only excite a single line
in the slice corresponding to the one Larmor value that is associated with a
single value in the selected static magnetic field range, equation 2.30, as

$$\omega(z) = \gamma(B_0 + zG_z). \tag{2.31}$$

Exciting a slice of defined size is accomplished by applying a range of fre-
quencies which correspond to the Larmor frequencies of the desired part of
the subject, as shown in figure 2.8. The thickness of the slice is affected by
the narrowed bandwidth of the pulse and the accompanying gradient strength.
The slice thickness can be decreased by increasing the gradient strength or
reducing the RF pulse bandwidth. Therefore, it can be given as

$$\Delta(\omega) = \gamma G_z \Delta(z), \tag{2.32}$$
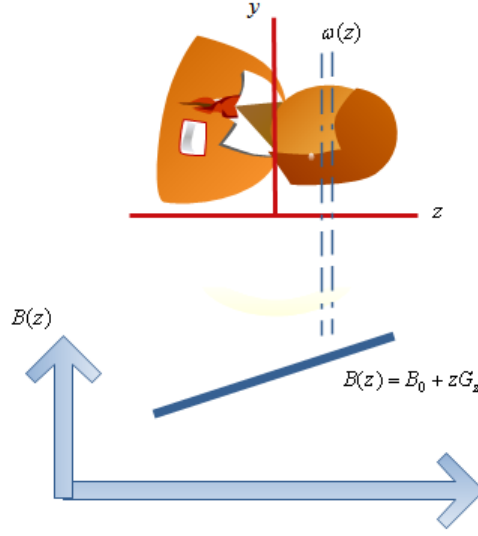
Figure 2.8: *Slice selection gradient*

where $\Delta\omega$ is the bandwidth of the RF pulse. One can shift the slice position by changing the central-frequency of the RF pulse and so a three dimensional acquisition can be obtained by acquiring successive slices. Figure 2.9 shows different RF pulses and their corresponding excitation profile.

2.8.4 Frequency Encoding

The frequency encoding gradient plays an important role in spatially locating signals from spins in the slice. The FID signal from the selected slice represents the sum of the signals from all spins as they all precess with same frequency. Therefore, a gradient field is introduced along the x-direction of the 2D slice,

$$B(x) = (B_0 + xG_x). \tag{2.33}$$

The changing magnetic gradient will force spins to precess with different frequencies in the gradient direction, given by

$$\omega(x) = \gamma(B_0 + xG_x). \tag{2.34}$$

Hence, the signals will consist of a range of frequencies in the time domain, related to specific spatial locations. The Fourier transform of these signals
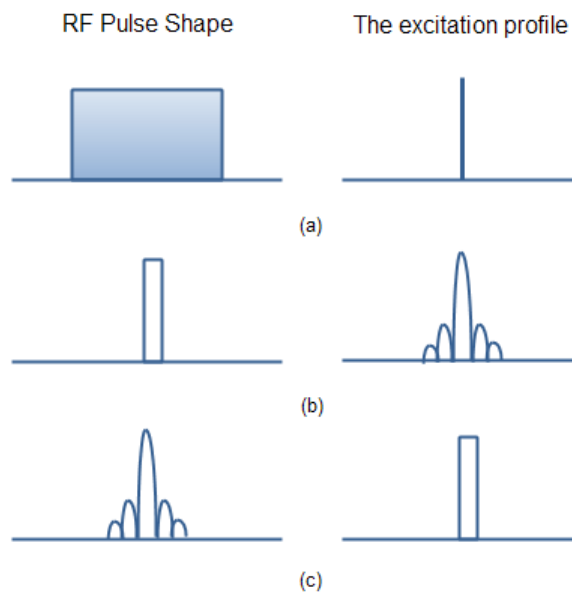
Figure 2.9: *RF pulses in the time domain and their correspoding excitation profile in frequency domain: (a) an infinitely long pulse gives a thin slice; (b) a rectangular pulse gives a Sinc profile and; (c) a Sinc pulse gives a rectangular slice shape.*

reflects signal intensities of strips of spins along the y-direction which is linearly related to their corresponding spatial location in the gradient direction.

2.8.5   Phase Encoding

In order to spatially localize an MR signal in a 2D image, a third gradient is implemented in an orthogonal direction to the frequency encoding gradient. Applying the phase encoding gradient imposes a linear phase variation of the spins in the direction of the applied gradient.

The phase encoding gradient, G_y, is applied prior to the readout gradient along the third direction, typically the y-direction. This, causes a linear spatial variation in the spins' precessional frequency given as:

$$\omega(y) = \gamma(B_0 + yG_y).\tag{2.35}$$

Considering a rotating frame of reference with frequency $\omega = \gamma B_0$, the phase accumulation resulting from the application of the phase encoding is,

$$\phi(y) = \gamma y \int_0^T G_y(t)dt,\tag{2.36}$$

where T is the duration of the phase encoding step. In order to map all spins' phases to their spatial location within the image matrix along the phase encoding axis, several FID signals are acquired. This is achieved by imposing the phase changes through varying the phase gradient strength G_y as many steps as the desired size of the 2D image matrix along the y-axis. Each FID signal takes a time of repeat, TR, in order to repeat the signal acquisition at different gradient strengths.

After acquisition, signals are sampled and stored in rows of a k-space matrix. The k-space data are then further processed by the two dimensional Fourier Transform (2DFT) to acquire the final MR image.

2.8.6 Spin Echo and Gradient Echo

It has been mentioned in section 2.7 that the FID signal decays and looses coherence due to the T_2^* effect. Spins under the effect of localised low magnetic field variation precess slower than those that are under slightly higher local magnetic field variation. After a given time all spins are out of phase. At this point applying a 180^0 RF pulse will reverse the spins in the transverse plane, the faster spins will be lagging behind the slower spins and, after a second time period the spins then come back to be in phase to form the so-called spin echo signal. The time between the 90^0 pulse and the echo signal is called the echo delay time or time to echo (TE) and the 180^0 pulse called the refocusing pulse or rephasing pulse. If the signal sampling is timed to be at the echo time, the dephasing due to the T_2^* effect would be overcome and the contrast in the image depends on T_2 only.

Applying two gradient lobes sequentially with opposite polarity creates a gradient echo. Spins under the influence of gradient field strength will have different spatial frequencies and thus will become out of phase with time as some spins precess faster than other . Applying a gradient lobe with opposite polarity will reverse the spins and bring them into phase again. A gradient echo compensates for the dephasing caused by the gradient field but not by the T_2^* effect due to the field inhomogeneity and the susceptibility. The contrast of the image then depends on the T_2^*.

2.8.7 k Space

In acquiring and handling MRI data the sequence of events plays very important role. The order at which pulses and gradients are applied is crucial in any imaging sequence. In any pulse sequence, data are stored with reference to k-space positions and are then Fourier transformed into images. The one

dimensional signal in the k-space can be given as

$$s(k) = \int dz \rho(z) \exp^{i2\pi kz}, \qquad (2.37)$$

where $k(t) = \gamma \int_0^T G(t)dt$ is the spatial frequency. As mentioned before in section 2.8.5, in 2D imaging, k-space is a row matrix with the x-axis representing the frequency encoding gradient axis, k_x, and each row of data along the y-axis representing a different phase encoding value, k_y. After the application of the 90^0 pulse and before the application of any gradient the origin of the k-space would contain information from the whole excited 2D slice with data not yet spatially encoded. After data collection following the gradient application the centre of k-space contains information about the contrast and largest details of the image , i.e. the lowest spatial frequency, while the finest details with the highest spatial frequencies determine the edges of the space.

Different image sequences acquire data following different k-space trajectories when spatially encoding the data. For example in the 2D gradient echo sequence, see figure 2.10, after the 90^0 RF pulse for a specific slice, a negative phase encoding gradient is applied to shift the data encoding to the bottom row of the k-space from the origin. This is followed by a negative readout gradient to shift the signal to the left in the readout axis k_x. Then, during the application of the positive readout gradient the data is sampled and encoded from left to right successively at the echo time. The same process is continued to fill the 2D k-space with a slightly less stronger negative phase encoding gradient after the application of the excitation pulse to place the data correctly along the phase encoding axis k_y. Another example is the spin wrap sequence. The sequence starts with a 90^0 RF pulse for a thin slab of spins with a slice selection gradient which is followed by a negative rephasing gradient lobe for half of the slice selection gradient duration.Then, a phase encoding gradient along with a negative frequency encoding (readout) gradient is applied before the positive readout gradient. This allows the encoding of the of the signal

along k_x axis from left to right. This course of action represents a line in k space. Therefore, the sequence is repeated with different phase encoding gradient strength for the same time to step in k_y direction and therefore acquire the whole k space. A 2D Fouier transform of the collected produces the final image, Figure 2.11 shows the spin wrap sequence and the corresponding k space trajectory.

Encoding the data with a different trajectory could save a considerable amount of time in imaging such as in Echo plana Imaging (EPI). Using this technique a full 2D space can be acquired in a single excitation. In the course of the sequence, the acquired data follows a trajectory in a raster pattern shown by figure 2.12.
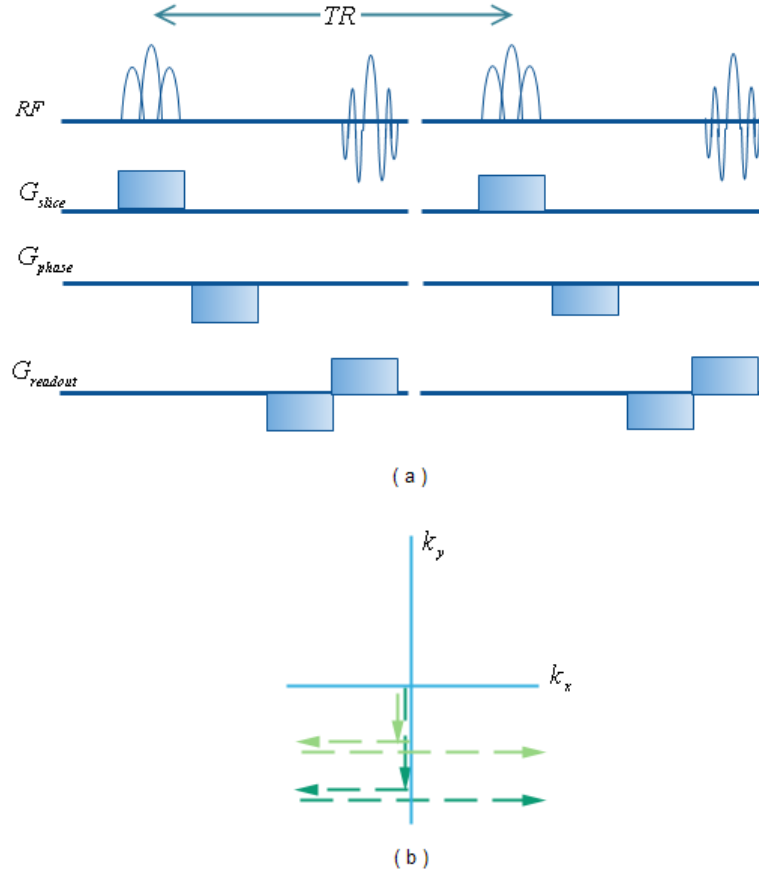
Figure 2.10: *The 2D gradient echo sequence a. time sequence b. k space trajectory*
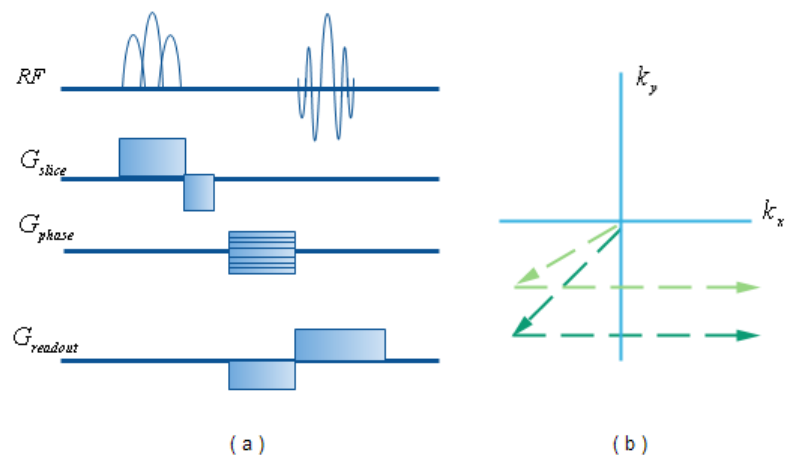
Figure 2.11: *The 2D spin wrap sequence a. time sequence b. k space trajectory*
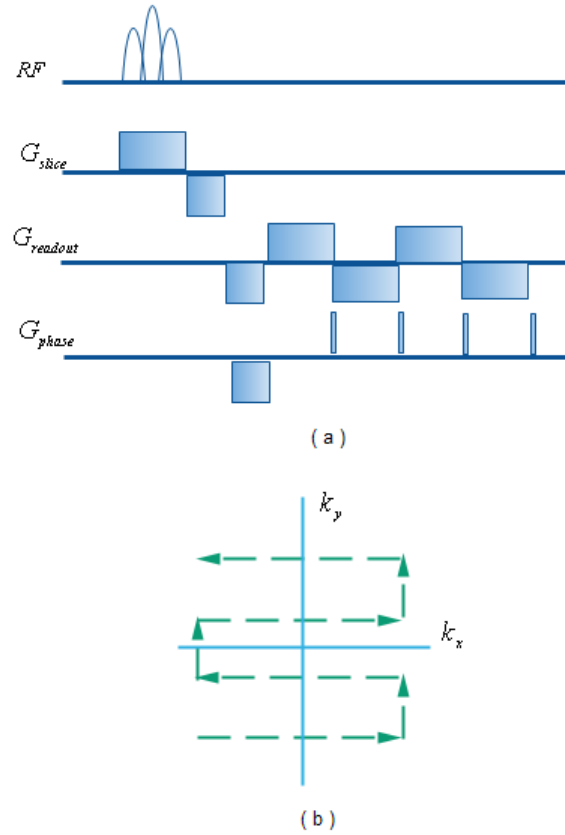
Figure 2.12: *The EPI sequence a. time sequence b. k space trajectory*

2.8.8   Contrast in MR Images

Having good image contrast is essential in clinical diagnostic imaging. The contrast of MRI images depend on the properties of the tissues' T_1 and T_2 relaxation. Different tissues have different recovery and relaxation times. Thus, by adjusting the scan parameters: the repetition time (TR) and echo time (TE), one of three contrast can be acquired: T_1 weighted contrast, T_2 weighted contrast or proton density weighted contrast.

In proton density weighted images, the T_1 and T_2 effect on the signal intensities are minimized by selecting long TR and short TE times and therefore the signal intensity will be only due the differences in the proton density of the tissues. T_2 weighted images have long TR and TE time, while short TR and short TE put more T_1 weight on the images. All three types of contrast will

always exist in all imaging sequences; however, the emphasis will be mostly on one type through scan parameter setting.

The abundance of water molecules in the body which are in continuous motion leads to the use of motion contrast imaging. Different pulse sequences can be used to provide a non-invasive imaging aid. For example, magnetic resonance angiography (MRA) provides images of the blood vessels structure. It can be used in detecting cardiac disorder, strokes and vascular disorders. One technique is the time of flight (TOF)MRA. Signal detected is based on blood displacement. It involves saturation of a selective slice and after a waiting time through which a new blood stream enters the slice a gradient echo image acquisition is applied to the same slice. The TOF signal depends on the amount of the new blood that enters the slice. Another technique is the velocity encoded phase contrast (VENC-PC)MRA where three gradient fields are used to produce a change in spins' precession phase; hence, a map of 3D flow can be created. Two sets of images can be acquired, one with strong gradient and the other with no or opposite gradient. The difference between the two images will represent the blood vessels when changes of phase have been introduced, [3]. Another type of contrast uses the diffusion of water in imaging. Brain tissues are anisotropic (water molecules diffuse in one direction faster than in other directions). Diffusion Tensor Imaging(DTI) is used to quantify water movements in voxels through calculating *fractional anisotropy* (FA). It has a value between 0 and 1, in which 0 means that water molecules diffuse equally and 1 means that the majority of molecules diffuse along some axis. The decrease of FA in affected voxels is a measure in multiple sclerosis and vascular dementia. For diffusion imaging controlled gradients are applied in pulse sequence in order to quantify the diffusion which is called the diffusion gradient. For example, in spin echo sequences diffusion gradient is applied before and after the refocusing pulse [2, 3].

2.9 MR System Hardware

Introduction

This section gives a brief overview of the MRI system, see figure 2.13. The most important part in the system is the magnet. Within the bore of the magnet, there are the shim coils, gradient coils and RF coils. In the case of the 7T scanner, the RF coils are usually attached to the bed.
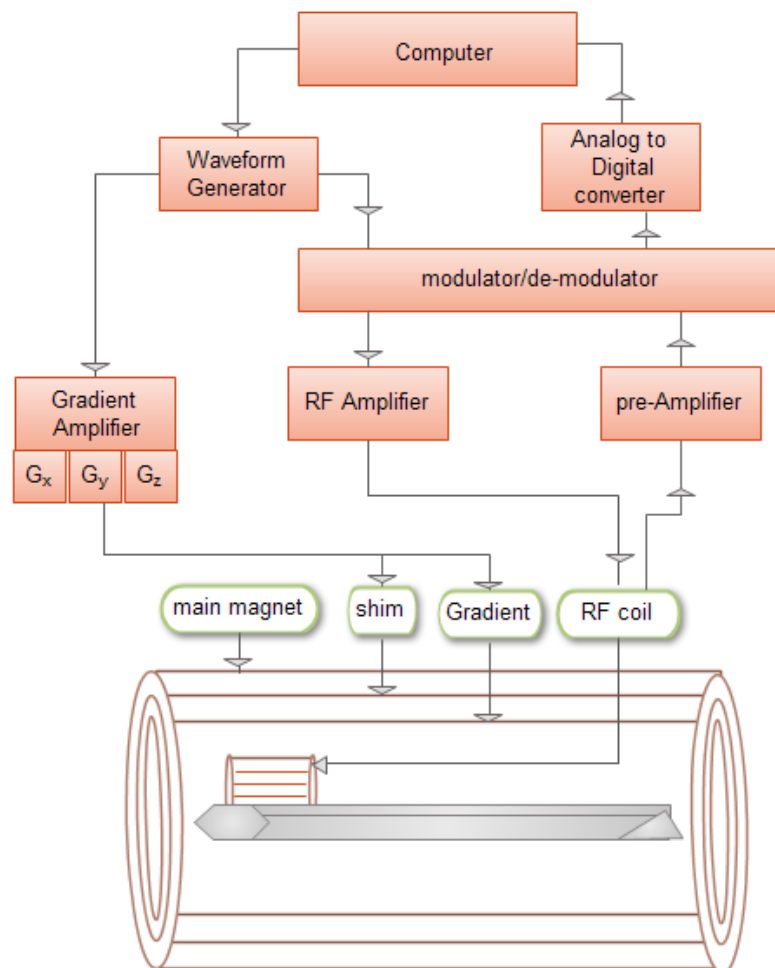
Figure 2.13: *The MRI system*

2.9.1 The Magnets

In the design of any MRI magnet several aspects have to be considered. These are: the field strength; spatial homogeneity; temporal stability; patient comfort; cost and fringe field minimization. The primary requirements of magnets is that they provide a spatially uniform magnetic field strength over the region being imaged. A homogeneity of 5 parts per million (ppm) over a 50 cm diameter for a clinical whole body magnet of 1.5 T strength is acceptable. The inhomogeneity in any body magnet causes image distortion and also speeds up the T_2^* dephasing. Therefore, it can be said that the uniformity should be such that the $T_2^{'}$ is longer than the readout gradient time during acquisition and that the readout gradient imposes more spin spatial variation than the spatial inhomogeneous static field. The changing of the field homogeneity over time could cause variation in the protons' precessional frequencies which in turn leads to images artefacts. However, it can regarded as negligible over the acquisition time. The fringe fields from the main magnet must be taken into consideration when installing the MR systems as they affect any nearby electronic devices. For example, fringe fields cover a region of 10 to 30 m from an unshielded 0.5 T magnet. Therefore, usually active or passive shielding is installed in the system to cancel out these undesired fields outside the magnet. In active shielding two pairs of coils with currents running opposite to that of the interior coils will generate a field that cancels out the fringes. In passive shielding, iron is installed into the wall of the imaging site or surrounding the main magnet. Most installed clinical systems are actively shielded, but for high field ($3T$) research systems still use passive shielding. The 7T system installed in Nottingham is surrounded by 200 tonnes of passive iron shielding. The magnet strength of clinical MRI systems are of field strengths up to 3T while magnets of up to 9.4 T field strength are available for human research systems. Three magnet types are used in MR systems: permanent; resistive and

superconducting. The permanent magnet systems are made of ferromagnetic material such as iron and are for field strengths up to 0.4 T. The uniformity is achieved by a careful shaping of the pole faces. However, one major drawback is the heavy weight of these magnets; they can weigh upto 100 tones for whole body magnets. They have the virtue of producing low fringe field; have low maintenance costs and the open design is suitable for claustrophobic patients. However, they require temperature control to maintain the field uniformity.

Resistive magnets are rarely used nowadays. They consist of copper wires by which the magnetic field is generated. With such a magnet, a coolant system must be introduced due to the heat generated by the currents in the wires. For example, a few millimetres in diameter of copper wire operating at room temperature carries about 100 amps continuously. However, in most of the recent MRI systems superconducting magnets are used. The wire of such magnets is made of an alloy of niobium or titanium which has no resistance when cooled under a temperature of less than 4K. Currents will flow in the wire continuously with zero resistance which gives rise to a high spatially uniform and stable magnet field because there is no power dissipation. In order to keep wires in a super-conductive state the wires are immersed in liquid helium at 4K.

The Nottingham 7T system magnet was installed in November 2004. The magnet installed is a Magnex (Oxford) with a 90 cm bore with estimated homogeneity of about 0.10 ppm.

2.9.2 Shim System

Shim coils are used to remove the inhomogeneity introduced during the magnet design process. It's almost impossible to construct magnets that are as homogeneous as specified by the theoretical designs. This is due to the variability during the manufacturing process, for example, wire distribution, contraction

of wires when cooled by helium to 4 K, shifting of wires under the passive magnet force, magnet stressing during transportation, etc. All these factors cause inhomogeneity of a few hundred ppm. Add to that the inhomogeneity caused by the difference in susceptibility between tissues, as well as structures around the magnet affecting the local magnetic field, leads to a requirement to have shim methods.

There are two main methods of shimming: passive and active shimming. For passive shimming pieces of iron are placed in the magnet bore in trays on the outer bore wall. For active shimming, coils surrounding the main magnet are used for field corrections. The field homogeneity is corrected through a repeated process of measuring the fields then shimming until target uniformity is achieved.

2.10 The Gradient Coils

During imaging acquisition a deliberate linear field inhomogeneity is imposed in the imaging region to encode spatially the spin's position within that region, as described in section 2.8. Three orthogonal resistive coils are set inside the magnet bore to generate the additional linear variation of the field in all the three orthogonal directions (x,y,z). Typically, they are capable of producing a linear variation of about 40 mT/m over the volume of interest.

There are criteria that have to be met in gradient coil design in general, although they can be designed to a specific application and desired performance. These are: low inductance; minimum resistance; high gradient to current ratio; good gradient uniformity; minimum interaction with conducting shields,; absence of torque; high duty cycle; minimum temporal field variation and suitable access for the patient.

The fast switching of the gradients causes flux changes that give rise to eddy

currents throughout the system, in the patient; main magnet components; rf coil and shield. The eddy currents produce a magnetic field that opposes the gradient field and hence reduce its performance and distort the images. They also can cause body currents and undesirable nerve stimulation if they are high enough. Active shielding may be used to reduce the effects of eddy currents.

2.10.1 The RF System

As stated throughout previous sections an RF pulses, the B_1 field is used to flip the spins and hence generate a detectable NMR signal. In practice, to irradiate the tissues a transmitter associated with an RF coil is used while for detection a receiver associated with a separate RF coil is used.

In the transmitter, a frequency synthesizer is used to generate an oscillating defined frequency which is multiplied by a defined pulse shape given by the waveform generator. An RF power amplifier is used to provide the power in order to tip the magnetization vector to the desired flip angle. The typical amplifiers for MR systems have an rf output power ranging from 2-30 kW, In the Nottingham 7T scanner, a 4 kW amplifier is installed. The RF power required to excite spins is dependent on many factors: main magnet strength, transmit coil efficiency, the duration of the RF pulse and the desired tipping angle.

In the receive mode, the FID signal produced by the relaxation process is induced in the receive coil, and is of the order of nV in magnitude and MHz in frequency, see section 2.7. Following this, the signal is amplified by a low noise amplifier (LNA) that is built into the RF coil for maximizing the signal detection with minimal noise. The signal is then demodulated to a reference frequency in order to split it into real and imaginary parts. The signal is then filtered with a band pass filter and digitised by an analogue to digital converter to be reconstructed in the main computer.

Through the RF coils, the radio frequency pulses couple to the body (sample) in transmitter mode while in the receiver mode they couple the received signal from spins to the console for acquisition. Independent coils can be used for transmission and reception or a single coil can be used to serve both objectives. RF coils need to generate a B_1 field orthogonal to the main field B_0 that is uniform over the imaged region. The next chapter will cover the RF coil in

greater detail.

Bibliography

[1] R. Gabillard. Measurement of relaxation time t_2 in the presence of an inhomogeneity in the magnetic field more important than the width of the line. *C. R. Acad. Sci.*, 232:1551–1552, 1951.

[2] P. Hagmann, L. Jonasson, P. Maeder, J. Thiran, V. Wedeen, and R. Meuli. Understanding diffusion mr imaging techniques: From scaler diffusion-weighted imaging to diffusion tensor imaging and beyond. *RadioGraphics*, 26:S205–S223, 2006.

[3] Scott A. Huttel, Allen W. Song, and Gregory McCarthy. *Functional Magnetic Resonance Imaging*. Sinauer Associates Inc., second edition edition, 2009.

[4] A. Kumar, D. Welti, and R. R. Ernst. Nmr fourier zeugmatography. *J. Magn. Reson*, 1975.

[5] P.C. Lauterbur, D.M. Kramer, W.V. House, Jr., and C.-N. Chen. Zeugmatographic high resolution nuclear magnetic resonance spectroscopy. images of 243 chemical inhomogeneity within microscopic objects. *J. Am. Chem. Soc.*, 97:6866–6868, 1975.

[6] P. Mansfield. Multi-planar image formation using nmr spin echoes. *J. Phys. C. Reson*, 1977.

Chapter 3

Radio Frequency Coils: Design and Specifications

3.1 Introduction

RF coils are used for transmitting RF pulse in order to excite spins in any volume of interest in the body. They are also used for signal reception. This chapter will cover RF coils in detail; starting from the reciprocity concept in MRI, to the different types of RF coils. The basics of RF coil circuits, RLC circuit theory, used in coil design is also covered in the chapter.

3.2 RF Signal Transmission,Reception and the Principle of Reciprocity

RF coils are used for two purposes: as a transmitter to excite the magnetization vector and as a receiver to detect the FID signal during magnetization relaxation and image encoding. Transmit coils are designed based on one of the most primary laws in electromagnetism, Ampere's law. Ampere's law states that the closed line path integration of a magnetic field is equal to the current

enclosed by that path, [21]

$$\frac{1}{\mu_0} \oint B \cdot dl = \int_S J \cdot dS. \tag{3.1}$$

Therefore, a good RF transmitter coil has to be able to generate a uniform rotating magnetic field B_1 oscillating at the desired Larmor frequency of the spins, as discussed in section 2.6 in the previous chapter.

Following excitation, the rotating magnetic field resulted from the precession of the magnetization vector generates an induced EMF ξ, the FID signal, in a receiving probe according to the Faraday induction law

$$\xi = \oint E \cdot dl = -\frac{d}{dt} \int_S B \cdot dS. \tag{3.2}$$

An essential property for receive coil design to obtain is that of high signal sensitivity. Therefore, it is more common to use separate coils for transmission and reception as each coil can be designed for optimal performance at the desired Larmor frequency. However, a single coil can be used for both.

Hoult conducted an experiment that described the reciprocity nature between RF signals of the transmit and receive coils, [9]. He assumed that the precession of the spin system (magnetization vector) can be considered as a current loop that will generate a uniform magnetic flux through the receive coil and induce a voltage signal. The same induced voltage would generate a rotating B_1 field that tips the magnetization vector in the transverse plane. A linearly polarized RF magnetic field B_1 generated by a single coil can be decomposed into two counter rotating field components, in term of complex phasor notation [16, 9]

$$\hat{B}_1 = \frac{1}{2}(B_1 \exp j\omega t + B_1 \exp -j\omega t), \tag{3.3}$$

$$B_{1x} = Re[\hat{B}_1] \text{ and, } B_{1y} = Im[\hat{B}_1] .$$

However, for high field MRI the wavelength in tissues becomes comparable to body size. Therefore, the field generated is elliptically polarized due to any phase shift between the conduction and displacement currents within the

tissues where they generate their own field. Therefore, the elliptically polarized field generated by the RF coil can be written as

$$\hat{B}_1 = Re[(\hat{B}_{1x}\hat{x} + \hat{B}_{1y}\hat{y})\exp i\omega t]. \tag{3.4}$$

The z component of the RF field does not affect the magnetization, and can be thus neglected. The field can be decomposed into two counter rotating components. One of which, B_1^+, will tip the magnetization vector in to the transverse plane as it precess in the same sense as the spins during signal transmission while the other B_1^- will be out of phase by 2ω and therefore can be ignored. Equation 3.4 can be rewritten as

$$\begin{aligned} B_1^+ &= \frac{1}{2}(\hat{B}_{1x} + i\hat{B}_{1y})\exp j\omega t \\ B_1^- &= \frac{1}{2}(\hat{B}_{1x} - i\hat{B}_{1y})^* \exp -j\omega t \end{aligned} \tag{3.5}$$

These two equations correspond to the RF field components in two different rotational directions as seen from the stationary frame of reference where the first is rotating in the $+\omega t$ direction and the second is rotating in the the $-\omega t$ direction .

In signal reception it is the B_1^- component that will be detected in the RF probe rather than B_1^+ field.

3.3 RLC Equivalent Circuit and Resonance

One of the primary requirements when designing an RF coil, is to transmit a uniform magnetic field over the region of interest and to enhance the signal received at the appropriate frequency, [9]. All RF probes are basically inductors that are tuned to a specific resonant frequency.

The RF coil can be described by an equivalent RLC circuit. The probe is made of a conductor with inductance L that naturally poses some resistance R and is tuned at the desired frequency by adding a parallel capacitor C across the terminal. Figure 3.1 shows simple circular loop with its equivalent circuit.
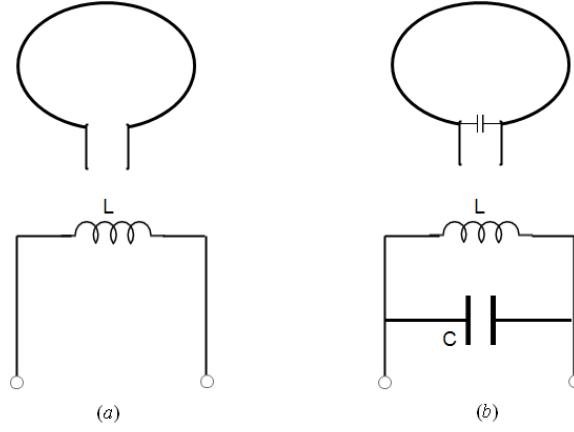
Figure 3.1: *Simple coil loop: (a) coil is not tuned, (b) tuned coil.*

The impedance measured across the RF coil terminals is given as

$$Z = R + jX \tag{3.6}$$

where R is the resistance of RF probe. It dissipates energy as heat by the means of ohmic law

$$W = \frac{1}{2}I^2 R \tag{3.7}$$

where the current I is the peak current of the circuit.

However, electric and magnetic field energy is accounted for in the reactive part of the impedance which can be decomposed into capacitive and inductive reactances given as

$$X = X_C + X_L$$
$$X_C = \frac{1}{\omega C} \tag{3.8}$$
$$X_L = \omega L$$

where $\omega = 2\pi f$, the resonant frequency of the alternating input current. A high coil efficiency which yields high acquisition SNR occurs when the coil is tuned to resonant at the desired Larmor frequency. This is done by minimizing

coil impedance through bringing the reactance to zero.

$$X = 0$$

$$X_C = X_L \quad and$$

$$\omega_0 = \frac{1}{\sqrt{LC}}$$

(3.9)

When the resonant condition for the coil system is met, the electric and magnetic energy transfer equally between system passive components at the resonant frequency during each cycle and dissipates energy through the real resistance R. The choice of the appropriate L and C components is crucial since the NMR system is confined by the magnetic field strength to a specific frequency band width, with the Larmor frequency as the centre-frequency. The RF coil can be tuned by varying the inductor or the capacitor across the terminal. It is more common to tune the probe using a variable capacitor. In practice, most coils have several distributed capacitors in order to produce a uniform current distribution and a hence homogeneous magnetic field B_1 distribution over the region of interest. This decreases the electric field produced by the coil and therefore reduces the tissue heating. However, as the static magnetic field strength increases and their corresponding Larmor frequencies increase, RF coils are no longer simple loops with capacitors associated to it. They become a complicated distributed configuration of electric capacitors and inductors and therefore more care is required when designing these types of coils.

3.4   Q-Factor

In resonant coils, the oscillating energy is shared electrically and magnetically. The efficiency of the coil in providing high field sensitivity can be measured by the well known Q factor. Q factor is defined as the ratio of the energy stored

in the system to the energy dissipated during one cycle,

$$Q = 2\pi \times \frac{Energy\ stored}{Energy\ dissipated\ per\ cycle}. \tag{3.10}$$

The emf voltage measured across a probe terminal at resonance is

$$V = Q\xi, \tag{3.11}$$

where ξ is the signal voltage. The quality factor of the simple LCR circuit is given as

$$Q = \frac{\omega L}{r}, \tag{3.12}$$

and can also be expressed as

$$Q = \frac{1}{r\omega C}, \tag{3.13}$$

where r is the resistance associated with the circuit components as they are not ideal. Typically, Q values range between 50 to 500 for NMR coils [17]. Another equivalent way of defining the Q factor is in term of the frequency bandwidth as

$$Q = \frac{f_0}{\Delta f}, \tag{3.14}$$

where f_0 is the resonant frequency and Δf is the range of frequency band width at the half peak power value.

3.5   Impedance Matching

Transmitting the signal from the coil to the pre-amplifier efficiently is as important as detecting a strong FID signal from the coil. Matching the probe impedance to the transmission line, 50Ω impedance, is crucial to avoid any reflections which leads to image signal loss. The reflection coefficient is defined as:

$$\Gamma^2 = \frac{Energy\ reflected\ at\ the\ boundary}{Energy\ reflected\ +\ the\ Energy\ transmitted}, \tag{3.15}$$

$$\Gamma = \frac{Z_{coil} - Z_{TL}}{Z_{coil} + Z_{TL}}, \tag{3.16}$$

where Z_{coil}, Z_{TL} are the coil and transmission line impedance, respectively. When $\Gamma = 0$, all the power is transmitted and reflections are eliminated. In other words, the impedance matching condition is met:

$$Z_{TL} = Z_{coil}^*, \tag{3.17}$$

where Z_{coil}^* is the complex conjugate of the coil impedance.

3.6   SNR and RF Coil Losses

The Signal to Noise Ratio (SNR) determines the quality of any MRI image. It is the amount of the NMR signal detected by the RF probe to the amount of noise. At ultra high magnetic fields, the increase in signal is associated with coil and tissue losses as

$$SNR \propto \frac{\omega^2 B_1}{\sqrt{R_\Omega + R_r + R_{tissue}}}, \tag{3.18}$$

where R_Ω, R_r and R_{tissue} are the ohmic resistance, radiation, and coupled tissue resistance, respectively. Therefore, one of the major issues in high field coil design is to overcome coil losses given as resistive and radiation losses as well as tissue losses.

3.6.1   RF Coil Losses

An ideal RF coil would be expected to act more as an energy conserving coil and less as an antenna or radiating coil. However, in reality coils loose energy especially as field strength increases. Therefore, RF coil losses can generally be considered as a result of power dissipated to the Ohmic and radiation losses,

$$P_{loss} = \frac{I^2}{2}(R_\Omega + R_r), \tag{3.19}$$

where $R_\Omega = R_L + R_C$ is the ohmic resistance due to the real resistance of the conductor and capacitor. The ohmic losses increase with $\sqrt{\omega}$ and ω for conductor and the capacitor losses respectively. As a consequence, these affect the RF transmitter efficiency as well as SNR of the RF receive for any tuned RF coil at the operational frequency.

For an arbitrary coil with length l, conductivity σ, cross section A, current flow on the surface of the conductor dissipate power as heat, as a result of the resistance of the conductor surface area R_s, thus

$$R_L = \frac{R_s l}{A}, \quad R_s = \sqrt{\frac{\omega \mu}{2\sigma}},$$
$$R_C = \frac{1}{\omega Q C}.$$
(3.20)

Ohmic losses can be minimized at high operational frequencies by using a distributed circuit design which will decrease the inductance of the coil or by increasing the surface area of the coil.

RF coils generally lose energy to loading tissues, the magnet bore and the surrounding free space. It can be thought of as the difference between coil's input power and Ohmic losses within the coil. For electrically small coil enclosed by a surface area A, radiated power in terms of the complex poynting vector can be given as [1], [15] :

$$P_r = 0.5 \int_A (\mathbf{E} \times \mathbf{H}^*) \cdot dA$$
(3.21)

Hence, for arbitrarily shaped wire loops used for NMR detection, the power radiated and the radiation resistance are given as

$$P_r = 10I^2(\beta^2 A)^2$$
$$R_r = 20(\beta^2 A)^2 \approx 31,200(A/\lambda^2)^2,$$
(3.22)

for phase constant $\beta = \omega\sqrt{\mu\varepsilon}$. Equation 3.22 indicates that at high fields, radiation losses increase by ω^4 and A^2. Consequently, the transmit efficiency and the SNR received is decreased while power absorption is increased in biological tissues. One way to control radiation losses is by building small coils

of size 0.1λ in a multi-coil array. Another option is to use TEM (Transverse Electromagnetic) coil design or a Birdcage coil, [16], [24]. Moreover, travelling wave MRI exploits the radiative effect in the design of the antenna.

3.6.2   Tissue Losses

The wavelength in tissues with high water content at 128 MHz, 3 T, clinical systems, is about 27 cm, and reduces to about 12 cm at a frequency of 300 MHz (7 T). Accordingly, B_1 field homogeneity deteriorates as a result of wavelength and interference effect.

For a lossy-anisotropic, inhomogeneous coil-tissue system, a $\mathbf{B}_1$ field produces eddy currents, $\mathbf{J}_e$, due to tissue conductivity, σ, and displacement currents $\mathbf{J}_d$ as a result of tissue dielectric effects, [7]:

$$
\begin{aligned}
J_e &= \sigma \mathbf{E} = -j\omega\sigma \mathbf{A}, \\
J_d &= -j\omega\varepsilon \mathbf{E} = \omega^2 \varepsilon \mathbf{A},
\end{aligned}
\tag{3.23}
$$

where $\mathbf{A}$ is the magnetic vector potential defined as $\mathbf{B} = \nabla \times \mathbf{A}$. The total power dissipated in tissues can be calculated as

$$
\begin{aligned}
P_{tloss} &= \frac{1}{2} \int_V (\mathbf{J} \cdot \frac{\mathbf{J}^*}{\sigma}) dV, \\
\mathbf{J} &= \mathbf{J}_e + \mathbf{J}_d.
\end{aligned}
\tag{3.24}
$$

Power lost in tissues is dominated by displacement current density losses as it increases with ω^2 in comparison to eddy currents' losses which are linearly proportional with operational frequencies. In addition to B_1 inhomogeneity and SNR losses, tissue losses cause excessive tissue heating measured by the Specific Absorption Rate (SAR). Tissue losses can be controlled by RF shimming; RF shimming reduces radiation resistance and enhances coil efficiencies, designing RF coils that target a specific region of interest (ROI), driving coils with efficient RF pulse sequence reduces the power and decrease tissues losses.

3.7 Specific Absorption Rate(SAR)

The power dissipated in the sample is given by rewriting equation 3.22 in terms of the electric field as

$$P = \int_V \frac{\sigma |E|^2}{2} dV, \tag{3.25}$$

SAR is calculated as

$$SAR = \frac{\tau}{2T_R} \int_V \frac{\sigma |E|^2}{\rho} dV, \tag{3.26}$$

where σ, ρ is the conductivity and density of the sample respectively and $\tau/2T_R$ is the RF duty cycle. By calculating the total power dissipated in the sample to both exposed time and sample weight, specific absorption (SAR) can be calculated as

$$SAR = \frac{total\ RF\ energy\ dissipated\ in\ sample}{exposed\ time \times sample \times weight}. \tag{3.27}$$

The international Electrotechnical Commission (IEC), [3] has restricted the normal operating mode to 4 W/Kg over the whole body, and 3.2 W/Kg over the head with these values averaged over a 6 min period. Numerical modelling is a common method to calculate SAR when designing RF coils which will be touched upon in later chapters. Temperature rise and measurements for any designed RF coil can be done using fluoroptic temperature-sensitive optical fiber probes. Using these probes, fluoroptic thermometry technique can be used to measure temperature changes due to RF power deposition in a head phantom during MR imaging experiments for the designed RF coils [14].

3.8 RF Coils

Losses in the RF coils and in the biological tissues can be controlled and reduced by proper coil design. RF coils can be optimized for uniformity, SNR and other criteria. Furthermore, it has been proven that with optimal RF

design and excitation, the specific absorption rate (SAR) and thus the tissue heating can be reduced.

3.8.1 Quadrature Drive Vs. Linear Drive

There are two possible methods for driving RF coils in MRI systems: linear or quadrature excitation. When the RF field is fed through a single point so that the B_1 field is directed toward a single direction, then the RF coil is called a linear coil and generates a linearly polarized field. As previously mentioned, equation 2.20, any linearly polarized field can be decomposed into two circular polarized fields, B^+ and B^-, one is rotating clockwise and the other is rotating anti-clockwise. Because only one component of the two is coupled to the rotating spins, B^+ in the transmission mode and B^- in the reception mode, it is favourable to use quadrature coils in the MR imaging. Quadrature coils could incorporate a hybrid device where the quadrature field is generated by two 90^0 out of phase currents through two feed ports. The quadrature coils have the virtue of requiring only half of the RF power that linear coils use. In term of signal reception, they have higher SNR by a $\sqrt{2}$ factor. The signal received by the coil is a circular polarized signal. Therefore, if a linear coil is used to detect a circular field only one component will be detected and the other will be wasted. Chen et. al [4] was the first to propose the use of quadrature coil for MRI transmission and reception. Many studies have been conducted since then and other forms of excitation have been preformed since, such as the 4-port excitation [12]. However, even though the quadrature excitation has proven to be better than Linear excitation, quadrature detection is more difficult to design and construct for practical coils such as surface coils.

3.8.2 Volume Coils

In the last few decades there has been a tremendous innovation in RF volume probes designed as a result of the introduction of high field MRI systems operating at frequencies up to 600 MHz. Most surface coils that are commercially available for imaging are used as receive only coils whereas head and body coils are used as transmit/receive coils. Probes ought to be able to transmit a uniform magnetic field over a region(volume) of interest and acquire high SNR signal with uniform gain at any point in the Volume of Image (VOI). Designing probes with such criteria is a very challenging engineering task. Therefore, RF probes can be classified based on the orientation of the rotational magnetic field with respect to the current distribution into two classes: Axial RF coils where the rotational RF magnetic field is directed along the axis of the coil, and transverse RF coils in which the rotational rf field is transverse to the probe axis. A uniform rotational magnetic field in an axial resonator is ideally generated by considering a uniform current distribution on a spherical surface, while for a more realistic coil design, such as a Helmholtz coil in figure 3.2(a), two parallel loops driven by in phase currents, gives a uniform field distribution.

The four coil configuration applied for low field resistive magnets [10] can also be applied for NMR probes with less restriction on homogeneity requirements (less than $\pm 5\%$), figure 3.2(b). Solenoid coils are another kind of axial coil, figure 3.2(c). They are used in Micro-coil design for NMR experiments. However, solenoid coils are not applicable in high field super conducting magnet due to their sample in-accessibility and self resonance effect.

r For large samples, loop gap coils are designed to work at high frequencies where the large number of turns in the solenoidal coil are replaced by one large loop (cylinder) with one or multiple gaps along the coil, where the gaps work as a tuning capacitors, figure 3.2(d). Thus, the high impedance problem in

the solenoid is overcome by the loop gap coil design,[5, 6].

(a) Helmholtz Coil   (b) Four Loops Coil

(c) Solenoid Coil   (d) Loop Gap Coil
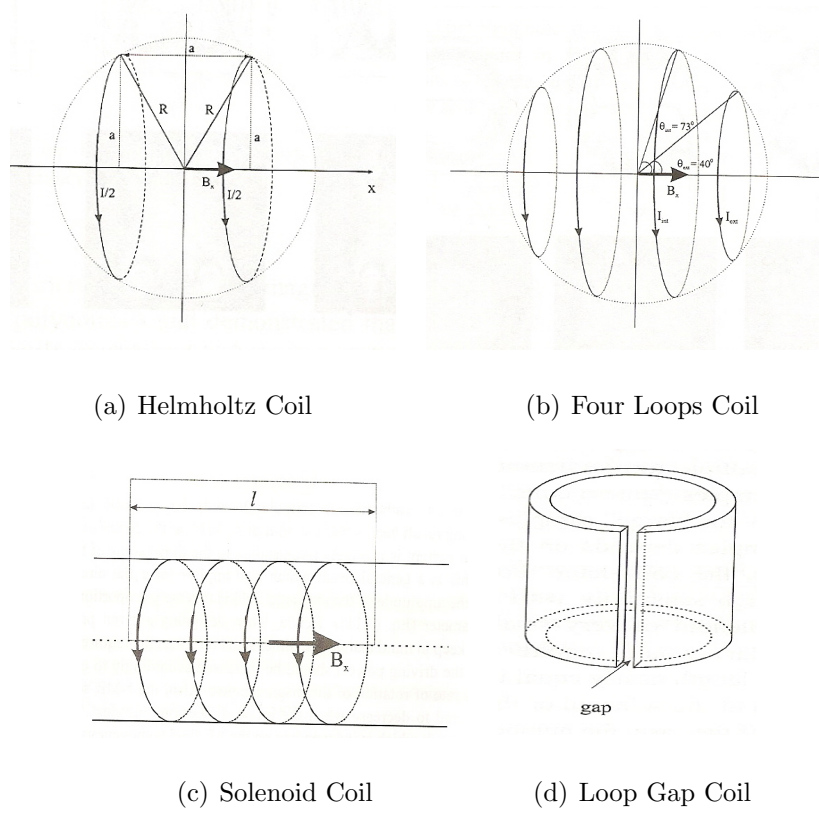
Figure 3.2: *Axial RF coils configurationqs [2].*

In contrast to axial coils, transverse coils work well with axial size magnets and other magnets so sample accessibility is not a concern when designing such coils. The sensitivity is lower in general than that would produced by an axial coils [11]. An ideally cosine current I distribution on a cylindrical surface generates an ideal homogeneity within the region of interest,

$$I = I_0 \cos(\theta)\hat{a}, \tag{3.28}$$

where θ is the azimuthal angle and the current directed along the magnet field B_0 direction. The saddle coil which is used in gradient coil design can loosely approximate an ideal current distribution in RF coil design. It consists of two pairs of axial wires laid over two halves shells and connected with arc shape wires as a return current forming a half-shell shape current loops, figure 3.3(a).

As the operating frequency increases above 100 MHz, the length of the current paths (coil's wire) are of the order $\lambda/10$ limit and the high impedance affects coil performance. The sample in the coil introduces parasitic capacitances which shifts the resonance frequency of the coil and causes sample heating as a result of dielectric losses. In response to high frequency coil demands, a slotted tube resonator STR was developed by Schneider and Dullenkopf [23]. The STR, designed as two shielded arc shape copper strips curved in cylindrical shape, can be easily tuned and matched at high frequencies. Figure 3.3(b) shows the STR configuration and the currents path.

Hayes *et al* [8] introduced the birdcage resonator as an approximation to the cosine current distribution. Hence, more field uniformity can be achieved at high frequencies. Physically, the birdcage resonator consists of arbitrary number of rungs which are equally distributed along the circumference of the coil. The birdcage coil can be represented electrically by a ladder network where each unit in the network represents a physical rung. It can be designed as low-pass with capacitors on the rungs; high-pass with capacitor on the end rings or hybrid-pass where capacitors are distributed on both rungs and end rings. A periodic ladder network of LC elements makes an electrical representation of the birdcage coil. Figure **??** shows the types of birdcage coil with their electrical representation. In order for the birdcage to resonate and create a homogeneous magnetic field the current in the rungs must change phase incrementally from 0 to 2π,

$$I_n = I_0 \cos(\pi n/(N + \phi)), \tag{3.29}$$

where n is the rung number and ϕ is the spatial phase factor which is determined by the driving mode. The closer the current distribution on the rungs to a cosine function the better the magnetic field homogeneity, which is achieved by increasing the number of the rungs used. However, maintaining uniform current distribution while tuning and matching the coil is complicated at high

frequencies.

(a) Saddle Coil   (b) Slotted Tube Resonator (STR)

(c) Birdcage Coil
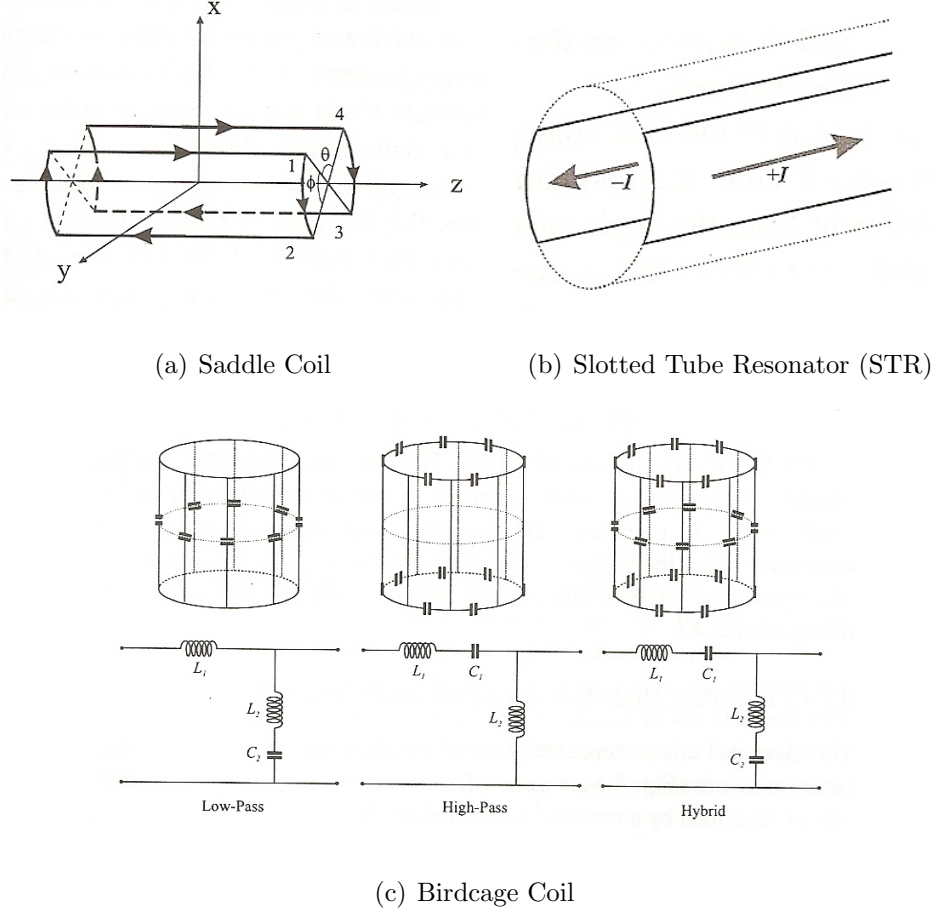
Figure 3.3: *Transverse RF coils [2].*

3.8.3 Surface Coils

A surface coil is placed directly next to tissues being imaged and is designed specifically for imaging superficial organs. In transmit-receive RF coils, volume coils are favourable because they generate a uniform magnetic field over the tissue's volume. However, in reception mode, noise from all the volume will be detected by the coil and added to the MR signal from the slice being selected. Therefore, surface coils have the benefit of acquiring high SNR from the nearby field of view (FOV). At Ultra-high frequency a coil's RF losses can be limited by reducing the physical length of the coil to $\lambda/10$ or less. For 7T (298 MHz) system, the size of surface coil is about a couple of cm in diameter.

The surface coil in its simplest shape is a circular loop which can be represented as a simple LC circuit. Distributing capacitors around the circumference of the coil improves the current distribution and increases the coil's operational frequency. When using a receive surface coil in combination with a transmit volume coil, the two coil could couple to each other. During transmission, a current induced on the surface of the coil and might causes skin burns while during reception, the volume coil could add noise to the signal detected. Therefore, a trap circuit and a PIN diode is used to detune either coils during transmission and reception.

In clinical MR systems, scans usually start with a large FOV because the region of interest is not usually precisely determined. Unfortunately, having a large FOV comes at the cost of low SNR when using a volume coil for reception; however, two possible solution can be applied. One is to use a surface coil repeatedly with different positions, which consumes time. The other solution is to use multiple surface coils which is called an array coil.

3.8.4 Array Coils

The main principle of an NMR array coil is based on combining simultaneous signals obtained from multiple coils to produce a single image. Therefore, a large field of view is covered while retaining a high SNR [22]. The main difficulty in designing array coils is to control coupling between array elements. When two coil elements are brought into proximity, the inductive coupling between the coil elements causes splitting of the resonant frequency; therefore, noise and signal transfer between elements degrades the sensitivity of the coil. The coupling between elements increases with the increase of the mutual inductance. The ionic currents in the tissues induce emf in arrays which in turn cause correlated noise in the coil. Consequently, SNR values decrease [22], [19]. One way to decouple arrays is by overlapping the neighbouring elements in an

attempt to reduce the mutual inductance to zero; however, it has the disadvantage of restricting the geometrical layout of array coils and it has no effect on the next nearest neighbouring array coupling. Therefore, the low impedance pre-amplifier has been suggested to reduce coupling. The low input impedance of the pre-amplifier prevents any induced emf, and therefore any currents to flow, by introducing a 'tank' circuit [22]. No signal or noise will be transferred between elements even though they are receiving signals independently. Another way is to build capacitive circuits between arrays to cancel out mutual inductance [13].

Array coil design can be categorized based on their geometrical arrangement of the coils. For example, for parallel MR imaging such as sensitivity encoding (SENSE) [20], array elements must be arranged such that the direction of under-sampling is coordinated in the same direction as the arrays' sensitivity variation. These elements are used to acquire intermediate under-sampled images. Such images are aliased because of overlap of signals from pixels outside the under-sampled field of view with signals from the imaging space. Therefore, the SENSE technique is used to unfold the aliased image and create a complete MR image using the complex sensitivity profile of each array element. Elements in the array can be arranged in a straight line array when maximum acquisition of spatial information is desired in one direction. Also, they can be arranged as a 2D grid and wrap-around arrays where they cover less field of view but have the virtue of multi-dimensional spatial encoding. Surface array coils with complex looping arrangements such as concentric and diagonal array design emphasise the phase variation in coils' sensitivity maps. Therefore, they are useful in unfolding aliased pixels with parallel reconstruction techniques such as Sensitivity Encoding (SENSE) and Partial Parallel Imaging with Localized Sensitivity (PILS), while also having the multi-directional spatial encoding ability. Volume coils can be adapted for parallel MRI if de-

signed as a set of independently driven elements and used for spatial encoding
[18].

Bibliography

[1] *Fundamental of physics*. New York: John Wiley and Sons, 1974.

[2] *NMR Probeheads for Biophysical and Biomedical Experiments*. Imperial College Press, 2006.

[3] Technical Report IEC 60601-2-33:2002. Medical electrical equipment part 2-33: Particular requirement for the safety of magnetic resonance equipment for medical diagnosis. Technical report, International Electrotechnical Commission, 2002.

[4] N. Chen, D. I. Hoult, and V. I. Sank. Quadrature detection coils - a further improvement in sensitivity. *J. Magn. Reson.*, 54:324–327, 1983.

[5] W. N. Hardy and L. A. Witehead. Split-ring resonator for use in magnetic resonance from 200-2000 mhz. *Rev. Sci. Instrum.*, 52:213–216, 1981.

[6] W. N. Hardy and L. A. Witehead. A double- tuned probe for metabolic nmr studies. *Mag. Reson. Med.*, 23:367–371, 1992.

[7] Roger F. Harrington.

[8] C. E. Hayes, W. A. Edelstein, W. A. Schenck, O. M. Mueller, and M. Eash. An efficient, highly homogeneous radiofrequency coil for whole-body nmr imaging at 1.5t. *J. Magn. Reson.*, 63:622–628, 1985.

[9] D. I. Hoult. The principle of reciprocity in signal strength calculations: a mathematical guide. *Conc. Magn. Reson.*, 12(4):173–187, 2000.

[10] D. I. Hoult and R. Deslauriers. A high-sensitivity, high-b_1 homogeneity probe for quantitation of metabolites. *Mag. Reson. Med.*, 16:411–417, 1990.

[11] D. I. Hoult and R. E. Richards. The signal-to-noise ratio of the nuclear magnetic resonance experiment. *J. Magn. Reson*, 24:71–85, 1976.

[12] T. S. Ibahim, R. Lee, B. A. Baertlein, A. Kangarlu, and P. M. L. Robitaille. Comparison between linear, quadrature and 4-port excitations from 1.5 t to 4.7 t. ISMRM, 1999.

[13] J. Jevtic. Ladder networks for capacitive decoupling in phased-array coils. 2001.

[14] A. Kangarlu, T. Ibrahim, and F. Shellock. Effects of coil dimensions and field polarization on rf heating inside a head phantom. *Magn. Res. Imag.*, 2005.

[15] L. Libby. Special aspects of balanced shielded loops. In *Proceeding of the I. R. E. and Waves and Electrons*, pages 641–646, 1945.

[16] Arthur W. Magill. *Ultra-High Frequency Magnetic Resonance Imaging.* PhD thesis, School of physics and Astronomy, University of Nottingham, 2006.

[17] J. Mispelter, M. Lupu, and A. Bringuet. *NMR probheads for biophysical and biomedical experiments: theoretical principles and practical guidelines.* Imperial College Press, 2006.

[18] M. A. Ohliger and D. K. Sodickson. An introduction to coil array design for parallel mri. *NMR in Biomedicine*, 19:300–315, 2006.

[19] R. G. Pinkerton, E. A. Barberi, and R. S. Menon. Noise properties of a nmr transceiver coil array. *J. Magn. Reson.*, 171:151–156, 2004.

[20] K. P. Pruessmann, M. Weiger, M. B. Scheidegger, and Peter Boesiger. Sense: Sensitivity encoding for fast mri. *Mag. Reson. Med.*, 42, 1999.

[21] Simon Ramo, John R. Whinnery, and Theodore Van Duzer. *Fields and Waves in Communication Electronics.* John Wiley and sons Inc., 1994.

[22] P. B. Roemer, W. A. Edelstein, C. E. Hayes, S. P. Souza, and O. M. Muller. The nmr phase array. *Mag. Reson. Med.*, 16:192–225, 1990.

[23] H. J. Schneider and P. Dullenkopf. Slotted tube resonator: A new nmr probe head at high observing frequencies. *Rev. Sci. Instrum.*, 48:68–73, 1977.

[24] J. Vaughan, G. Adriany, E. Yacoub, T. Duong, L. DelaBarre, P. Andersen, and K. Ugurbil. A detunable tem volume coil for high field mri. *Mag. Reson. Med.*, 47:990–1000, 2002.

Chapter 4

Electromagnetic Modelling

Techniques

4.1   Introduction

RF coil designs and coil-tissue interactions at low magnetic field strength (less than 3T (128 MHz)) have been studied using circuit concepts and transmission line theory. At such low frequencies, circuit concepts can be used to determine the proposed RF coil resonant frequency and magnetic field patterns using the Biot-Savart law and by assuming a uniform current distribution for the coil. However, for higher strengths the quasi-static approximations start to fail as the geometric dimensions of the RF wavelengths become significant. Moreover, the presence of body tissue in loaded coils deteriorates the fields even faster and the B_1 field homogeneity worsens with the increase of resonant frequency. Hence, these effects lead to localized heat (hot spots) due to absorption in tissues. As a result of the failure of quasi-static approximations, numerical tool methods such as full wave methods become vital in designing and optimising the performance of RF coils.

One of the most used full wave methods in RF coil design and coil-tissue inter-

actions is the finite-difference time domain (FDTD) method introduced by Yee in 1966. The FDTD method solves time dependent Maxwell equations for electric and magnetic fields. The problem space is converted into a regular mesh which consists of small Yee cells. The electric and magnetic field are calculated at alternate half time steps in an iterative process until a stable solution is reached. There have been numerous applications of the FDTD methods in RF coil design and field interactions. For instance, using the FDTD method, Collins et al.[5] have calculated the B_1 field, SAR and SNR for a surface coil positioned on the surface of an anatomically accurate human chest. Wang et al.[16] calculated the amount of power radiated and dissipated by a surface coil loaded with different samples at different frequencies. Collins el. al. [6] in 2003 did the FDTD calculations to study the effect of the cell size on the accuracy of local and average SAR calculations. A year later, Collins et al.[4] calculated SAR values for the human head in three different coils: a Birdcage coil operating at 1.5 T (64 MHz), and a quadrature surface coil, and a TEM coil both operating at 7 T (300 MHz). Also, a 12 element birdcage coil has been designed and the SNR, SAR and B_1 fields were calculated at a rang of frequencies up to 345 MHz for quadrature excitation [3].

The biconjugate gradient algorithm in combination with the fast Fourier transform was used by Jin et al.[11](1996) to compute B_1 fields, and SAR values for a birdcage coil, linearly and quadratically excited at three different frequencies: 64 MHz (1.5 T), 128 MHz (3T) and 256 MHz (6T). The FDTD method in combination with the method of moments (MOM) was used by Chen et al.[1] to model a shielded end cap birdcage coil at four different frequencies, (64 MHz, 128 MHz, 171 MHz and 256 MHz), at which B_1 field distribution and SAR values were calculated. The transmission line modelling TLM introduced by John in 1974 is also applied in electromagnetic interactions such as the effect of power lines on the body[8] and the SAR values for mobile phone antennas

[9]. Most recently, it has been applied to modelling B_1 field distribution, field inhomogeneity, SAR and SNR values for birdcage coils at ultra high frequency [12].

4.2   Finite Difference Time Domain (FDTD) Method

This section will give a brief overview for the most popular full wave methods: Finite-difference time domain method (FDTD) and Transmission Line Modelling (TLM). Part of the work presented in this thesis was carried out on transmission line method in-house code and the other part is carried out on a commercial FDTD package, xFDTD (Remcom).

4.2.1   Yee's Finite Difference Algorithm

The FDTD method is based on replacing differential Maxwell's equations for an isotropic, homogeneous medium with the central finite difference approximation of second order accuracy. Therefore, the problem space is discretized into a $3D$ grid and initial conditions are applied, mostly by assuming equal field values everywhere in space. Hence, excitation is applied and the fields' components are calculated at future time steps in an iterative process until a steady state is reached.

The Maxwell curl equations for an isotropic, homogeneous medium are given as:

$$
\begin{aligned}
\frac{\partial \mathbf{B}}{\partial t} &= -\nabla \times \mathbf{E}\,, \\
\frac{\partial \varepsilon \mathbf{E}}{\partial t} &= -\sigma \mathbf{E} + \frac{\nabla \times \mathbf{B}}{\mu}\,,
\end{aligned}
\tag{4.1}
$$

where $\mathbf{B}$ is the magnetic induction, $\mathbf{E}$ is the electromagnetic field, t is the time, σ is the electrical conductivity, ε is the electrical permittivity, $\varepsilon = \varepsilon_r \varepsilon_0$,

and μ is the magnetic permeability equal to that of air for biological tissues.

Rewriting these equations in term of curl equation definitions gives

$$
\begin{aligned}
\frac{\partial B_x}{\partial t} &= -\left(\frac{\partial E_z}{\partial y} - \frac{\partial E_y}{\partial z}\right), \\
\frac{\partial B_y}{\partial t} &= -\left(\frac{\partial E_x}{\partial z} - \frac{\partial E_z}{\partial x}\right), \\
\frac{\partial B_z}{\partial t} &= -\left(\frac{\partial E_y}{\partial x} - \frac{\partial E_x}{\partial y}\right), \\
\frac{\partial \varepsilon E_x}{\partial t} &= -\sigma E_x + \frac{1}{\mu}\left(\frac{\partial B_z}{\partial y} - \frac{\partial B_y}{\partial z}\right), \\
\frac{\partial \varepsilon E_y}{\partial t} &= -\sigma E_y + \frac{1}{\mu}\left(\frac{\partial B_x}{\partial z} - \frac{\partial B_z}{\partial x}\right), \\
\frac{\partial \varepsilon E_z}{\partial t} &= -\sigma E_z + \frac{1}{\mu}\left(\frac{\partial B_y}{\partial x} - \frac{\partial B_x}{\partial y}\right).
\end{aligned}
\tag{4.2}
$$

According to the Yee method, the problem space can be redefined as a 3D grid of cubic cells, with each grid point defined as

$$
(i, j, k) = (i\Delta x, j\Delta y, k\Delta z),
$$

and, any function of space and time defined as

$$
F^n(i, j, k) = F(i\Delta x, j\Delta y, k\Delta z, n\Delta t) \quad,
$$

where $\Delta x, \Delta y, \Delta z$ are the spatial increments in the x, y and z directions and Δt is the time step. In terms of magnetic and electric field, the function $F \equiv (H or E)$ fields. For cubic cells, the spacing in all dimensions are equal so $\Delta x = \Delta y = \Delta z = \delta$. Therefore, the general definitions of Maxwell's time and space derivatives in terms of the central difference approximation of second order accuracy using Taylor's series are given as [15]

$$
\begin{aligned}
\frac{\partial F^n(i, j, k)}{\partial x} &= \frac{F^n(i + 1/2, j, k) - F^n(i - 1/2, j, k)}{\delta} + O(\delta^2), \\
\frac{\partial F^n(i, j, k)}{\partial t} &= \frac{F^{n+1/2}(i, j, k) - F^{n-1/2}(i, j, k)}{\Delta t} + O(\triangle t^2).
\end{aligned}
\tag{4.3}
$$

The terms $O(\delta^2)$ and $O(\triangle t^2)$ represent errors in the central difference approximation as a result of truncating the series. These terms can be dropped by

assuming that they are negligibly small. Hence,

$$
\begin{aligned}
\frac{\partial F^n(i,j,k)}{\partial x} &= \frac{F^n(i+1/2,j,k) - F^n(i-1/2,j,k)}{\delta}, \\
\frac{\partial F^n(i,j,k)}{\partial t} &= \frac{F^{n+1/2}(i,j,k) - F^{n-1/2}(i,j,k)}{\triangle t}.
\end{aligned}
\tag{4.4}
$$

Applying equation (4.4) to (4.2), the finite difference approximation equations for the field components are:

$$
\begin{aligned}
H_x^{n+1/2}(i,j+1/2,k+1/2) = &\; H_x^{n-1/2}(i,j+1/2,k+1/2) \\
&+ \frac{\delta t}{\mu(i+1/2,j,k+1/2)\delta} \big[E_y^n(i,j+1/2,k+1) \\
&\qquad\qquad\qquad\qquad\qquad - E_y^n(i,j+1/2,k) \\
&\quad + E_z^n(i,j,k+1/2) - E_z^n(i,j+1,k+1/2) \big],
\end{aligned}
\tag{4.5}
$$

$$
\begin{aligned}
H_y^{n+1/2}(i+1/2,j,k+1/2) = &\; H_y^{n-1/2}(i+1/2,j,k+1/2) \\
&+ \frac{\delta t}{\mu(i+1/2,j,k+1/2)\delta} \big[E_z^n(i+1,j,k+1/2) \\
&\qquad\qquad\qquad\qquad\qquad - E_z^n(i,j,k+1/2) \\
&\quad + E_x^n(i+1/2,j,k) - E_x^n(i+1/2,j,k+1) \big],
\end{aligned}
\tag{4.6}
$$

$$
\begin{aligned}
H_z^{n+1/2}(i+1/2,j+1/2,k) = &\; H_z^{n-1/2}(i+1/2,j+1/2,k) \\
&+ \frac{\delta t}{\mu(i+1/2,j+1/2,k)\delta} \big[E_x^n(i+1/2,j+1,k) \\
&\qquad\qquad\qquad\qquad\qquad - E_x^n(i+1/2,j,k) \\
&\quad + E_y^n(i,j+1/2,k) - E_y^n(i+1,j+1/2,k) \big],
\end{aligned}
\tag{4.7}
$$

$$
\begin{aligned}
E_x^{n+1}(i+1/2,j,k) = &\left(1 - \frac{\sigma(i+1/2,j,k)\delta t}{\varepsilon} \right) \cdot E_x^n(i+1/2,j,k) \\
&+ \frac{\delta t}{\varepsilon(i+1/2,j,k)\delta} \big[H_z^{n+1/2}(i+1/2,j+1,k) \\
&\qquad\qquad\qquad\qquad\qquad - H_z^{n+1/2}(i+1/2,j-1/2,k) \\
&\qquad\qquad\qquad\qquad\qquad + H_y^{n+1/2}(i+1/2,j,k-1/2) \\
&\qquad\qquad\qquad\qquad\qquad - H_y^{n+1/2}(i+1/2,j,k+1/2) \big],
\end{aligned}
\tag{4.8}
$$

$$E_y^{n+1}(i, j + 1/2, k) = \left(1 - \frac{\sigma(i, j + 1/2, k)\delta t}{\varepsilon}\right) \cdot E_y^n(i, j + 1/2, k)$$
$$+ \frac{\delta t}{\varepsilon(i, j + 1/2, k)\delta} \left[H_x^{n+1/2}(i, j + 1/2, k + 1/2)\right.$$
$$- H_x^{n+1/2}(i, j + 1/2, k - 1/2) \quad (4.9)$$
$$+ H_z^{n+1/2}(i - 1/2, j + 1/2, k)$$
$$\left. - H_z^{n+1/2}(i + 1/2, j + 1/2, k)\right],$$

$$E_z^{n+1}(i, j, k + 1/2) = \left(1 - \frac{\sigma(i, j, k + 1/2)\delta t}{\varepsilon}\right) \cdot E_z^n(i, j, k + 1/2)$$
$$+ \frac{\delta t}{\varepsilon(i, j, k + 1/2)\delta} \left[H_y^{n+1/2}(i + 1/2, j, k + 1/2)\right.$$
$$- H_y^{n+1/2}(i - 1/2, j, k + 1/2) \quad (4.10)$$
$$+ H_z^{n+1/2}(i, j - 1/2, k + 1/2)$$
$$\left. - H_z^{n+1/2}(i, j + 1/2, k + 1/2)\right].$$

The electric and magnetic fields components are staggered in Yee cells at a half spatial increment (cell) from each other. Figure 4.1 shows the electric field components positioned at the centre of the cell edges pointing in the direction of the coordinate, while magnetic field components are at the centre of each face and pointing in a direction perpendicular to each face of the cell. Applying the initial values of fields at times n and $n - 1/2$, the magnetic and electric field components are evaluated at $n + 1/2$ and $n + 1$, respectively, where the fields are spatially $1/2$ step offset. For example, field components (H_x, H_y, H_z) are calculated at time step $n + 1/2$ using known field component values at previous time steps n and $n - 1/2$. These field components are then used to calculate the electric field components (E_x, E_y, E_z) at next time step $n + 1$.
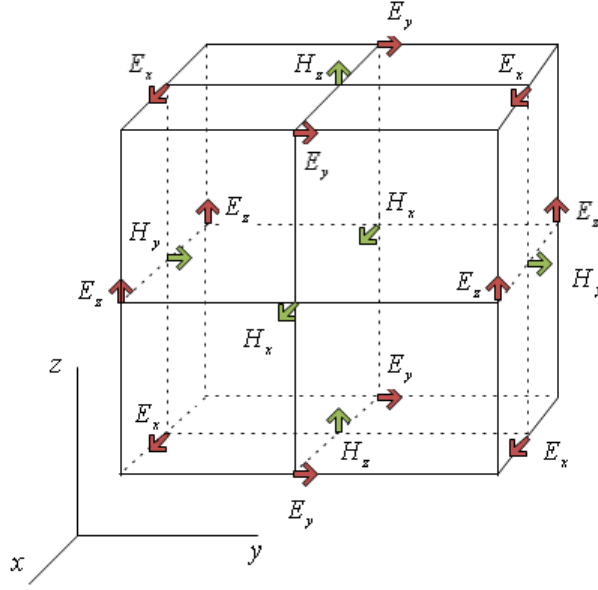
Figure 4.1: *Position of field components on the Yee cell*

4.2.2 Accuracy and Stability

As has been mentioned, the FDTD approximation is of a second order accuracy, which means that the first error term is proportional to the square of δ. Therefore, to ensure an accurate computational result the spatial increments have to be as small as possible. Usually, the physical system is discritzed as 10 cells or more per one wavelength corresponding to the maximum frequency,

$$\delta \leq \lambda/10 \qquad \text{(for the shortest wavelength } \lambda) \quad .$$

In order to ensure stability of the calculations the time step should be chosen such that the electromagnetic fields pass through one grid cell in a single iteration. So, the stability condition that must be satisfied is [15]

$$u_{max}\Delta t \leq 1/\sqrt{\frac{1}{\Delta x^2 + \Delta y^2 + \Delta z^2}}, \qquad (4.11)$$

where u_{max} is the maximum wave velocity in the model. For a cubic grid, the stability condition becomes

$$u_{max}\Delta t \leq \delta/\sqrt{3}. \qquad (4.12)$$

The FDTD algorithm equations (4.5) to (4.10) calculate the electric and magnetic field at half time step interval from each other for one complete iteration. The time step calculation depends on the cell size and speed of the propagating wave though the medium. The smaller the cell size the larger the number of calculations per iteration, the larger the memory requirements, and duration of the simulation. In MRI applications, the human body model should be a 5 mm grid or less which then meets the stability condition for high MRI frequencies (~ 300 MHz) and ensures accuracy of calculations.

4.3 The Transmission Line Modeling

The transmission line matrix method is a time domain numerical technique that solves EM field problems at high frequencies by drawing the analogue between Maxwell's equations and voltages and currents for two parallel transmission lines. In this technique, the physical system is discretized to a mesh of lumped elements where the electrical components reflect the physical property of the system and the behaviour of the electromagnetic fields through it. Therefore, the TLM method can be summarized as:

- Discretize the field problem to the equivalent lumped elements network.

- Solve the network by iterative method.

- Draw the analogy between Maxwell's fields and circuit elements for the calculation of fields.

4.3.1 Scattering and Connections

In a similar analogy to Huygens principle voltage pulses incident on the transmission line grid nodes are reflected back and scattered toward the adjacent nodes which in turn will propagate and scatter the new incident pulses. Voltage

pulses continue to propagate and scatter across the TLM grid until a solution is obtained.

Consider an incident voltage pulse $_kV^i$ at time step k which is incident upon a node in which its all linked lines impedances are known, then the scattered and reflected pulses are related to the incident through the scattering matrix S_k as,

$$_kV^r = S_kV^i. \tag{4.13}$$

The scattered pulses from the node will travel toward their immediate neighbours and become an incident on those nodes at the next time step $k+1$, the reflected pulses at time step k are related to the incident on the nearest neighbours through the connection matrix C_k as

$$_{k+1}V^i = C_kV^r. \tag{4.14}$$

In the 3D network representation physical problems can be represented by a number of nodes; however, the most widely used is the Symmetrical Condensed Node (SCN) shown in figure 4.2. Each SCN is a network of interconnected lines where there are two orthogonal ports on each face of the cell. Hence, it has 12 voltage ports labelled from 1-12 in a traditional labelling scheme. The voltage at each port is also labelled by three subscripts, the first defines the direction of propagation (x,y, or z), the second defines the position of the link line whether in the positive or the negative direction(p, or n), the third gives the polarization of the pulses. A superscript is also added to define the reflected and incident pulses (r or i) [2]. For example, V_{xpy}^i is an incident y-polarized voltage pulse on the positive x branch of the node.

The scattering matrix for a homogeneous medium is first considered; where C, L is the total capacitance and inductance of the link line. Four conditions have to be applied in order to drive the scattering. They are:

- Conservation of electric charge

- Conservation of magnetic flux

- Continuity of electric field

- Continuity of magnetic field

Applying all four conditions give 12 equations relating the incident voltage components to the reflected ones, as follows:

$$V_{ynx}^r = V_x - Z_0 I_z - V_{ypx}^i$$

$$V_{ypx}^r = V_x - Z_0 I_z - V_{ynx}^i$$

$$V_{znx}^r = V_x - Z_0 I_y - V_{zpx}^i$$

$$V_{zpx}^r = V_x - Z_0 I_y - V_{znx}^i$$

$$V_{zny}^r = V_y - Z_0 I_x - V_{zpy}^i$$

$$V_{zpy}^r = V_y - Z_0 I_x - V_{zny}^i \,,$$

$$V_{xny}^r = V_y - Z_0 I_z - V_{xpy}^i$$

$$V_{xpy}^r = V_y - Z_0 I_z - V_{xny}^i$$

$$V_{xnz}^r = V_z - Z_0 I_y - V_{xpz}^i$$

$$V_{xpz}^r = V_z - Z_0 I_y - V_{xpz}^i$$

$$V_{ynz}^r = V_z - Z_0 I_x - V_{ypz}^i$$

$$V_{ypz}^r = V_z - Z_0 I_x - V_{ynz}^i$$

(4.15)

where $V_{x,y,z}$ are the node voltages,

$$V_x = \frac{1}{2}(V_{ypx}^i + V_{zpx}^i + V_{ynx}^i + V_{znx}^i)$$

$$V_y = \frac{1}{2}(V_{zpy}^i + V_{xpy}^i + V_{zny}^i + V_{xny}^i) \,,$$

$$V_z = \frac{1}{2}(V_{ypx}^i + V_{zpx}^i + V_{ynx}^i + V_{znx}^i)$$

(4.16)

$I_{x,y,z}$ are the loop current.

$$I_x = \frac{1}{2Z_0}(V_{ypz}^i - V_{zpy}^i - V_{ynz}^i + V_{zny}^i)$$

$$I_y = \frac{1}{2Z_0}(V_{zpx}^i - V_{xpz}^i - V_{znx}^i + V_{xnz}^i) \,,$$

$$I_z = \frac{1}{2Z_0}(V_{xpy}^i - V_{ypx}^i + V_{xny}^i + V_{ynx}^i)$$
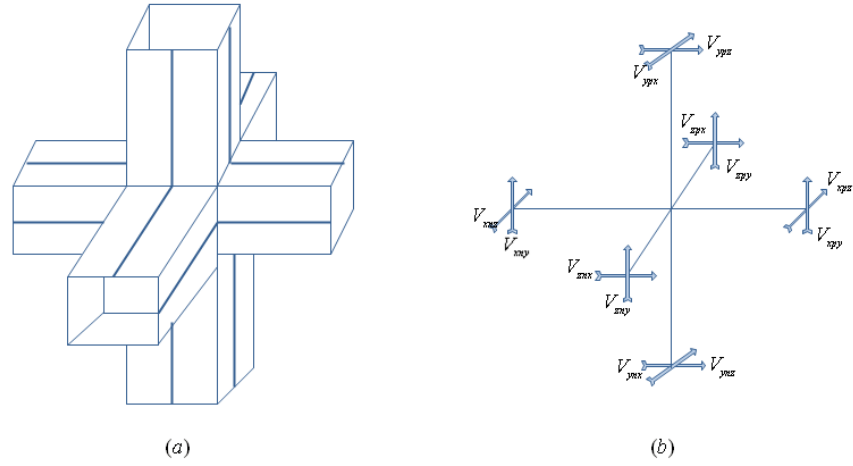
(4.17)

Figure 4.2: *The TLM SC Node, (a) structure representation; (b) Voltage pulse notations.*

4.3.2 Modelling an Inhomogeneous Medium, the Stability and Mesh Parameters

When modelling a physical medium, it is important to choose the spacing between the nodes so it can accommodate details of the model and the shortest wavelength of interest. Hence, it is recommended that

$$\Delta l \leq \lambda/10. \tag{4.18}$$

The mesh spacing Δl and the transmission line velocity u_{TL} determine the timestep Δt as

$$\Delta t = \Delta l/u_{TL}. \tag{4.19}$$

Decreasing the timestep increases the spatial resolution of the problem space and decreases the modelling error. However, the available computer's memory storage and the running time are crucial factors in determining Both Δl and Δt. The transmission lines' velocity u_{TL} is related to the wave propagation velocity as

$$u = \frac{u_{TL}}{2}, \tag{4.20}$$

for a homogeneous isotropic medium, vacuum, $u = c$, where c is the velocity of light. However, most physical systems are inhomogeneous: for example, body tissues are modelled as inhomogeneous media where tissues are considered conductive and capacitive. In such a mixed material, the velocity of the wave changes as it travels from one medium (air) to another. Changing the capacitance and inductance of the link lines to account for the permittivity ε and permeability μ changes will affect the simulation synchronism, equation (4.20), and the timestep Δt will be different in different materials. Moreover, changing the spacing Δl will affect the scattering process, and there might be places on the grid where the correspondence of one link line to another is lost. One way to overcome this is to consider a medium with free space

background materials and add stub lines that model the extra capacitors and inductors where the materials are heterogeneous, see figure 4.3. The stub lines are one-port transmission lines with their lengths adjusted so that a voltage pulse entering one stub line is reflected back to reach the node at time step Δt. Hence, synchronism is maintained. To model an extra capacitance, ε_r, the stub line has to have an open circuit termination whereas in modelling an extra inductance, μ_r, a short circuit termination is required. The ohmic losses are modelled by adding an infinitely long resistive line so voltage pulses will be absorbed out of the system.
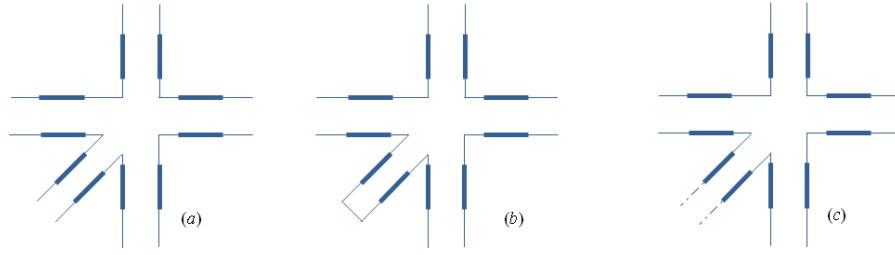

Figure 4.3: *2D TLM node representation showing: (a) Capacitative, (b) Inductive and, (c) Lossy stubs.*

Accordingly, three equations are added to the scattering matrix to account for the dielectric stubs,

$$V_{sx}^r = V_x - V_{sx}^i,$$
$$V_{sy}^r = V_y - V_{sy}^i, \tag{4.21}$$
$$V_{sz}^r = V_z - V_{sz}^i.$$

Voltage pulses entering the resistive stubs are never reflected back, so their scattering is not calculated. However, their effects are accounted for in the

nodal voltages. Equation (4.15) is replaced by

$$V_x = \frac{2}{4 + \hat{Y}_x^s + \hat{G}_x^s} \left(V_{ypx}^i + V_{zpx}^i + V_{ynx}^i + V_{znx}^i + \hat{Y}_x^s V_{sx}^i \right),$$

$$V_y = \frac{2}{4 + \hat{Y}_y^s + \hat{G}_y^s} \left(V_{zpy}^i + V_{xpy}^i + V_{zny}^i + V_{xny}^i + \hat{Y}_y^s V_{sy}^i \right), \qquad (4.22)$$

$$V_z = \frac{2}{4 + \hat{Y}_z^s + \hat{G}_z^s} \left(V_{xpz}^i + V_{ypz}^i + V_{xnz}^i + V_{ynz}^i + \hat{Y}_z^s V_{sz}^i \right),$$

where $\hat{Y}^s$ and $\hat{G}^s$ are normalized admittance and conductivity of the dielectric and lossy stubs, given as

$$\hat{Y}_m^s = 4(\varepsilon_r - 1),$$
$$\hat{G}_m^s = \frac{\sigma_m \Delta l}{\hat{Y}^0}, \qquad (4.23)$$

where $m = x, y$ or z.

4.3.3   TLM Output fields

The electric and magnetic fields can be calculated at either node or link lines from the scattered and reflected voltages and circulating currents in the grid. The electric field components across nodes are

$$E_x = -\frac{V_x}{\Delta x} = -\frac{V_{ypx}^i + V_{zpx}^i + V_{ynx}^i + V_{znx}^i}{2\Delta x},$$

$$E_y = -\frac{V_y}{\Delta y} = -\frac{V_{zpy}^i + V_{xpy}^i + V_{zny}^i + V_{xny}^i}{2\Delta y}, \qquad (4.24)$$

$$E_z = -\frac{V_z}{\Delta z} = -\frac{V_{xpz}^i + V_{ypz}^i + V_{xnz}^i + V_{ynz}^i}{2\Delta z}.$$

The magnetic field components are calculated from the current circulating around the node as

$$B_x = -\frac{\mu_0 I_x}{\Delta x} = -\frac{\mu_0}{2Z_0 \Delta x} \left(V_{ypz}^i - V_{zpy}^i - V_{ynz}^i + V_{zny}^i \right),$$

$$B_y = -\frac{\mu_0 I_y}{\Delta y} = -\frac{\mu_0}{2Z_0 \Delta y} \left(V_{zpx}^i - V_{xpz}^i - V_{znx}^i + V_{xnz}^i \right), \qquad (4.25)$$

$$B_z = -\frac{\mu_0 I_z}{2Z_0 \Delta z} = -\frac{\mu_0}{2Z_0 \Delta z} \left(V_{xpz}^i + V_{ypz}^i + V_{xnz}^i + V_{ynz}^i \right).$$

4.4 Excitation of the Fields

In an electromagnetic field simulation, a sinusoidal function can be used for acquiring a steady state response. Ports are excited with either current or voltage sources with amplitude A, frequency f and phase ϕ as $A\sin(2\pi ft+\phi)$. An impulse function or Guassian pulse can be used to excite a wide range of frequencies. The Fourier Transform of the temporal fields provides the resonant frequencies of the system.

This work is concerned with the response at 298 MHz corresponding to 7 T. Therefore, most of the TLM simulations are done with 1 V or 1 A excitation at two different phases 0 and $\pi/2$ for quadrature excitation at a single frequency. Other phase shifts were used to simulate the multiple transmit elements.

4.5 Boundary Conditions

All physical problems that deal with electromagnetic simulation techniques have a defined space where pulses scattered at the boundaries have to be terminated properly for stability to be maintained. The simplest boundary condition is the absorbing boundary where all incoming waves are absorbed. A Perfectly Matched Layer (PML) can be also used where all pulses at any angle are absorbed. The absorbing boundary is the choice for most simulations in this study in all directions.

The boundaries may also be terminated with a perfect conducting surface, Perfect Electric Conductor (PEC) or Perfect Magnetic Conductor (PMC), which will reduce the run time and memory storage providing that the problem modelled is symmetric. For example, a PEC is used for shielded field structure.

4.6 Numerical Calculation of B_1 Fields and SAR

It has been mentioned in section 3.2, that the rotating RF field may have com-
ponents which are oppositely rotating, one is coupled to spins in the transmis-
sion mode and the other is coupled to spins in the reception mode. The two
field components can be written in terms of the transverse field components by
comparing two snapshots of the magnetic field at two instants of time with one
a quarter of a cycle ahead of the other. Then the rotating field components in
equation (2.5) can be written as

$$B_1^+ = \frac{1}{2}\left(B(t) - i \cdot B(t + \tau_{\pi/2})\right),$$
$$B_1^- = \frac{1}{2}\left(B(t) + i \cdot B(t + \tau_{\pi/2})\right),$$

(4.26)

where B_1^+ is the transmit rotating magnetic field and is rotating in the same
sense as the spins, B_1^- is the receive rotating component and is rotating in the
opposite sense to the spins, and $B(t)$ is the transverse magnetic field,

$$B(t) = B_x(t) + i \cdot B_y(t),$$

(4.27)

and $\tau_{\pi/2}$ is the duration of a quarter of a cycle. The B_z component can be
ignored since it has a small value in comparison to the transverse components
and it does not contribute to the NMR spins. However, all the electric field
components contribute to the SAR calculation as

$$SAR = \frac{\sigma(E_x^2 + E_y^2 + E_z^2)}{2\rho}.$$

(4.28)

$E_{x,y,z}$ are the peak values.

4.7 High Field Effect

4.7.1 Material Properties

The effect of electric tissue properties ε_r and σ can no longer be ignored in the
frequency range 64 MHz to 340 MHz, where tissues cannot be considered as

either a good conductor or a dielectric. The tissue permeability μ_r may play a role in affecting static magnetic field homogeneity, causing image artifact and detecting physiological information, but its effect on the rotational RF field is of the order 10^{-6} times the applied field.

Field penetration and attenuation is largely affected by the applied field frequency and the biological tissue shape and properties. Both permittivity and conductivity of tissues are a function of frequency. It is well known that an applied rotational field B_1 is associated with an oscillating electric field. Hence, a conduction current is generated as a result of the translation of charges and rotational motion of molecules which is related to the electric field by tissue conductivity. Therefore, fields are attenuated in tissues.

At low frequencies, charges accumulate at the edge of cell membranes and dipoles align with the field causing field polarization proportional to tissue permittivity. Therefore, with time, currents decrease and polarization increases. As the frequency increases toward the upper limit of RF frequencies, charges and dipoles oscillate fast and the conduction current increases, which in turn increases conductivity and decreases permittivity.

4.7.2 Wavelength and Penetration Depth

The wavelength in biological tissues with relative permeability μ_r and permittivity ε_r is calculated as

$$\lambda = \frac{\lambda_0}{\sqrt{\mu_0 \varepsilon_r}}, \tag{4.29}$$

where λ_0 is the free space wavelength. The relative permeability is approximately equal to 1. In general, as frequency increases wavelength decreases. The reduction of wavelength is enhanced with the presence of tissue with high permittivity values. For example, using tissue properties of the brain in table 4.1 at two frequencies 64 MHz and 256 MHz, wavelength is reduced in these

tissues by a factor of 8 compared with the free space value at 256 MHz and is reduce for by a factor of 3.5 compared with the wavelength in free space' at 64 MHz.

The penetration depth in tissue is also decreased as the frequency increases. The penetration depth is defined as the distance in the direction of field propagation at which the field values reduce to e^{-1} of the initial value at reference position and is given by

$$\eta = \sqrt{\frac{2}{\omega \mu_0 \sigma}}.$$ (4.30)

The decrease in field penetration is evident in tissues with relatively high conductivity such as the heart and blood.

4.7.3   Central Brightening

It is believed that the existence of central brightening, which is a major artifact in head MRI at 7 T, is not explicitly a result of dielectric presence. The geometry of the RF coil, the RF coil/tissue interaction and the shape and properties of tissues are all factors that contribute to such phenomena and affect the electromagnetic wave behaviour.

An empty hybrid birdcage body coil with uniform current distribution at 298 MHz will show central brighting in the middle of the coil as a result of field interference effects, but not at low frequency excitation such as 64 MHz. In such coils, each drive element with an amplitude and phase opposes another one with same amplitude and opposite phase. Therefore, fields from different elements sum in a constructive and destructive fashion giving rise to high field values at some points and low values at quarter wave length distance. When the coil is loaded with the body, wavelengths become shorter and the central brightening becomes more evident at low frequencies such as 64 MHz. However, at high frequencies this effect is evident in head coils where coil size is

comparable to the wavelength of the B_1 field at such a frequency.

Several approaches have been considered to overcome such artifacts including parallel imaging in reception mode, RF shimming and transmit Sensitivity Encoding technique (transmit SENSE). The next chapter will discuss the RF shimming approach from the electromagnetic wave point of view as a possible solution for reducing the central brightening pattern and generating a homogeneous B_1^+ field.

4.8   Simulation of 2-Dimensional Birdcage Coil Using TLM Techniques

In this section, the in-house built 3D TLM code [14] is tested by modelling a 2D bidcage-like coil at four different frequencies. The code was provided by the George Green Institute for Electromagnetics Research (GGIEMR) [14] and altered to read the head model by the electromagnetic group in the Sir Peter Mansfield Magnetic Resonance Centre (SPMMRC), Nottingham. The transmit B_1 field maps as well as field inhomogeneity and SAR values are calculated for linear and quadrature excitation. The results are validated against previous study which developed a finite element method (FEM) to analyse the SAR and B_1 field in a 2D bidcage model loaded with two different head slices [10].

4.8.1   The Birdcage-like coil description

A 2D birdcage-like model has been simulated as an axial slice of a 3D model. The slice is of 2 mm thickness. The mesh is $200 \times 200 \times 1$ dimension with 2 mm voxels. The simulated coil has a 17.5 cm radius and consists of 16 elements (rungs) which are modelled as voltage sources. The rungs are surrounded

with a copper shield of 20.4 cm radius with 2.3 cm thickness. The electrical property of the shield has the advantage of reducing the simulation time as fields' calculations are terminated at the shield boundary. The run time is about 20 minutes for each slice at a single resonant frequency. The coil is operated at four different frequencies: 64 MHz, 128 MHz, 171 MHz and 256 MHz, which are the resonant frequencies 1.5 T, 3 T, 4 T and 6 T systems. The electrical data for the head slices used in the validation are only available for these four frequencies. Therefore, the TLM in-house built code cannot be validated at the 7 T system resonant frequency.

4.8.2 2D Head Model

In order to study the electromagnetic interactions inside the head and SAR level a 2D head slice was used in combination with the birdcage-like coil. The head slice used in the simulation passes through the middle of the brain with 2 mm resolution. The slice was extracted from a head model by segmenting MRI images into cubic voxels and is provided by the National Radiological Protection Board of UK [7]. Each voxel is tagged with a type of tissue and its properties. It consists of nine different type of tissues. These are skin, muscle, bone, brain, cerebrospinal fluid (CSF), sinuses (air), lens, vitreous, Sclera (muscle), humour and cartilage. Figure 4.4 shows the tissue distribution in the head. The material proprieties of these tissues $\rho \times 10^3 (Kg/m^3)$, $\varepsilon_r = \varepsilon/\varepsilon_0$ and σ (S/m) are given in table 4.1.
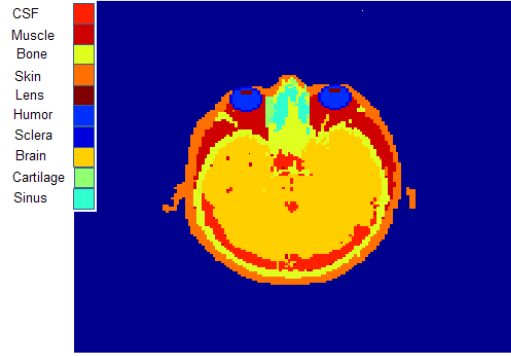
Figure 4.4: *2D head slice passes through the eyes with nine different tissue types given in table 4.1.*

Tissue Type	ρ	64MHz		128MHz		171MHz		256MHz	
		ε_r	σ	ε_r	σ	ε_r	σ	ε_r	σ
CSF	1.06	106	0.62	103	0.7	101	0.73	100	0.8
Air		1	0	1	0	1	0	1	0
Muscle	1.04	85	0.89	65	1.3	61	1.3	55	1.3
Sclera	1.04	85	0.89	65	1.3	61	1.3	55	1.3
Bone	1.85	26	0.04	25	0.05	24	0.05	22	0.06
Skin	1.1	73	0.73	63	0.86	60	0.87	53	0.7
Lens	1.05	46	0.45	35	0.45	35	0.46	34	0.48
Humor	1.01	100	1.9	73	1.7	73	1.3	73	1.75
Brain	1.03	88	0.49	70	0.57	69	0.58	68	0.6
Cartilage	1.1	26	0.04	25	0.05	24	0.05	22	0.06

Table 4.1: *Tissue properties [10], $\rho \times 10^3 \ (Kg/m^3)$, $\varepsilon_r = \varepsilon/\varepsilon_0$ and $\sigma \ (S/m)$.*

4.8.3 Excitation Method (Linear Vs. Quadrature)

The most popular method of excitation used in birdcage probes is quadrature excitation. Using quadrature excitation at low frequencies generates a circularly polarized field which is more homogeneous than the linearly polarized field generated by linear excitation. Exciting the coil linearly requires a single point drive point while driving the coil in quadrature mode involves more complicated techniques. In quadrature excitation, the input is split in two halves using a circuit that serves as a splitter/combiner device, that is 90° hybrid device, figure 4.5. The first part is fed into one point which is tangential to the x-axis and the other part of the signal is phase shifted by 90^0 and fed to a point that is $\pi/2$ away from the first point, tangential to the y-axis. If the rotating field has the same rotation of magnetization, the net magnetization vector will flip and rotate on the transverse plane [13].
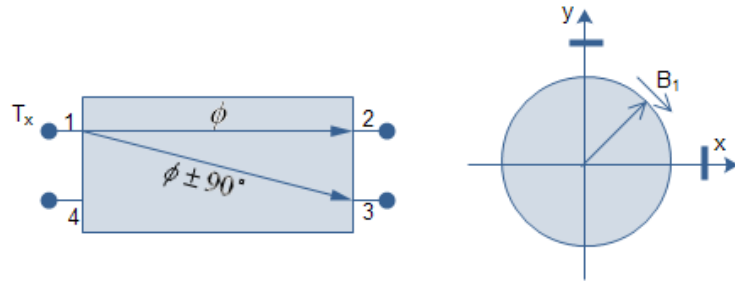
Figure 4.5: *Drivig the port in quadrature mode by 90^0 hybrid device.*

For the limited 2D model presented here where the birdcage coil has not been modeled as a complete electric circuit with passive components, the quadrature excitation is achieved by driving the voltage sources sinusoidally with 1 volt each, phase shifted by $\Delta\phi = m(2\pi)/16$, where m is the number of rungs. Hence, the total phase shift around the rungs is 2π. However, the linear excitation in the probe is done by driving the voltage sources with their magnitude

varying sinusoidally while the phase is kept constant. As the following

$$V_m = V_0 \sin\left(\frac{2\pi m}{16}\right), \tag{4.31}$$

where V_m denotes the voltage in the mth rung, and V_0 is the maximum voltage which is set to a unit volt for a low impedance port.

4.8.4 Results and Discussion: Transmit B_1^+ Fields Vs. Frequency

Figure 4.6 shows transverse rotational magnetic fields $|B_1^+|$ at 64, 128, 171 and 256 MHz in the birdcage-like coil when driven in linear and circular modes. For the linear birdcage-like coil, transmit fields were scaled to generate a maximum field value of $27\mu T$ for a 90° nutation in the brain. Accordingly, the transmit circular polarized field in the quadrature birdcage-like field has a peak value in the brain of $19.1\mu T$. Both coils show a uniform field distribution in the head at 64 MHz. As frequency increases, field intensity increases in the centre of the head as seen at 128 and 171 MHz. At 256 MHz, the field intensity becomes very high, forming the classic central brightening pattern surrounded by a trough in the $|B_1^+|$ response.

Considering brain tissue ($\varepsilon_r = 88$), the wavelength in such tissues at 64 MHz is about 50 cm greater than the head size. Hence, the phase of the wave is almost constant as it propagates toward the centre of the head. However, as the frequency increases to 256 MHz the wavelength in tissues decrease to 12.5 cm which is a significant fraction of the head size; hence, the wave phase changes significantly as it propagates toward the centre of the head which gives rise to the hotspot pattern. Figure 4.7 shows field profiles of linear and quadrature transmit fields $|B_1^+|$ across the brain. As frequency increases, the field intensity increases and field localise to a defined peak in the brain.
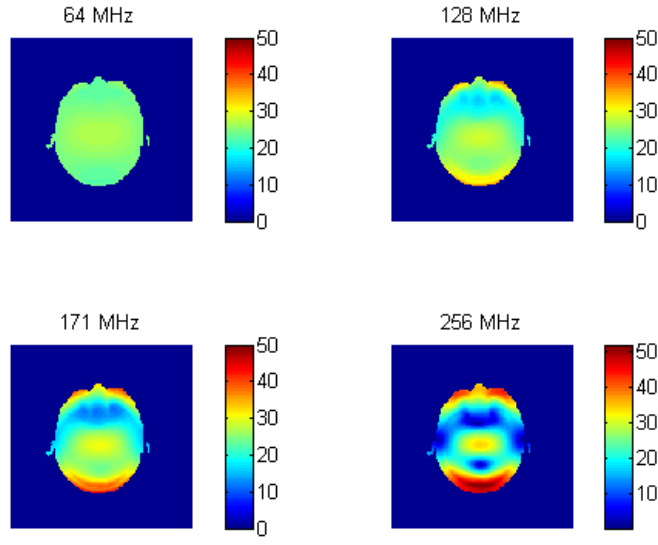
(a) Linear Excitation
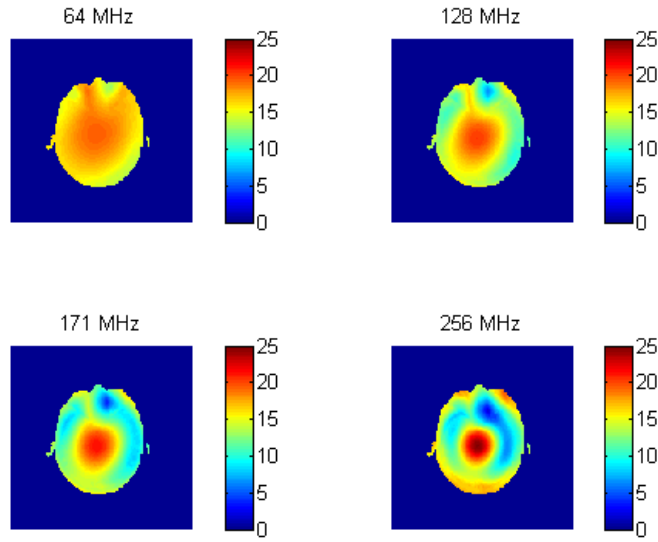
(b) Quadrature Excitation

Figure 4.6: *Transverse magnetic field maps $|B_1^+|$ in μT in (a) linear and (b) quadrature mode for all four frequencies.*
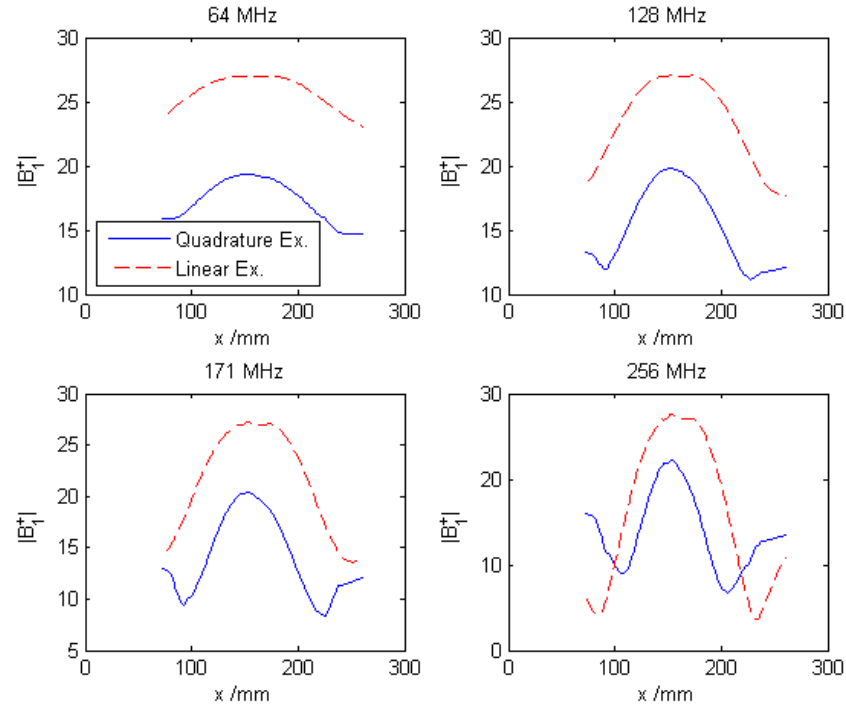
Figure 4.7: *Transmit B_1 profile of quadrature (red line) and linear (blue line) excitations.*

4.8.5 Results and Discussion: SAR calculations and Field Uniformity

In order to examine the SAR in the head and to verify this work against previous work done by Jin et al.[10], the head is assumed to be exposed to an RF pulse of 4.7 s duration and averaged over 6 min. SAR calculations were done based on equation (4.28) and tissue data in table 4.1. Figure 4.8(a) shows the SAR distribution in the 2-dimensional linear birdcage-like coil designed in this work in comparison to Jin et al. 2-dimensional linear birdcage coil, figure 4.8(b). Both coils show a weak SAR distribution in a horizontal strip shape across the head and increase linearly in the vertical direction to reach its highest value around the edge especially in the eyes and skin while remain constant along the horizontal direction. As the frequency increases towards 256 MHz, SAR values start to become higher in deeper regions of the head.

Figure 4.9 compares the SAR distribution in the birdcage-like coil and the birdcage coil designed by Jin et al. [10] with both coils in quadrature mode. The images in figure 4.9(a) and 4.9(b) show weak SAR distribution in the centre of the head which increases radially toward the edge while the values remains constant in the angular direction. As the frequency increases the weak region of SAR decreases because high SAR areas are deeper in the head. The difference in values between the two works is a result of using two different simulation techniques, transmission line modelling (TLM) and finite element method (FEM), for modelling the same coil.
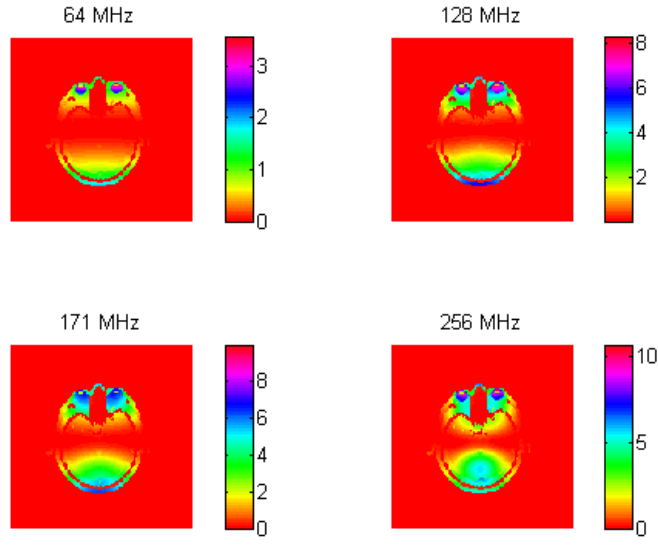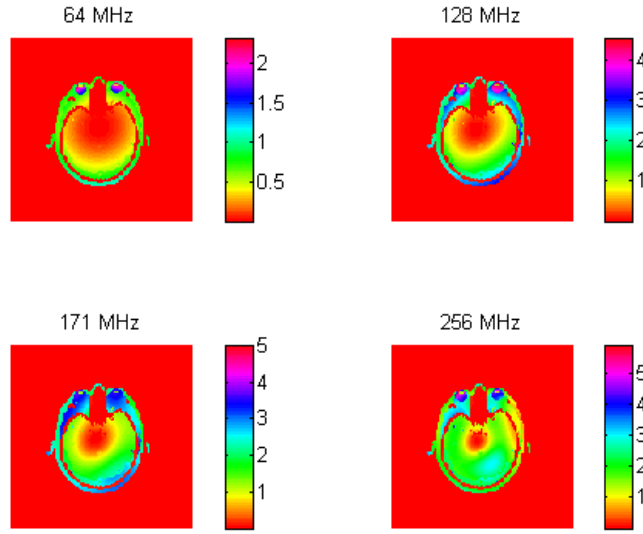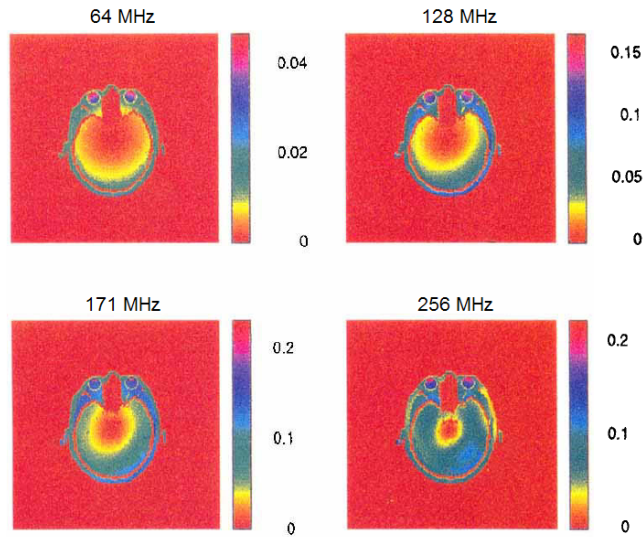
(a) Linear Excitation - this work
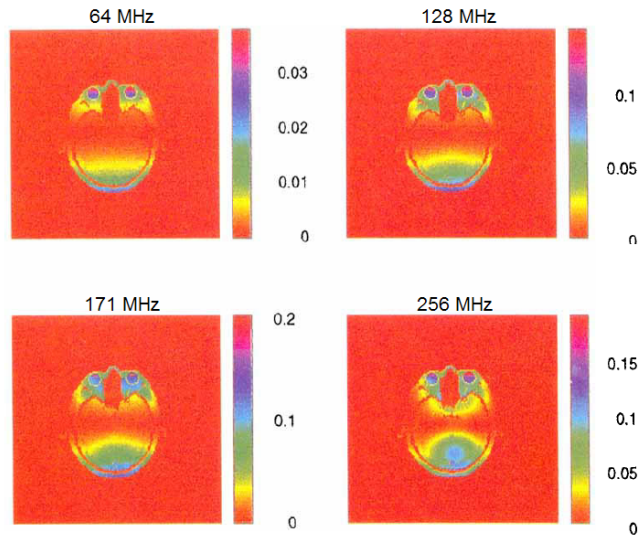
(b) Linear Excitation - Jin et al.

Figure 4.8: *SAR maps in W/kg as a result of linear excitation in (a) birdcage-like coil and, (b) Jin et al. birdcage coil for all four frequencies.*

(a) Quadrature Excitation - birdcage-like coil

(b) Quadrature Excitation - Jin et al. birdcage coil

Figure 4.9: *SAR maps in W/kg as a result of quadrature excitation in the (a) birdcage-like coil and (b) Jin et al. birdcage coil for all four frequencies.*

Table 4.2 gives average and maximum SAR values for all eight different tissues in the head slice at all four frequencies as a result of the linear excitation as well as SAR values over the entire region. As frequency increases the highest maximum SAR occur in humor and muscles, and SAR is increased from 64 MHz to 256 MHz by a factor of 3 for humor and by a factor of 5 for muscles tissues. Moreover, the average SAR values for the entire region have increased by a factor of 3.4, 4.3 and 4.8 when the frequency is increased from 64 MHz to 128, 171, and 256 MHz, respectively, and the maximum SAR values are 2.31, 2.81, and 2.9 for frequencies 128, 171 and 256 MHz.

Tissue Type	64 MHz		128 MHz		171 MHz		256 MHz	
	Avg.	Max.	Avg.	Max.	Avg.	Max.	Avg.	Max.
Lens	0.74	0.77	1.91	1.97	2.27	2.32	2.5	2.61
Humor	2.78	3.55	6.76	7.97	6.28	6.97	8.03	10.63
Cartilage	0.05	0.08	0.17	0.24	0.21	0.28	0.25	0.45
Bone	0.02	0.06	0.06	0.19	0.08	0.21	0.11	0.29
Brain	0.21	1.08	0.81	3.58	1.18	4.49	1.76	5.61
Skin	0.73	1.9	2.21	5.71	2.48	6.34	1.91	6.3
CSF	0.68	1.38	2.23	4.4	2.87	5.5	3.16	6.46
Muscle	0.54	2.01	2.47	8.22	3.42	9.98	2.97	10.46
Sclera	1.29	1.68	5.05	6.09	6.09	6.91	6.06	8.27
Overall	0.41	3.55	1.4	8.22	1.77	9.98	1.97	10.63

Table 4.2: *Maximum and average SAR (W/kg) for linear birdcage-like coil.*

For a quadrature birdcage-like coil, Table 4.3, the highest maximum SAR values occur in humor tissues where SAR values increased by a factor of 2.5 when frequency increased from 64 to 256 MHz. Moreover, as the frequency increased from 64 MHz to 128, 171, and 256 MHz the average SAR values

increase by a factor of 3.1, 3.7, and 4. Also, the maximum SAR values increase by 1.9, 2.1, and 2.5.

Tissue Type	64 MHz		128 MHz		171 MHz		256 MHz	
	Avg.	Max.	Avg.	Max.	Avg.	Max.	Avg.	Max.
Lens	0.48	0.51	1.09	1.13	1.2	1.25	1.29	1.46
Humor	1.87	2.33	3.97	4.53	3.42	3.78	4.32	5.93
Cartilage	0.03	0.04	0.08	0.12	0.1	0.13	0.12	0.2
Bone	0.02	0.03	0.05	0.1	0.06	0.11	0.07	0.13
Brain	0.23	0.64	0.8	1.87	1.14	2.33	1.69	3.01
Skin	0.81	1.13	2.18	3.03	2.36	3.08	1.73	3.42
CSF	0.54	0.83	1.56	2.39	1.94	2.85	2.11	3.01
Muscle	0.64	1.23	2.44	4.53	2.94	5.02	2.44	4.58
Sclera	0.87	1.1	2.97	3.44	3.33	3.74	3.26	4.54
Overall	0.4	2.33	1.24	4.53	1.49	5.02	1.63	5.93

Table 4.3: *Maximum and average SAR (W/kg) for quadrature birdcage-like coil.*

The maximum and average transmit field $|B_1^+|$ variation in the region of interest can be considered as a measure of field uniformity. The average field variation is calculated as

$$\delta_{avg} = \frac{1}{A\tilde{B}_1^+} \iint_A |B_1^+ - \tilde{B}_1^+| dA \qquad (4.32)$$

and the maximum B_1^+ field variation is given as

$$\delta_{max} = \frac{|B_{1max}^+ - B_{1min}^+|}{A\tilde{B}_1^+}, \qquad (4.33)$$

where A is the area of the region of interest and $\tilde{B}_1^+$ denotes the average value of B_1^+ over area A. Table 4.4 and 4.5 show average and maximum field inhomogeneity as a result of linear and quadrature excitation in brain tissues, respectively. In general, field inhomogeneity increases with frequency for both coils' excitation methods. The central brightening is evident for circular excitation where field variations are more obvious over brain tissues than for the linear coil. In the three lower frequencies, field distribution in tissues is more even for linear excitation; hence, field inhomogeneity is decreased by a factor of 2.4 for 64 MHz, 2 for 128 MHz, and 1.1 for 171 MHz in comparison to circular field excitation. However, at 256 MHz, the maximum and average field inhomogeneity is higher for linear excitation by 69% and 4.38%, respectively. This work is concerned with high RF frequencies, in particular 298 MHz, and hence the circular excitation method will be used in the forthcoming calculations.

	64 MHz	128 MHz	171 MHz	256 MHz
δ_{max}	17.54	60.18	107.04	241.1
δ_{avg}	6.48	14.54	22.17	72.38

Table 4.4: *Maximum and average field inhomogeneity (%) in brain tissues for linear birdcage-like coil.*

	64 MHz	128 MHz	171 MHz	256 MHz
δ_{max}	42.86	107.37	114.07	172.10
δ_{avg}	10.39	26.41	38.57	67.99

Table 4.5: *Maximum and average field inhomogeneity (%) in brain tissues for circular birdcage-like coil.*

4.9   Summary

In this chapter an in-house TLM code is adapted for investigating the head/coil interaction. A 2-dimensional birdcage-like coil was designed in both linear and quadrature mode at four different frequencies. The rotational field maps show the development of the central brightening effect as the frequency increases in agreement with previous work [12]. The in-house TLM code was verified by comparing SAR distribution in a 2-dimensional birdcage coil built by Jin et al. [10] to the birdcage-like coil modelled in this work in linear and quadrature excitation modes. Both studies show an agreement in SAR distribution across the head slice. It shows also that SAR values for linear excitation are higher than that for quadrature excitation due to the reduction of current values in quadrature mode. However, the difference in values between the two works is a result of using different simulation techniques, transmission line modelling (TLM) and finite element method (FEM), for modelling the same coil. The field inhomogeneity calculations show that field inhomogeneity increases as frequency increases. However, this is more evident in linear excitation at 256 MHz than in quadrature excitation.

Bibliography

[1] J. Chen, Z. Fen, and J. Jin. Numerical simulation of sar and b_1-field inhomogeneity of shielded rf coils loaded with the human head. *Mag. Reson. Med.*, 45(5):690–695, 1998.

[2] C. Christopulous. *The Transmission-Line Modelling (TLM) Method in Electromagnetics.* Morgan and Claypool Publishers, 2006.

[3] C. M. Collins, S. Li, and M. B. Smith. Spatial resolution of numerical models of man and calculated specific absorption rate using the fdtd method: A study at 64 mhz in a magnetic resonance imaging coil. *Journal of Magnetic Resonance Imaging*, 40:847–856, 1998.

[4] C. M. Collins, W. Liu, J Wang, R. Gruetter, T Vaughan, K. Ugurbil, and M. B. Smith. Temperature and sar calculations for a human head within volume and surface coils at 64 and 300 mhz. *Journal of Magnetic Resonance Imaging*, 19:650–656, 2004.

[5] C. M. Collins and M. B. Smith. Calculations of b_1 distribution, snr and sar for a surface coil adjacent to an anatomically-accurate human body model. *Mag. Reson. Med.*, 45:692–699, 2001.

[6] C. M. Collins and M. B. Smith. Spatial resolution of numerical models of man and calculated specific absorption rate using the fdtd method: A study at 64 mhz in a magnetic resonance imaging coil. *J. Magn. Reson. Imag.*, 18:383–388, 2003.

[7] P. J. Dimbylow and S. M. Mann. Sar calculation in anatomically realistic model of the head for mobile communication transceivers at 900mhz and 1.8ghz. *Phys. Med. Biol.*, 39:361–368, 1994.

[8] O. P. Gandhi and J. Y. Chen. Numerical dosimetry at power-line frequencies using anatomically based models. *Bioelectromagnetics*, 1:43–60, 1992.

[9] O. P. Gandhi, G. Lazzi, and C. M. Furse. Electromagnetic absorption in the human head and neck for telephone at 835 and 1900 mhz. *IEEE Transactions on Microwave Theory and Techniques*, 44:1884–1897, 1996.

[10] J. Jin and J. Chen. On the sar and field inhomogeneity of birdcage coils loaded with human head. *Mag. Reson. Med.*, 38:953–963, 1997.

[11] J. M. Jin, J. Chen, W. C. Chew, H. Gan, R. L. Magin, and P. J. Dimbylow. Computation of electromagnetic fields for high-frequency. *J. Magn. Reson. Imag.*, 40:847–856, 1998.

[12] Arthur W. Magill. *Ultra-High Frequency Magnetic Resonance Imaging.* PhD thesis, School of physics and Astronomy, University of Nottingham, 2006.

[13] J. Mispelter, M. Lupu, and A. Bringuet. *NMR probheads for biophysical and biomedical experiments: theoretical principles and practical guidelines.* Imperial College Press, 2006.

[14] J. Paul, C. Christopoulos, and D. Thomas. *A 3-D time-domain TLM electromagnetic field solver: regSolve.cc.* The George Green Institute for Electromagnetics Research (GGIEMR), School of Electrical and Electronic Engineering, University of Nottingham, 2000. In house manual.

[15] Matthew N. O. Sadiku. *Numerical Techniques in Electromagnetics.* CRC Press, 2001.

[16] J. Wang, O. Fujiwara, Sachiko Kodera, and Socichi Watanabe. Fdtd calculation of whole-body average sar in adult and child models for frequen-

cies from 30 mhz to 3 ghz. *Physics in Medicine and Biology*, 51:4119–4127, 2006.

Chapter 5

B_1 shimming: Optimizing of Elementary Drive Currents for Volume Coils Using the Regularisation Technique

5.1 Introduction

Over the past few decades computer modelling and simulation techniques have become increasingly important in many different fields especially for the bio-engineering and Medical fields. No matter the size of the physical problem to be investigated the goals are basically the same; to understand the system characteristic in order to represent its behaviour and then to seek a useful solution that can represent and predict the unknown response. For that, mathematical modelling as a tool of investigation accompanied with computational modelling, have become both substantial and successful in predicting and optimizing many biological and physical systems. For example, one approach to overcome the in-homogeneity issues at ultra high fields is through controlling

the excitation elements independently. These elements can be driven appropriately to improve the excitation profile through independent pulse profiles for parallel excitation [8]. Ibrahim et al [7] compared the performance of birdcage coil with linear, quadrature and four port excitation and concluded that for higher field systems using four port excitation is superior in terms of homogeneity and SAR values over that of 2 port quadrature excitation. B_1 shimming can be also used to improve homogeneity over a region of interest(ROI) through altering element's phases and/or amplitudes independently. Mao et al [10] studied B_1 shimming at frequencies up to 600 MHz using the xFDTD method using 16 and 80 element elliptical, stripline coil arrays; the results showed that B_1 shimming could be more effective with a large number of drive elements or small ROI. A 16 element driven coil can shim a slice up to 600 MHz while 80 element shimming can shim the whole brain at frequencies up to 600 MHz. The field homogeneity in relation to SAR values was explored by Mao et al [11] using 16 stripline TEM elements shimming over three different regions: optimizing the whole head, entire brain and, a single brain slice. It was concluded that when the B_1 homogeneity improved over a small region of interest, the maximum local SAR level might become high if the SAR is not taken into consideration during optimisation. Therefore, the numerical approach is vital in describing the behaviour of this system and with the right optimization tool one can suggest new solutions and optimal drive configurations.

This chapter describes the using of the regularization technique in MRI. First the inverse problems and the discrete ill-posed problems is described. The transmission line modelling (TLM) technique is then used to demonstrate the tissue-RF field interactions in two birdcage-like coils, 6 and 16 rungs, at 300 MHz in two and three dimensional problem as well as two three dimensional 32 and 64 multi-element coils for further comparison. The necessary mathematical information for use of the regularization technique used is introduced.

The details of the mathematical theories for optimisation is out of the scope of this work.

5.2   Inverse Problem

The term inverse problem is widely mentioned in different application fields especially engineering and physics. According to J. B. Keller [6] one can call two problems inverse to each other if the formulation of one problem involves the other. One is called the direct problem and the other is the inversion problem. However, when the mathematical representation is for a real physical problem, direct and inverse problem are distinct in nature. For example, the direct problem could be the prediction of the future state of the system from the knowledge of its present state and physical laws, while the inverse problem might be the determination of the present sate of the physical system from future observation or identification of its parameters. From the point of view of applied mathematics, there are two main reasons for studying inverse problems: the need to know the past state or parameter of a physical system, as well as the need to know how to control a physical system via its parameter or present state in order to reach a desired state in the future. Inverse problems do not often satisfy the conditions of the well-posed problem. They could have a solution but the solution might not be unique or might not depend continuously on the data. They also might not have a solution, so they can be classified as ill-posed problems [6].

5.2.1   Discrete Ill-Posed Problem

The conditions of well-posed problems was first introduced by Hadamard in 1923, his postulates for a well-posed problem are that:

- For the permissible data, a solution exists;

- For the permissible data, the solution is unique;

- The solution depends continuously on the data [6].

He also supposed that physical systems could not be solved because they are usually ill-posed problems in which at least one of the conditions "the existence, uniqueness or continuity" are violated [5]. However, a vast number of ill-posed problems in science, engineering and medicine was dealt with and described in literature. One example is the problem that will be discussed later in this work. Although there might be some concerns about the violation of the first condition, the second and the third ones are the most important. If the problem has more than one solution then one has to decide which one to dismiss and which to pick by adjusting the model through adding further information [6]. Serious numerical problems can arise from the violation of the third condition, if any small perturbation in the data causes a large perturbation in the solution [6]. In other words, if the solution does not depend continuously on the data. Illustrating the difficulties associated with ill-posed problem is done by the means of a linear system of equations:

$$Ax = b; \quad A \in R^{n \times n}. \tag{5.1}$$

The linear least squares problem can be defined as,

$$min \parallel Ax - b \parallel_2, \quad A \in R^{m \times n}, \quad m \geq n. \tag{5.2}$$

The problem is ill-posed, if it satisfies the following:

- The singular value of A decays to zero;

- The ratio between the largest and the non-zero singular value is large [5].

Therefore, the above equations can not be solved with the standard methods of numerical linear algebra, such as LU factorization or Cholesky method,

because the criteria indicate that A is ill-conditioned; "have a large condition number" [5]. In such a case where the ordinary numerical methods do not hold for such data as they are no longer stable, one can seek a more well behaved solution by the means of Regularization Methods. Regularization methods do not make an inherently unstable methods stable, all that they do is make the solution as stable as possible by recovering a part of the information about the solution [6].

5.2.2 The Regularization Technique

In general, regularization methods used to overcome the difficulties are associated with a large condition number A. This is usually achieved by replacing the ill-conditoined matrix A by a well-conditioned one that is drawn from A in order to get an approximate solution [3]. It is also necessary to add additional information about the sought solution that control the smoothness of the solution [5], where the smoothness degree is controlled by the so called regularization parameter λ. This is represented by adding a small norm or seminorm $\|L\left(x - x^*\right)\|$ to the described ill-posed problems $Ax = b$ or $min\|Ax - b\|$. The rationale behind this assumption is that the solution to physical problems must have a small seminorm or norm; side constraint:

$$\Omega\left(x\right) = \|x - x^*\| \tag{5.3}$$

where x^* is the initial estimate solution.

It is necessary to seek a regularized solution x_λ so that there is a balance between minimizing the residual norm $\|Ax-b\|$ and the side constraint $\Omega\left(x\right)$. one of the most common regularization method is called *Tikhonov regularization*, where the regularized solution is given by:,

$$x_\lambda = argmin\{\|Ax - b\|^2 - \lambda^2\|L\left(x - x^*\right)\|^2\}. \tag{5.4}$$

The variation in the regularization parameter λ reflects the sensitivity of the regularized solution to the perturbation in A and b. There are many different methods of regularization beside the Tikhonov regularization [5]. However, the Tikhonov regularisation is a standard method to use.

5.2.3   The Singular Value Decomposition (SVD)

It has been mentioned before that one of the associated problems with ill-posed systems is the ill-coditioning of matrix A. The singular value decomposition (SVD) is an important tool in regularization techniques that deal with these problems through decomposing the ill-conditioned matrix into a well-conditioned one.

The singular value decomposition decomposes a matrix $A \in R^{m \times n}$ with $m \geq n$ into the following form,

$$A = U\Sigma V^T = \sum_{i=1}^{n} u_i \sigma_i v_i^T \,. \tag{5.5}$$

Where $U^T U = V^T V = I_n$. U and V are called the left singular vector and the right singular vector; respectively, and they are orthogonal matrix. Σ is a diagonal matrix with none-zero elements in a decreasing order,

$$\Sigma = diag(\sigma_1, \sigma_2, \sigma_3, ...) \quad such\,that \quad \sigma_1 \geq \sigma_2 \geq \sigma_3 \geq .... \tag{5.6}$$

These diagonal elements are called the singular values of A and they are the square roots of the eigenvalues of AA^T or A^TA. By calculating the eigenvector of A^TA one can get the columns of V while the columns of U are the eigenvectors of AA^T.

5.2.4 Calculating the Optimal Regularization Parameters: the L-curve Method

The L-curve method is one of the graphical tools used for analysing ill-posed problems. It is a log-log plot, for all valid regularization parameters, of the seminorm $\|L(x_{reg})\|_2$ and the residual norm $\|Ax_{reg} - b\|_2$. Its name implies that it has the latter L shape with a distinct corner. The importance of the L-curve method arises from it being a trade off curve between the two quantities seminorm $\|L(x_{reg})\|_2$ and residual norm $\|Ab - x\|_2$ that ought to be controlled [5, 4].

If the regularization parameter is too large, the regularization solution corresponds to terms where $\|Ab - x\|_2$ will not fit the data correctly because too much filtering (damping) have been done on the data. In other words, the regularized solution correspond to terms where the regularization error dominates. If the regularization is too small then this means that the regularization solution corresponds to terms where $\|L(x_{reg})\|_2$ is too large despite the fact that the fit is good. This means that the terms are dominated by the perturbation errors. In other words, the solution x_{reg} corresponds to terms where less filtering is imposed [5, 4].

5.2.5 Tikhonov Regularization

Tikhonov regularization is considered to be an inverse problem as the regularized solution defined by equation (5.4) is a solution to the least-squares problem

$$min\| \begin{pmatrix} A \\ \lambda L \end{pmatrix} x - \begin{pmatrix} b \\ \lambda L x^* \end{pmatrix} \|_2 . \tag{5.7}$$

The regularisation routine used in this work is adopted from Hansen Regularisation package [5].

5.3 Regularization Approach in RF Coil Design

Consider an RF coil with discrete current elements, the resultant transverse B_1 field due to these sources within the coil structure can be represented as

$$AI = B \quad , \quad B \in C^m \quad , \quad I \in C^n \quad , \quad A \in C^{m \times n}. \qquad (5.8)$$

where A is the sensitivity matrix, where each element $A(i,j)$ represents the complex field components $B_{x,y}$ at the voxel i from the source j, B is the target field components over the region of interest and I is the current source [9]. As the number of current elements is usually smaller than the number of the sampling points in A, the system under the study is an overdetermined system and it is classified as ill-posed. The system can be solved by the means of the regularization methods and can be thought of as a minimization of,

$$min \left\{ \|AI - B\|_2^2 + \lambda \|I - I_0\|_2^2 E \right\} . \qquad (5.9)$$

where E is the identity matrix, I_0 is the initial estimation of the currents (usually equal to zero) and λ is the optimal regularization parameter. The regularization parameter is determined by the L-curve method for a given target field. The regularization method used in this work is the well known Tikhonov regularization combined with the SVD method. The problem consists of searching for the optimal current values I that produces a homogeneous rotating field B_1^+ by calculating the optimal regularization parameter for different target fields.

In this work four different target fields are proposed in order to search for the best fields homogeneity. These are given in table 5.1. The first target field (TG1) represents a uniform field distribution with a uniform phase changes imposed, in the second target field (TG2) the phase changes are removed, in the third target field (TG3) the field distribution takes a quadratic shape over

the brain slice while the fourth target was chosen so that target field TG3 is smoothed. All target maps were scaled to a maximum of one. Figure 5.1 shows a representation of the third and fourth target fields.

Target Field	B_x	B_y
TG1	1	1i
TG2	1	0
TG3	$B_x(x,y) = (x^2 + y^2)pi/2$	$B_y(x,y) = i*(x^2 + y^2)pi/2$
TG4	$B_x(x,y) = \exp(x^2 + y^2)pi/2$	$B_y(x,y) = \exp i*(x^2 + y^2)pi/2$

Table 5.1: *The four different target fields proposed for the regularization scheme*

(a)   (b)
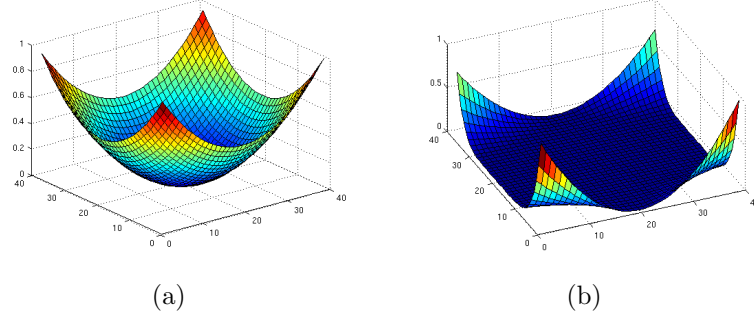
Figure 5.1: *Target Field:(a)target field (TG3) and,(b) target field (TG4).*

5.4 Results and discussion

5.4.1 2-dimensional TLM Birdcage-Like Coil Simulation and Optimization for B_1 Shimming

Two 2D shielded birdcage-like coils are simulated as an axial slice of a 3D birdcage coil. Unlike a true birdcage coil, the elements are driven as separate resonators at 300 MHz in the manner of a multi-transmit system. In this way the homogeneity can be optimized. The mesh size is of $70 \times 70 \times 1$ dimension with spatial resolution of 6 mm. The elements are at 14.4 cm radius surrounded by a screen of 16.8 cm inner radius and 1.8 cm thickness. The probe consists of either 8 or 16 elements simulated as current sources, figure 5.2. The shield has the advantage of reducing the simulation time as well as the benefits of preventing the probe (rf coil) coupling with the other circuits in the true physical MRI system. The upper and lower boundaries are modelled as parallel planes to acquire the transverse magnetic field components H_x, H_y as well as the electric field component E_z, and hence the coil with be simulated as an infinitely long coil.

(a) 8-element coil   (b) 16-element coil
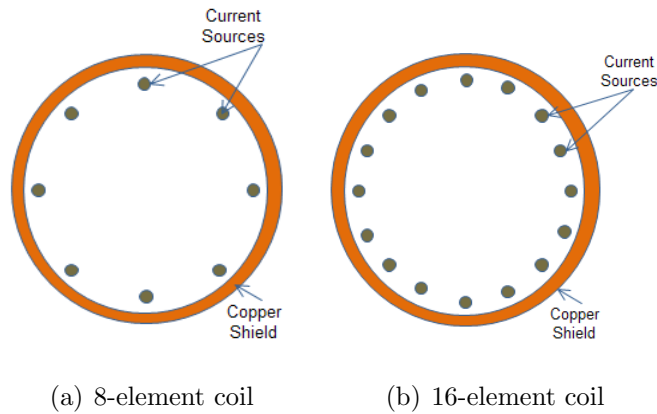
Figure 5.2: *Shows the 2-dimensional birdcage-like coil: 5.2(a) 8 element birdcage-like coil, 5.2(b) 16 element birdcage-like coil.*

Four different slices were extracted from the well known 3D head model (HUGO model) and used in the simulation, figure 5.3. The first slice passes through the sinus and includes fat, muscle, bone, marrow, blood, CSF, cartilage, mucous membrane, ganglia and neuron (Cerebelum) tissues. The second slice is 3.6 cm distance from the first and passes thorough the eyes and includes grey matter, white matter, muscous membrane, neuron (Cerebelum), muscles and CSF. the third slice passes through the brain's grey and white matter and is 5.4 cm away from the second and, the fourth slices is 1.2 cm away and also passes through the brain's grey and white matter. The choice of these slices is to study the effect of variation in tissue types in different slices on B_1 fields. for example, slice 1 has a high variation in tissues, (Fat, Muscle, Bone, Marrow, Blood, CSF, Cartilage, Ganglia, Neuron (Cerebelum)), while slice 3 has a low variation of tissue types, (Gery Matter, White Matter, Eyes (Vitreous), blood and CSF). The original head model is of 3 mm voxel size was re-sampled to a 6 mm head model in order to reduce the computational time. It consists of 15 different tissue types given in table 5.2. Each slice was uploaded in the 2D coil, then each source was individually excited sinusoidally at 300 MHz using current sources. The acquired electric and magnetic field maps were used to build up the sensitivity maps for Tikhonov regularization. The L-curve method is used to obtain the regularization parameter for the optimal solution, equation 5.9.
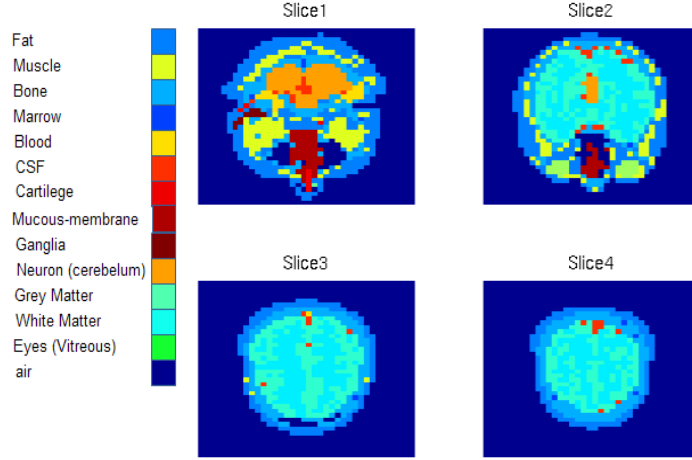
Figure 5.3: *Four 6mm axial slices: slice 1 passes through the sinus; slice 2 passes through the eyes; slice 3 and slice 4 passes through the brain.*

Material	σ S/m	ε_r	ρ Kg/m^3
air	0	1	0
marrow	0.02737	5.758	1810
fat	0.03957	5.634	920
bone	0.2156	23.16	1810
white matter	0.4133	43.78	1040
grey matter	0.6924	60.02	1040
skin	0.6414	49.82	1010
eye (viteous)	1.518	69.02	1170
muscle	0.7705	58.2	1040
blood	1.316	65.65	1060
neuron (cerebelum)	0.9732	59.72	1040
eye (lens)	0.6478	48.95	1100
csf	2.224	72.73	1010
cartilage	0.5525	46.77	1100
mucus-membrane	0.6308	51.9	1040
ganalia	0.8512	62.45	1040
copper	5.8e7	1	0

Table 5.2: *Electrical properties used for HUGO head tissue model and coil materials [2, 1]*

5.4.2 2-Dimensional 8 Rung Birdcage-Like Probe Vs. 16 Rung Birdcage-Like Probe at 300 MHz: Currents, Field Maps and Inhomogeneity

The L-curve method is used to calculate the optimal regularization parameter using all four target fields for all axial slices under study and all results were scaled to generate $|B_1^+|$ of 1.975 μT. Figure 5.4 shows currents and phases of 8 and 16 rungs RF coil for slice 1 in the two upper rows and the two lower rows, respectively. Using target field TG1, the 8-rung phases (upper row - red line) follow a similar linear behaviour to that of the standard 8-rung coil (blue line) with a reduced amplitude. The 16-rung coil shimming results follow the same behaviour of the 8-rung with more fluctuating in amplitude of the currents. Figure 5.5 shows that the 8 and 16 rungs coil fields' maps have a similar field distribution with higher field values in the brain area in the 16 rungs coil. unlike the standard 8 and 16 rungs coil, maximum $|B_1^+|$ fields distributed in soft tissues of the brain rather than around the sinus area and the skin. Removing the y-component in the second target TG2 alters the regularized phase behaviour, phases follow a sinusoidal behaviour in an increasing manner with amplitudes fluctuating around the head for the 8 rung coil while for the 16 rungs coil phases start to fluctuate randomly in an overall linear fashion with currents amplitude behave as a decaying sinusoidal wave. Figure 5.5 shows that using the second target field has focused the fields in brain area while using TG3 and TG4 has removed the $|B_1^+|$ fields from the head and the high values were shifted toward the skull and skin tissues. The currents' amplitudes, figure 5.4, as a result of using the third and fourth target fields (TG3, TG4) follow a sinusoidal behaviour in the 8 rungs coil while the phases from the third TG fluctuate in a linear fashion and that of the fourth TG flow a sinusoidal function behaviour.
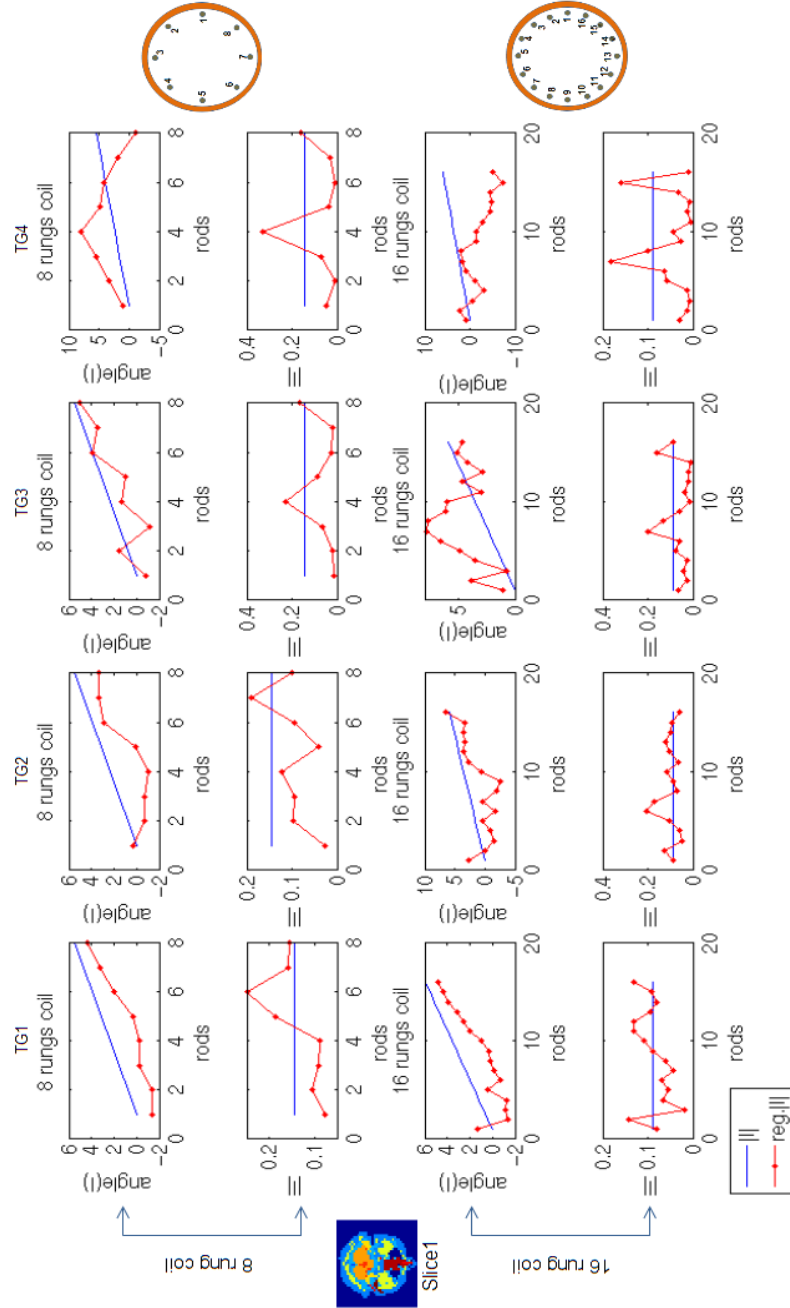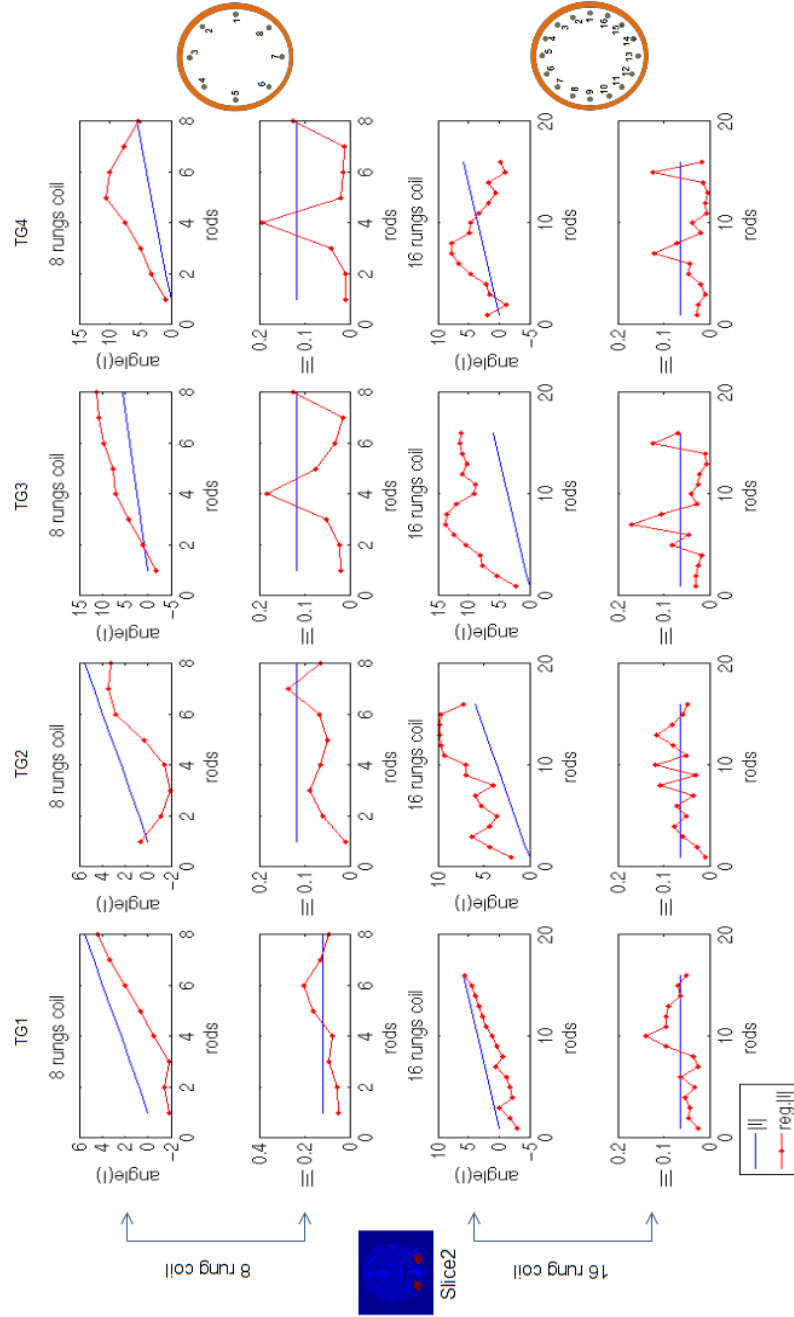
Figure 5.4: *Currents and phases of the 8-rung coil, top two rows, and; of the 16-rung coil, bottom two rows, for the first slice using target fields (TG1, TG2, TG3 and,TG4) from left to right. The blue line represents the results of a standard coil and the red line represents the optimisation technique results (RF shimming).*
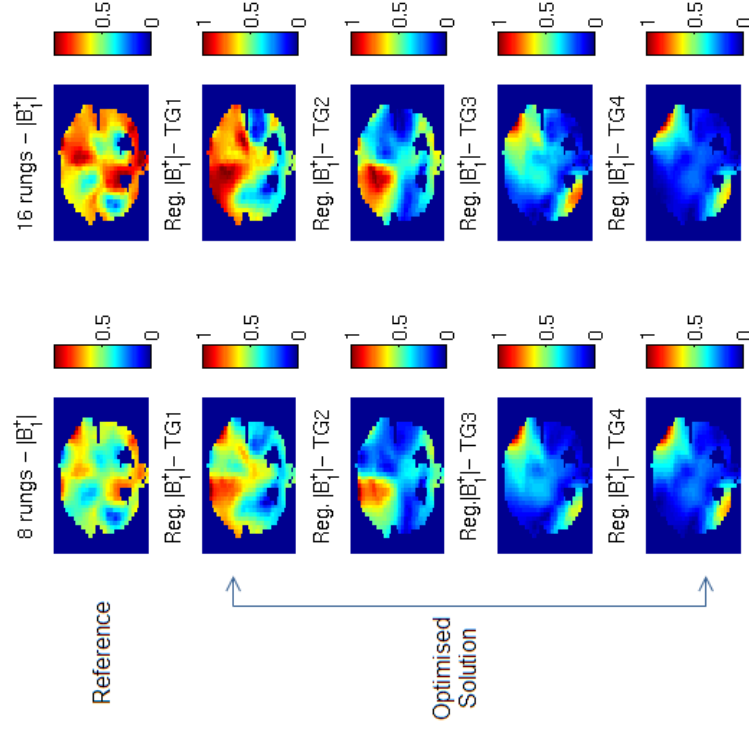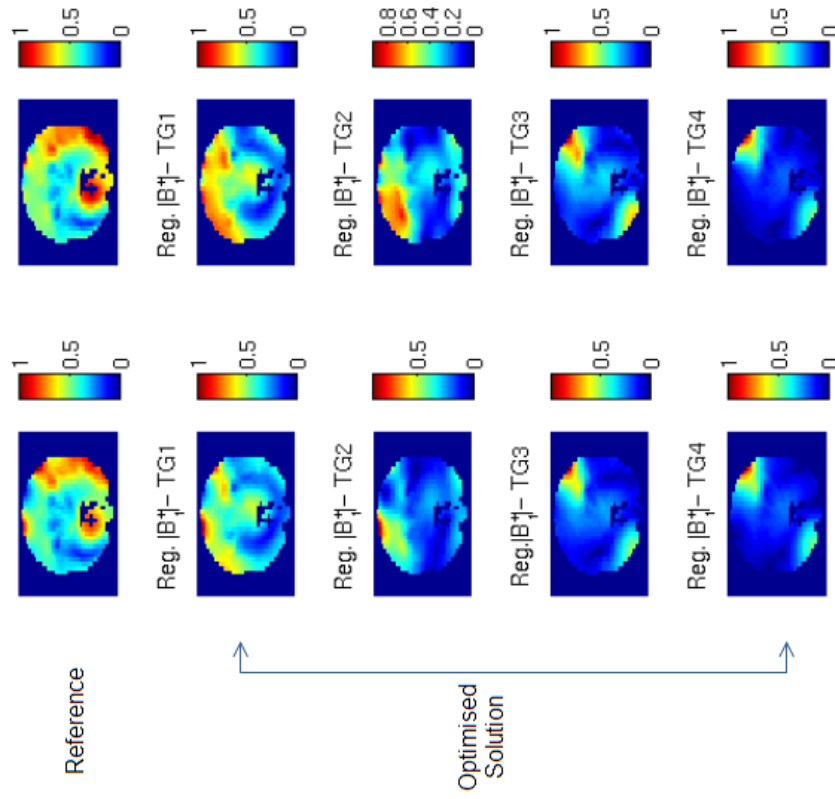
Figure 5.5: *The field maps for the first slice: using 8-rung (left column) and 16-rung (right column) coils. The figure compare the results of a standard birdcage coil field maps (Top row) with optimised field maps using four target fields (RF shimming), (TG1) in the second row, (TG2) in the third row, (TG3) in the fourth row, (TG4) in the fifth row.*

Figure 5.6 and figure 5.7 are the phases and currents distribution using all target fields and their corresponding field maps for 8 and 16 rungs coil for the second slice, all results are compared with standard birdcage coils results. In general, the current phases and amplitude follow the same behaviour to that of the first slice. The first target field TG1 gives the most uniform field distribution and linear phase variation for both the 8 and 16 rungs coil; the second target field (TG2) gave a linearly increasing sinusoidal phase behaviour; third and fourth target fields (TG3, TG4) currents' phases are of higher values than that of (TG1, TG2) with phases resultant from TG4 vary sinusoidally. Currents' amplitudes fluctuate randomly; however, those resultant from using (TG1 , TG2) and (TG3, TG4) flow the same behaviour, respectively.

The third and fourth slices have similar behaviour in $|B_1^+|$ field distribution, see figure ((5.9) and (5.11)) and also similar regularized currents' phases and amplitudes, as shown in figure ((5.8) and (5.10)). Figure 5.9 and figure 5.11 show that the hot spot appeared using standard 8 and 16 rung birdcage-like coil have been redistributed using regularized currents and phases (shimming) with the first target field TG1. However, using shimming with the second target field TG2 reduces the area over which the $|B_1^+|$ fields are distributed which in turn reflect back on fields uniformity. Using $|B_1^+|$ shimming with TG3 and TG4 eliminate almost all the $|B_1^+|$ fields in the brain and will not serve the goal of achieving a uniform transmit field distribution in the brain and therefore, will not be used in this work.

Figure 5.6: *Currents and phases of the 8-rung coil, top two rows, and; of the 16-rung coil, bottom two rows, for the second slice using target fields (TG1, TG2, TG3 and,TG4) from left to right. The blue line represents the results of a standard coil and the red line represents the optimisation technique results (RF shimming).*
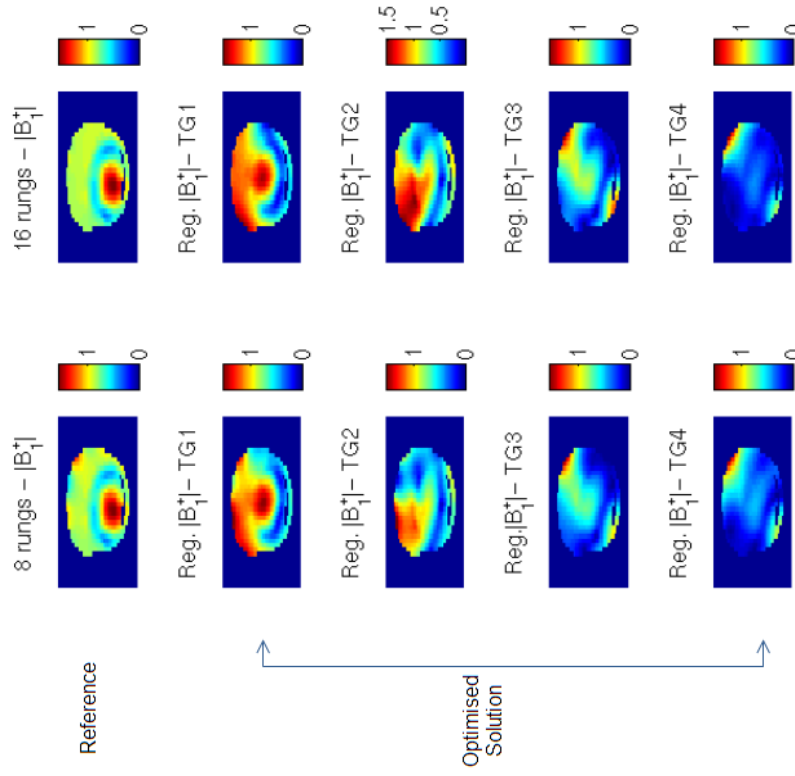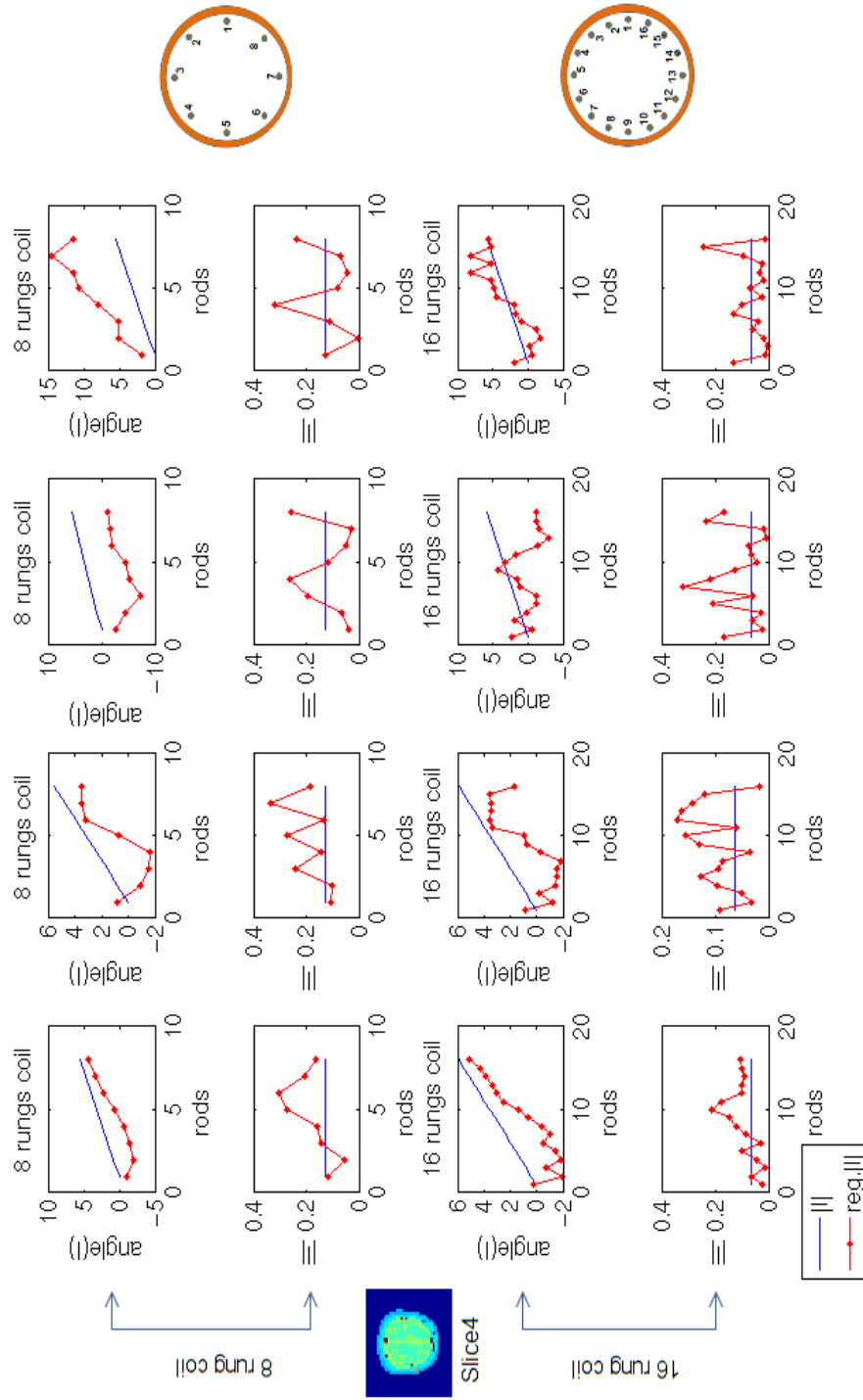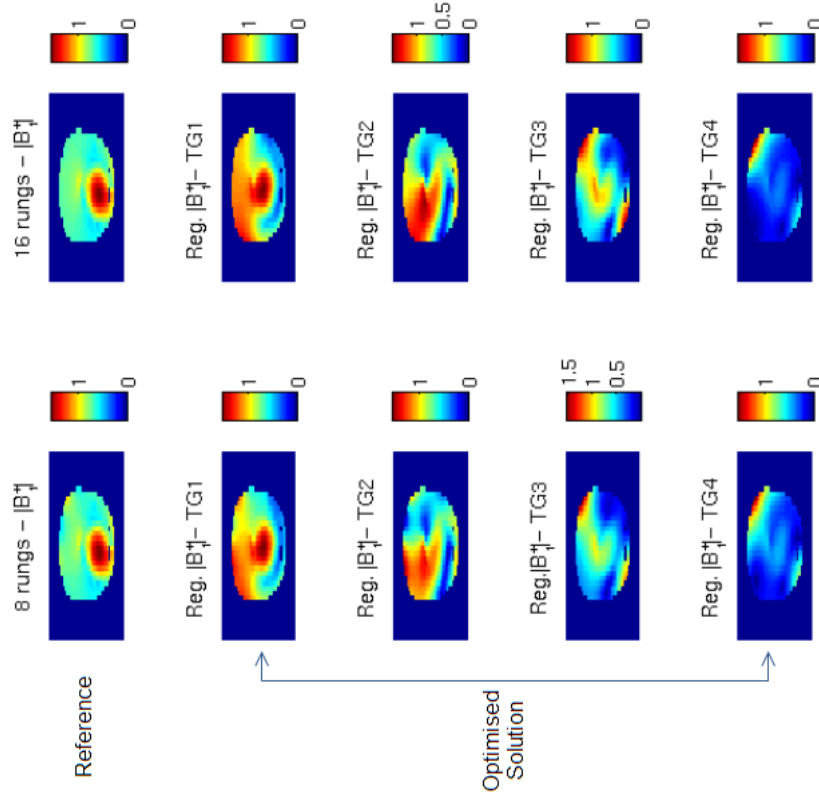
Figure 5.7: *The field maps for the second slice: 8-rung (left column) and 16-rung (right column) coils. The figure compare the results of a standard birdcage coil field maps (Top row) with optimised field maps using four target fields (RF shimming), (TG1) in the second row, (TG2) in the third row, (TG3) in the fourth row, (TG4) in the fifth row.*
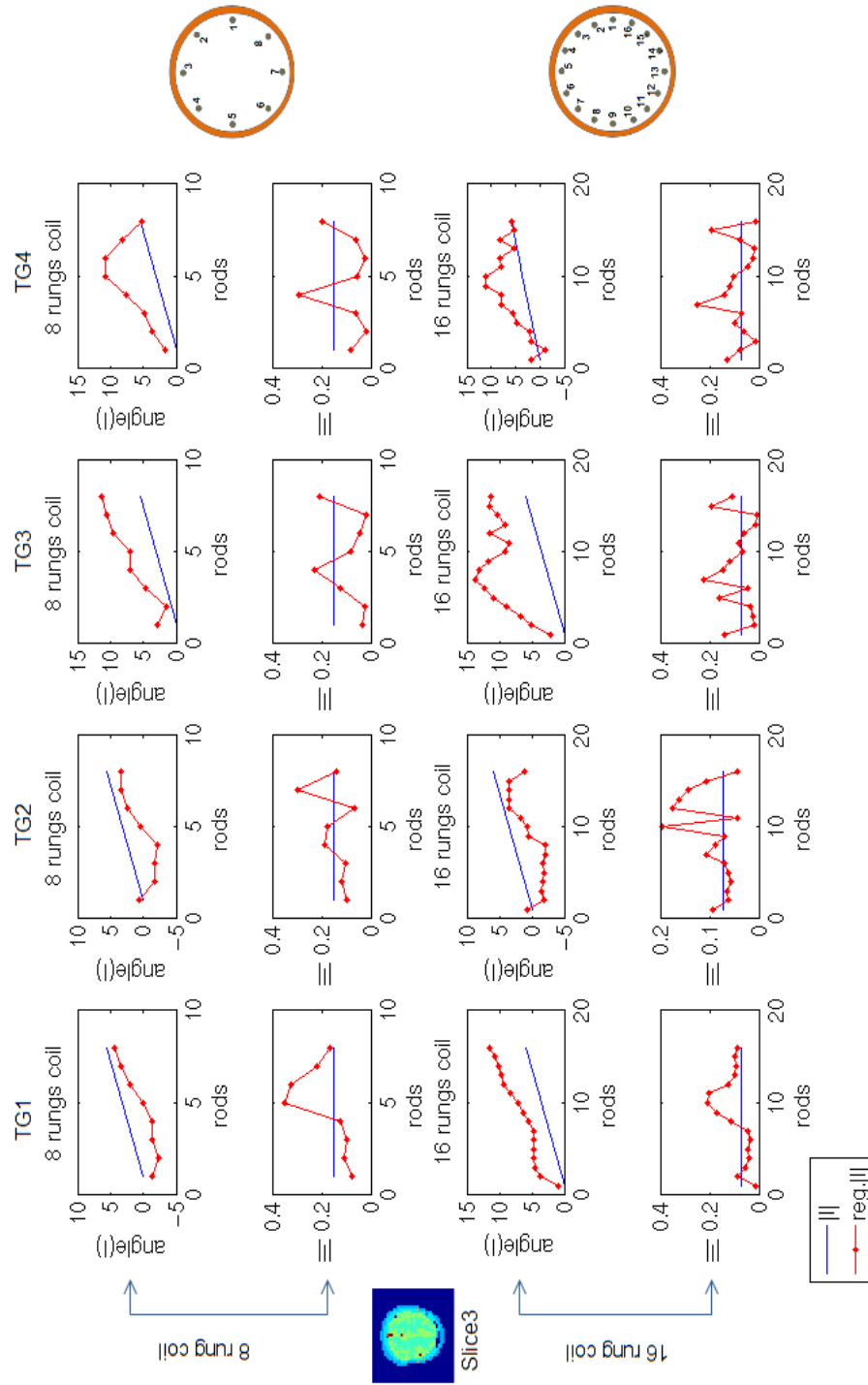
Figure 5.8: *Currents and phases of the 8-rung coil, top two rows, and; of the 16-rung coil, bottom two rows, for the third slice using target fields (TG1, TG2, TG3 and,TG4) from left to right. The blue line represents the results of a standard coil and the red line represents the optimisation technique results (RF shimming).*

Figure 5.9: *The field maps for the third slice: using 8-rung (left column) and 16-rung (right column) coils. The figure compare the results of a standard birdcage coil field maps (Top row) with optimised field maps using four target fields (RF shimming), (TG1) in the second row, (TG2) in the third row, (TG3) in the fourth row, (TG4) in the fifth row.*

Figure 5.10: *Currents and phases of the 8-rung coil, top two rows, and; of the 16-rung coil ,bottom two rows, for the fourth slice using target fields (TG1, TG2, TG3 and,TG4) from left to right. The blue line represents the results of a standard coil and the red line represents the optimisation technique results (RF shimming).*

Figure 5.11: *The field maps of the fourth slice: using 8-rung (left column) and 16-rung (right column) coils. The figure compare the results of a standard birdcage coil field maps (Top row) with optimised field maps using four target fields (RF shimming), (TG1) in the second row, (TG2) in the third row, (TG3) in the fourth row, (TG4) in the fifth row.*

Table 5.3 and 5.4 shows the calculated field in-homogeneity using equation 4.32 for all different slices with all target fields for 8 and 16 rung coils, respectively. In comparison to field in-homogeneity for standard birdcage-like coils a more uniform field is results from using the first target field in the regularization method for all four slices. In the 8-rung shimming, uniformity improved by 4.6% in the first slice and, 8.54% for the second slice and, 8.82% for the third slice and, 11.91% for the fourth slice. Shimming the 16-rung coil using the first target field increase uniformity by 2.62% for the first slice and, 6.68% for the second slice and, 6.86% for the third slice and, 9.82% for the fourth slice.

	TG1	TG2	TG3	TG4	Standard Probe
slice1	71.21	88.26	88.88	95.73	75.81
slice2	73.97	92.24	88.08	96.44	82.51
slice3	71.78	84.06	85.58	94.62	80.6
slice4	53.92	72.79	71.74	88.94	65.83

Table 5.3: *The regularized and non-regularized field inhomogeneity (%) for all four slices using 8-rung birdcage-like coil*

	TG1	TG2	TG3	TG4	Standard Probe
slice1	72.14	86.91	88.81	96.16	74.76
slice2	75.95	90.52	88.32	97.49	82.63
slice3	73.65	82.43	85.1	96.5	80.51
slice4	55.42	70.9	72.23	90.04	65.74

Table 5.4: *The regularized and non-regularized field inhomogeneity (%) for all four slices using 16-rung birdcage-like coil*

5.5   3-dimentional TLM Volume coil Simulation and Optimization for B_1 Shimming

In this section the 2D TLM simulation and optimisation is extended to a 3D coil for a full representation of the physical head/coil system. Four different coils have been simulated in this work: 8 rung birdcage-like coil (BC), 16 rung birdcage-like coil (BC), 32 multi-element coil and 64 multi-element coil. Each element in all coils were driven independently to generate the sensitivity maps for the Tikhanov regularization routine. The regularization were done for four different slices and for a Region of interest (ROI) in the brain . Currents' phases and amplitudes, $|B_1^+|$ field maps, uniformity and SAR values were compared for all coil designs.

5.5.1   TLM Volume Coils Simulation

The 3D 8 and 16 rungs birdcage-like coils are modelled as a cylindrical copper shield surrounding the coil elements. Elements are connected to the shield with upper and lower end-rings. The position of rods in the TLM mesh were determined by considering them distributed evenly along the circumference of a cylinder with radius R as

$$\phi = \frac{2\pi(n-1)}{N};$$
$$x = R\cos(\phi);$$
$$y = R\sin(\phi);$$

where n is the rod number, n: 1-8 for $N = 8$ rungs coil or, n:1-16 for $N = 16$ rungs coil. The copper shield is a 24 cm long copper cylinder with 16.8 cm radius and 1.8 cm thickness. The extreme ends of the shield is connected to upper and lower end rings with 6 mm length, 14.4 cm radius and, 2.4 cm thickness to be attached the copper shield. The rods were position at a surface

of 14.4 cm radius cylinder so that they will be attached to the copper shield through the end-rings. They are 6 mm cubic rods of 24 cm long; each rod is driven by 300 MHz sinusoidal current source positioned at the middle of the rod. figure 5.12 shows a schematic representation of the coils.
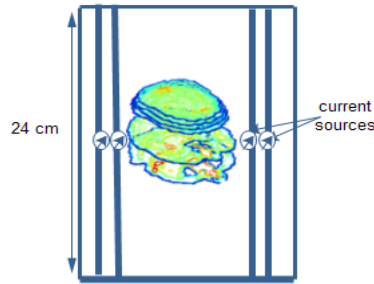
Figure 5.12: *Representation of the 8 and 16 rungs birdcage-like coil with the head slices used in this work are shown only.*

The 32 and 64 multi-elements coils were designed by adjusting the 8 and 16 birdcage coils through dividing each rod into four separate rods where each edge is connected to the copper shield with upper and lower end-rings; figure 5.12 shows a schematic representation of the multi-element coil. The rods at the extremes are 9 cm long where the middle two rods are of 8 cm long. The four rods with the eight end-rings give a total length of 24 cm. Each rod is driven with a 300 MHz sinusoidal current source positioned at the middle. The TLM mesh size was of $70 \times 70 \times 70$ cubic voxels with spatial resolution of 6 mm. The coils are loaded with HUGO head model slices described in section **??**. First, the TLM code was run for each rod individually and the electric and magnetic field were recorded in time for six different slices in total. slice 1 is passing through the sinus, slice 2 is 3.6 cm distance from slice 1, slice 3 is 5.4 cm away from slice 2 and finally slice 3, slice 4, slice 5 and slice 6 are 0.6 cm apart from each other. Second, the sensitivity maps for each slice were built using fields values from all individual rungs excitation and used in the

Tikhonov regularization routine with the first target field TG1 tested in the 2D simulations. TG1 was used as a target field because it gave the lowest inhomogeneity figures for all slices tested in the 2D simulation. The run time is about 14 hours for each current source.
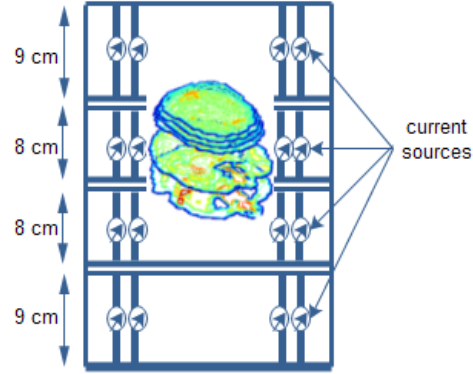
Figure 5.13: *Representation for the 32 and 64 multi-elements coil with the head slices used in this work are shown only.*
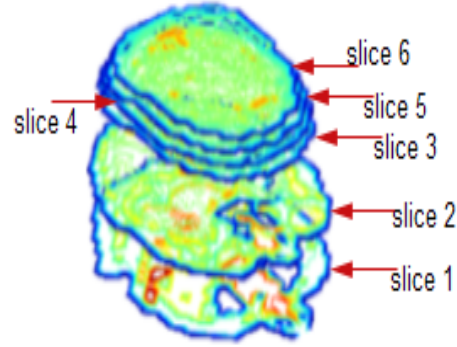
Figure 5.14: *The four chosen slices for individual slice optimisation and RF shimming.*

The 3D coil modelling and optimization results were divided into two parts. The first part is for the optimisation of $|B_1^+|$ maps and currents using four selective slices (individual slice optimisation). These are slice 1, slice 2, slice 3 and slice 5. The field maps, currents' phases and amplitudes and field uniformity for all four coils then compared to standard birdcage coil results .

The second part of the work was aimed at investigating the possibility of optimising the RF shimming for both optimal field uniformity and SAR value reduction for a region of interest. In order to do that four neighbouring slices were selected from the brain with a 1810 6 mm voxels in total , these are slice 3 to slice 6 in figure 5.14. In this case, the sensitivity maps is the summation of the acquired volume magnetic field maps and SAR maps for all individual sources excitation. The SAR maps were calculated using equation 4.28.

5.5.2   3D RF Head Coil Shimming for Four Different Axial Slices Using Tikhonov Optimisation

Figure 5.15 to figure 5.18 show the $|B_1^+|$ field maps before and after optimization in all slices for all four coils coils with their corresponding shimming (currents' phases and amplitude). All results were normalized to represent the 90 degree flip angle maps and currents values to generate a 3 ms duration rectangular RF pulse of 1.975 μT field strength in the brain's soft tissue. In figure 5.15, the non optimised $|B_1^+|$ fields for the 8 rung birdcage-like coil shows a central brightening in slice 1 and slice 2 where tissues diverge more than those of slice 3 and slice 5, using the optimisation routine did not improve the field pattern in slice 2 while the $|B_1^+|$ field is reduced to half at the middle of the slice, the $|B_1^+|$ fields pattern in slice 3 and 5 has a minor improvements in uniformity. The Regularisation optimisation routine assigned a linear phase change for current source for all slices while the currents' amplitudes differ with the slice. Similar to $|B_1^+|$ fields maps, the current amplitudes for slice 1 and 2 fluctuate randomly while for slice 3 and 5 they fluctuate in a linear fashion around the current amplitude. The 16 rungs birdcage-like coil, figure 5.16, shows similar behaviour to the 8 rungs coil. The non optimized $|B_1^+|$ field shows a central brightening in all slices but appears strongly in slice 1 and slice 2. Tikhanov regularization shows improvement in $|B_1^+|$ field distribution in slice 3,5 which pass through the brain. The magnitude of $|B_1^+|$ in slice 2 falls by 20 % while for slice 1 the regularization routine almost removed the $|B_1^+|$ field and therefore with such proposed current drive the 90 degree flip angle would not be achieved. Currents' phases and amplitudes for slice 3 and 5 are identical in their behaviour, linearly increasing fluctuating phases and a fluctuating amplitudes.
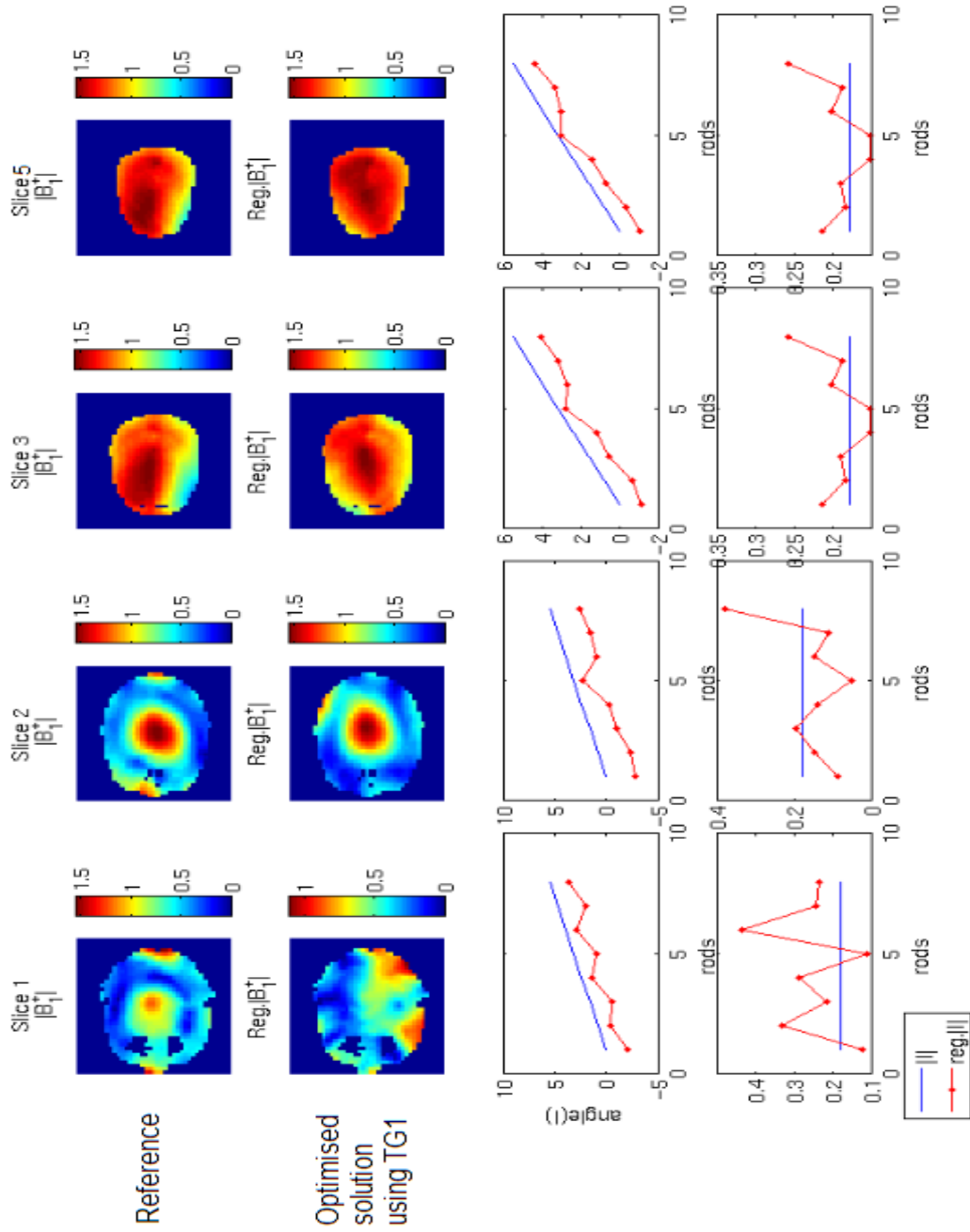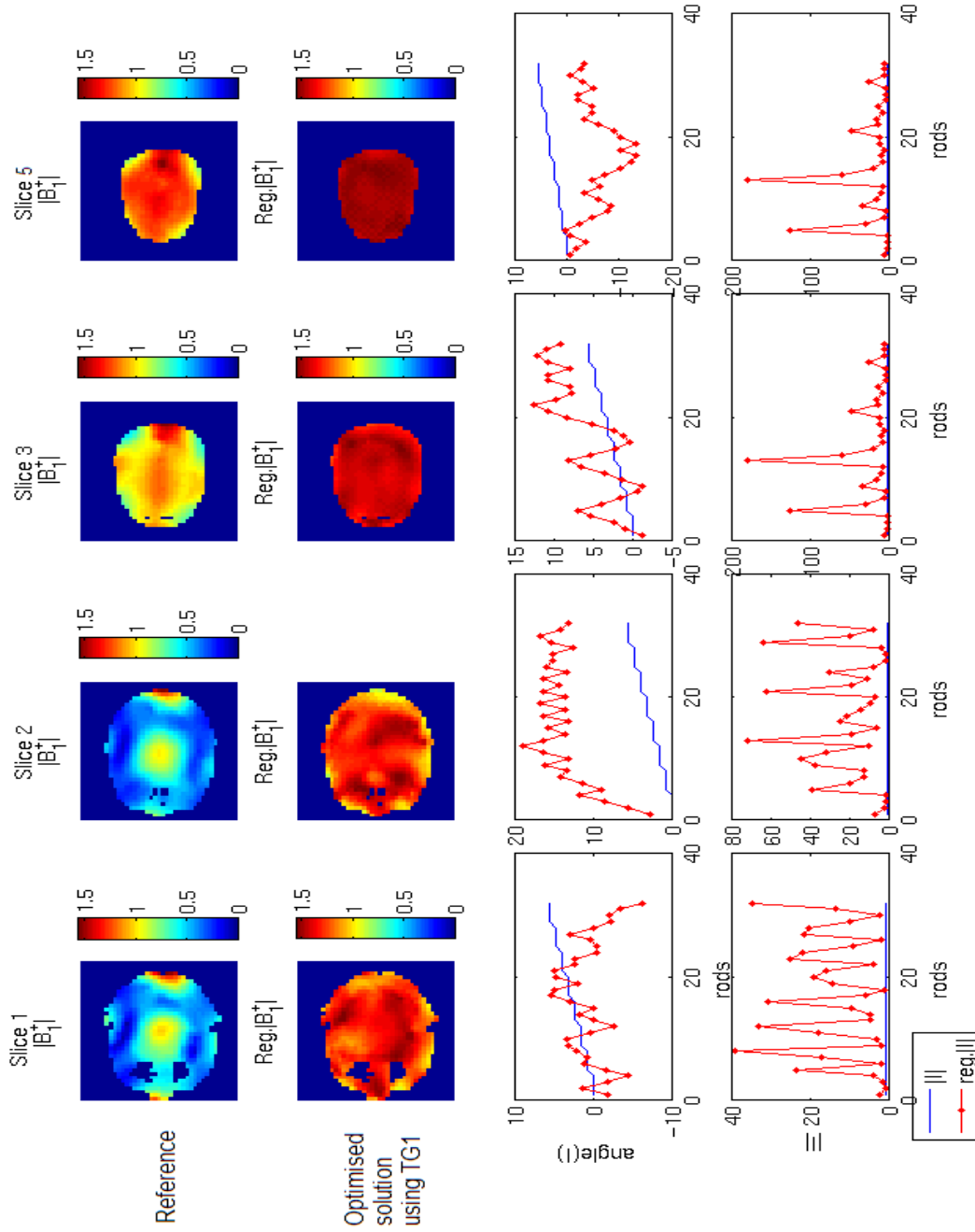
Figure 5.15: *Rotational field map (μT) and currents' phases (radian) and amplitude (Amp) for 8 rung coil for slices 1, 2,3 and 5.*
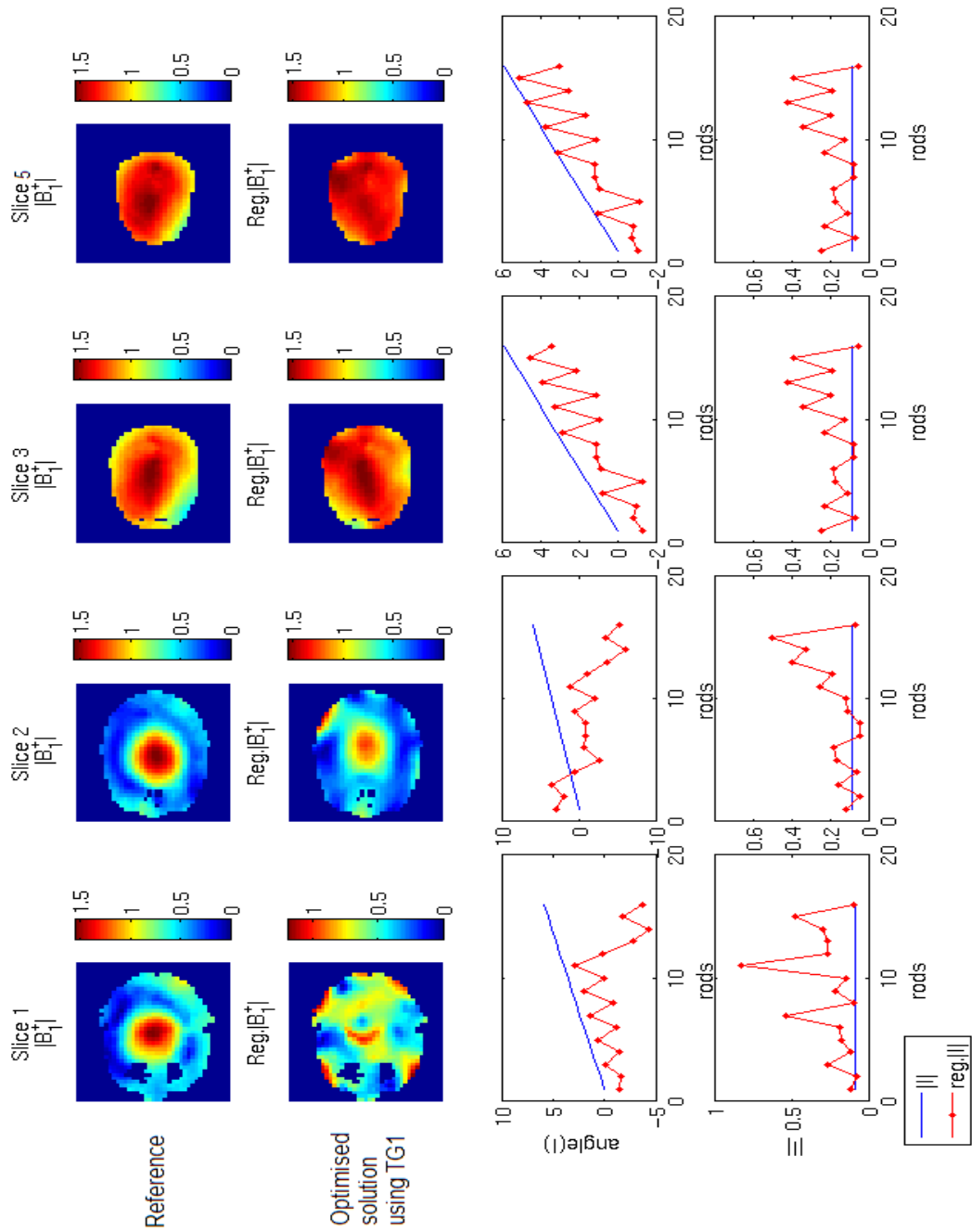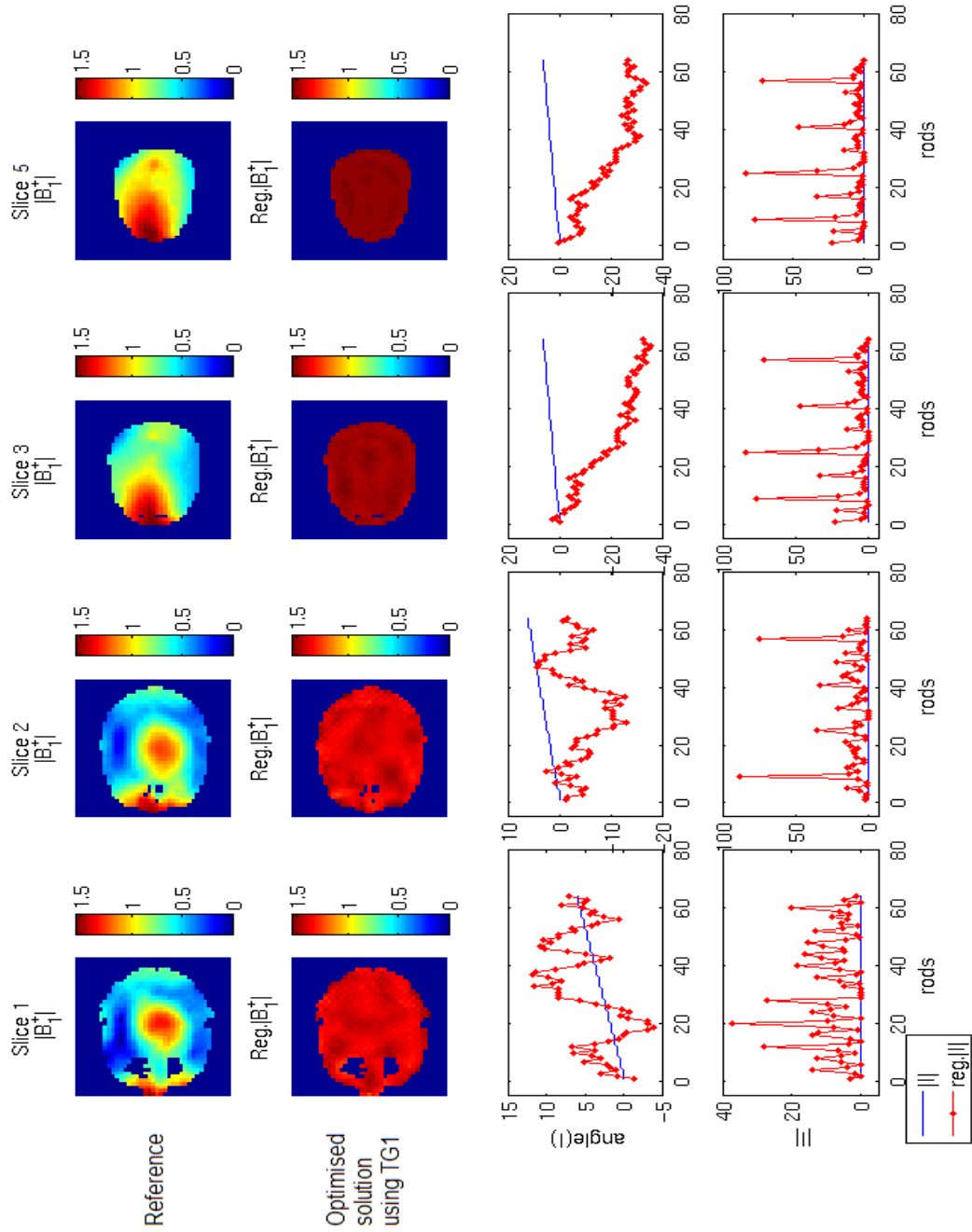
Figure 5.16: *Rotational field map (μT) and currents' phases (radian) and amplitude (Amp) for 16 rungs coil for slices 1, 2,3 and 5.*

Using the 32 and 64 multi-element coil, figure 5.17 and figure 5.18, increases the optimised $|B_1^+|$ field maps homogeneity for all slices especially for slice 1 and slice 2 in comparison to the same slices from 8 and 16 rung coils. The two figures show also that increasing the number of elements would produce more uniform flip angle maps over the whole excited slice. However, the assigned currents' phases and amplitude behaviour are not systematic and predictable for all slices. For both coils slices with no nulls introduced in them are more likely to have the same current amplitude values, such as slice 3 and slice 5. In general, there are some points where the amplitude spikes to a very high values for some elements, between 40 to 200 Amp for 32 multi-element coil and between 40 to 100 Amp for 64 multi-element coil. This implies that only a few elements have been optimised for shimming. In the 32 multi-element coils, current phases vary almost sinusoidally around the non regularized linear values for slice 1 and slice 3. The phases for slice 2 are about 4 times higher than the non optimised once, the values start with sharp increase for half the coil elements then plateau for the other half. Optimised current phases for slice 5, have a reverse direction to the none optimised and vary in a sine wave form. For 64 multi-element coil, the optimised phases for slice 1 and 2 vary sinusoidally for coils' elements while the phases for slice 3 and 5 follow a reverse trend to that of the non optimised one.

Figure 5.17: *Rotational field map (μT) and currents' phases (radian) and amplitude (Amp) for 32 multi-elements coil for slices 1, 2,3 and 5.*

Figure 5.18: *Rotational field map (μT) and currents' phases (radian) and amplitude (Amp) for 64 multi-elements coil for slices 1, 2,3 and 5.*

Table 5.5, shows field in-homogeneity for all four coils for all slices. In general, the homogeneity of the $|B_1^+|$ fields increases as the number of coils elements increase. In the 8 rungs birdcage-like coil, homogeneity of $|B_1^+|$ fields using Tikhanov optimisation increased by about 10, 3.75, 3.58 and 2.98 % in slice 1, 2, 3 and, 5, respectively. In the 16 rungs birdcage-like coil, homogeneity of slice 1, 2, 3, and 5 is increased by 40.24, 18.95, 2.19 and, 4.61 %, respectively. Using the 32 multi-elements coil reduces the field inhomogeneity by 74.96, 68.77, 34.56 and, 22.15 % while using 64 element-coil reduces inhomogeneity further by 82.02, 77.31, 40.71 and, 28.21 % for all four slices, respectively.

Slice	Slice 1		Slice2		Slice 3		Slice 5	
	UnReg.	Reg.	UnReg.	Reg.	UnReg.	Reg.	UnReg.	Reg.
8 rungs BC	91.9	81.79	86.34	82.77	41.51	37.93	27.74	24.76
16 rungs BC	97.32	57.08	92.00	73.05	38.08	35.89	25.59	20.98
32 multi-elements	87.48	12.52	81.8	13.03	38.76	4.2	24.5	2.35
64 multi-elements	86.21	4.19	81.03	3.72	42.18	1.47	28.95	0.74

Table 5.5: *Uniformity measures in (%) for all four coils (slice 1, slice 2, slice 3 and slice 5): the 8 and 16 rung birdcage-like coil, 32 and 64 multi-elements coils comparing the optimised field $|B_1^+|$ maps (Reg.) to the none optimised $|B_1^+|$ fields.*

5.5.3 3D RF Head Coil Shimming for an Assigned Volume Using Tikhonov Optimisation

Figure 5.19 shows optimal regularisation parameter values and L-curve plots for all four coils, it is well known that in the L-curve method the log-log plot has to show a distinct corner; however, for a large scale problem it is often hard to achieve. The L-curve solution does not show the correct L-shape for both 8 and 16 rung coils unlike the L-curve for optimising the 32 and 64 multi-element coils. The number of the current elements is very small in comparison to the size of the sensitivity matrix given in equation (5.8), 8×18252 for the 8 rung coil and 16×18252 for the 8 rung coil. This reflects back on all the optimised solution where solution is not converged for these two coils.
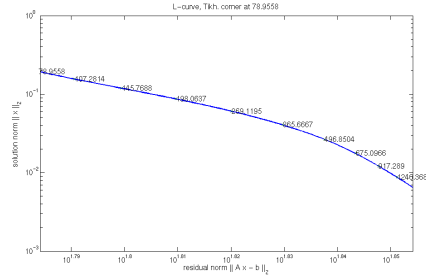
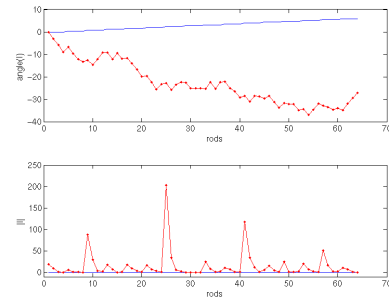
(a) 8 element BC-like coil
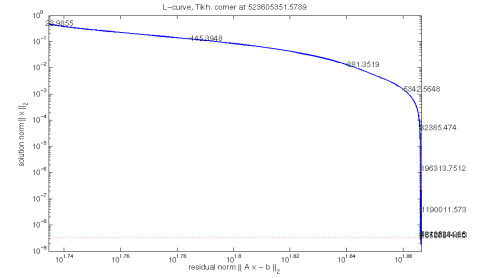
(b) 16 element BC-like coil
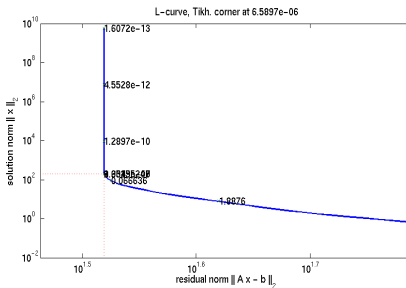
(c) 32 multi-transmit coil
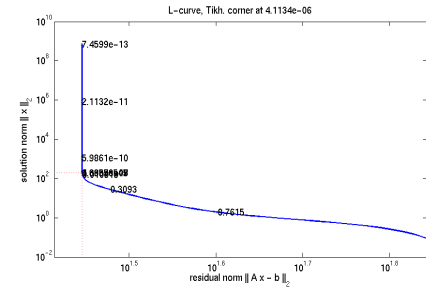
(d) 64 multi-transmit coil

Figure 5.19: *The l-curve values and plots for all four coils.*

In figure 5.20(a), the 8 rung coil current phases follow a sinusoidal behaviour as well as the amplitude while in the 16 rungs coil, figure 5.20(b), current

phases and amplitudes are almost linear except from two spikes in the current amplitude which indicate that only two sources of current were shimmed. Figure 5.21(a) shows that the optimised field values are less uniformly distributed than the non optimised $|B_1^+|$ field maps. However, SAR maps, figure 5.21(b), show a decrease in the optimised SAR values by a factor of 3.6 for first two slices, by a factor of 1.6 for the third and, by a factor of 2.6 for the last slice. However, it also has to be taken into consideration that the original electric field values produced by the TLM code are of high values which have a direct effect on optimised SAR values. In figure 5.22(a), the regularized $|B_1^+|$ fields are localised in frontal lobe area which cause field in-homogeneity. Moreover, the calculated SAR values, figure 5.22(b), are extremely high for the optimised solution in comparison to the no regularized value, the SAR values are higher by a factor of 10^7 which means that the optimised solution did not converge.
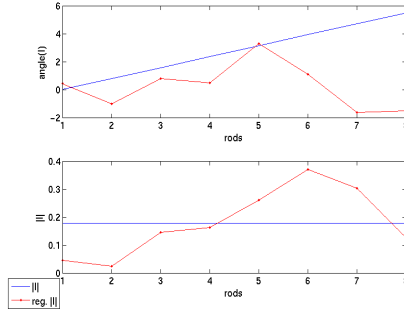
(a) 8 element BC-like coil
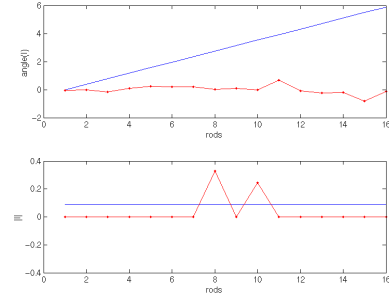
(b) 16 element BC-like coil
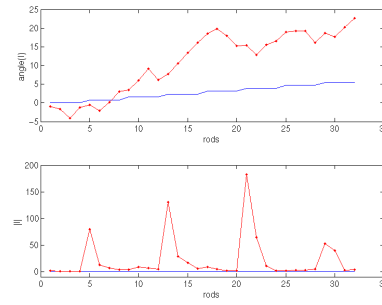
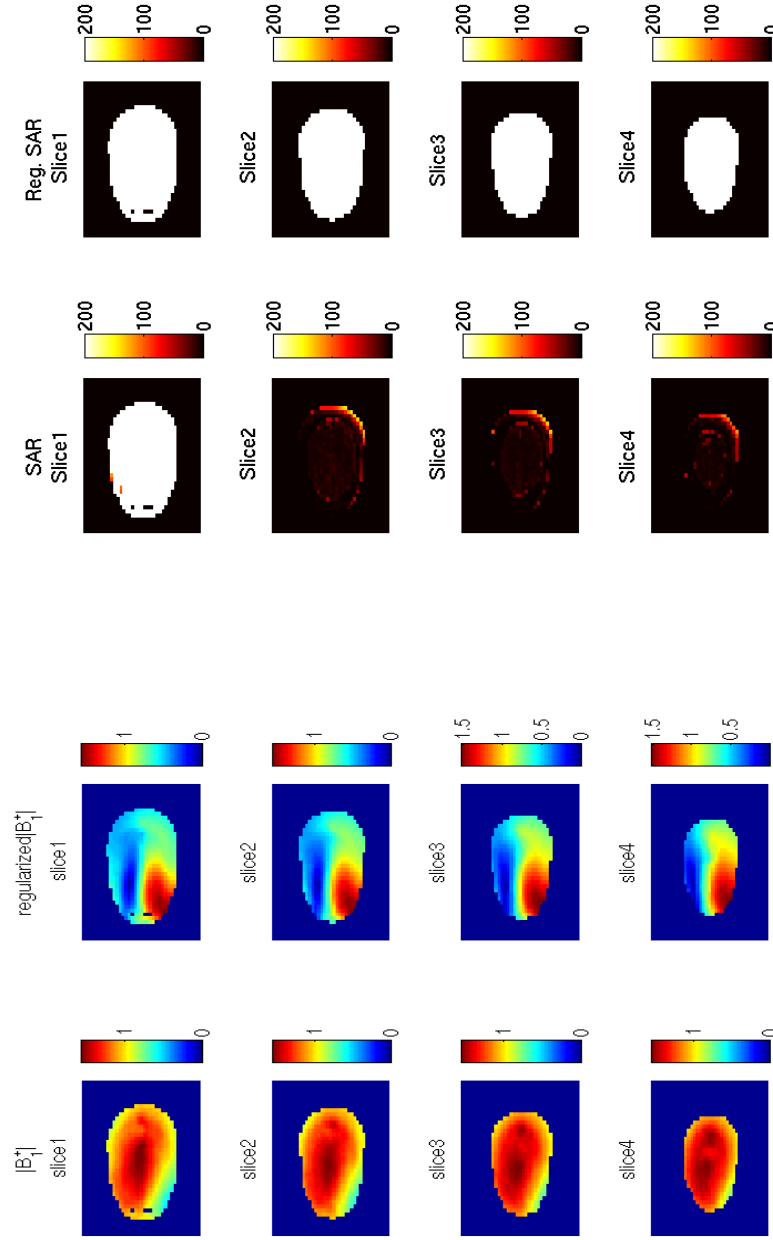(c) 32 multi-transmit coil

(d) 64 multi-transmit coil

Figure 5.20: *The Current phases (radian) and amplitude (Amp) for all four coils for a regularized volume.*
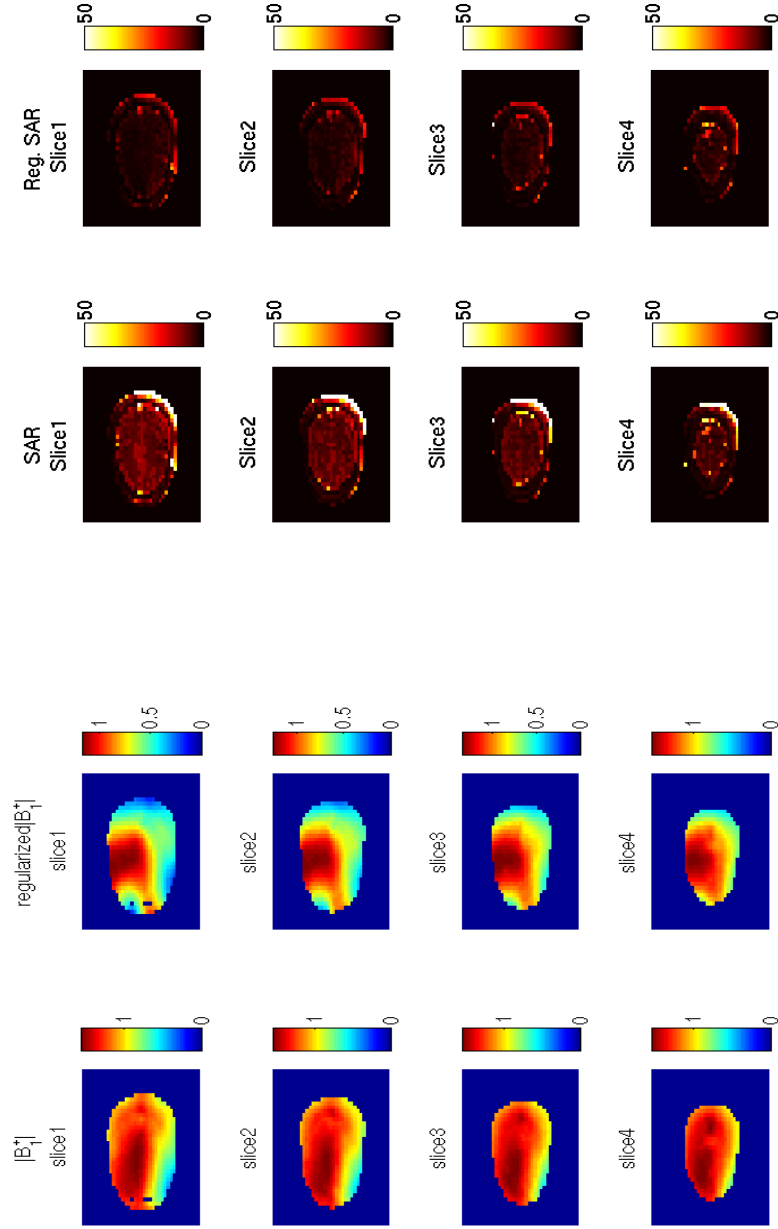
(a) 8 elements birdcage-like coil- $|B_1^+|$ maps

(b) 8 elements birdcage-like coil- SAR maps

Figure 5.21: $|B_1^+|$ field map (μT) and SAR ($watt/Kg$) for all four individual axial brain slices using 8 rungs birdcage-like coil.

(a) 16 elements birdcage-like coil - $|B_1^+|$ maps

(b) 16 elements birdcage -like coil- SAR maps

Figure 5.22: $|B_1^+|$ *field map (μT) and SAR (watt/Kg) for all four individual brain slices using 16 rungs birdcage-like coil.*

Figure 5.23(a) shows $|B_1^+|$ field distribution using the 32 multi-element coil for all slices. The regularized field maps show a general increase in the area over which a 90 degree flip angle can be achieved. Moreover, the regularised SAR maps, figure 5.23(b) show a decrease in SAR values for all four slices. The SAR values have been decreased to about tenth of the non-regularized SAR values for all slices. The values were decreased by a factor of 10, 20, 13.75 and 10 in the first, second, third and the fourth slice, respectively. Increasing the number of coil elements to be used to 64 improves the homogeneity and feasibility of achieving a 90 degree flip angle over a large field of view with in the individual slices as it is seen in figure 5.24(a). There is a great improvement in the $|B_1^+|$ field distribution as shown from individual brain slices of the non-regularized $|B_1^+|$ fields in compare to the regularized $|B_1^+|$ field maps. In the non regularized $|B_1^+|$ field maps, the central brightening is located mainly in the frontal lobe area. The SAR values have been decreased by a factor of 10 for all slices as seen in figure 5.24(b). Generally, the SAR distribution shows a high reading around the edge of the brain area, on the skin, and the values decreases as the fields penetrated deep into tissues.

The currents' phases and amplitude before and after the optimisation are given in figure 5.20(c) and 5.20(d) for 32 and 64 multi-element coils. The phase behaviour shows opposite trends to each other, the 32 multi-element coil shows a linear increase in the currents' phases while the 64 multi-elements coil show a linear decrease in phases. The magnitude of the currents in both coils are in general linear and approximately equal to that of the non optimised currents value for both coils; interestingly, it is found that the high spikes in both coils are form elements that has the same physical position in the coil.

Table 5.6 shows 1gm and 10gm SAR calculations in $Watt/Kg$ for all four coils comparing the regularized to the non-optimised SAR values. As it has been said earlier in this section, the error in L-curve optimisation parameter reflects

severely on the SAR calculation results for the 8 and 16 rungs coils with the optimised 1gm and 10gm SAR values being higher by the order of 10^9. The 1gm SAR values for 32 multi-elements coil have reduced by a factor of 9 in compare to a reduction by a factor of 2.62 in the SAR values for the 64 multi-transmit element coil. The table also shows that 10gm SAR values for the 32 multi-elements reduce by a factor 8 while that for the 64 multi-transmit elements coil reduced by a factor of 3.
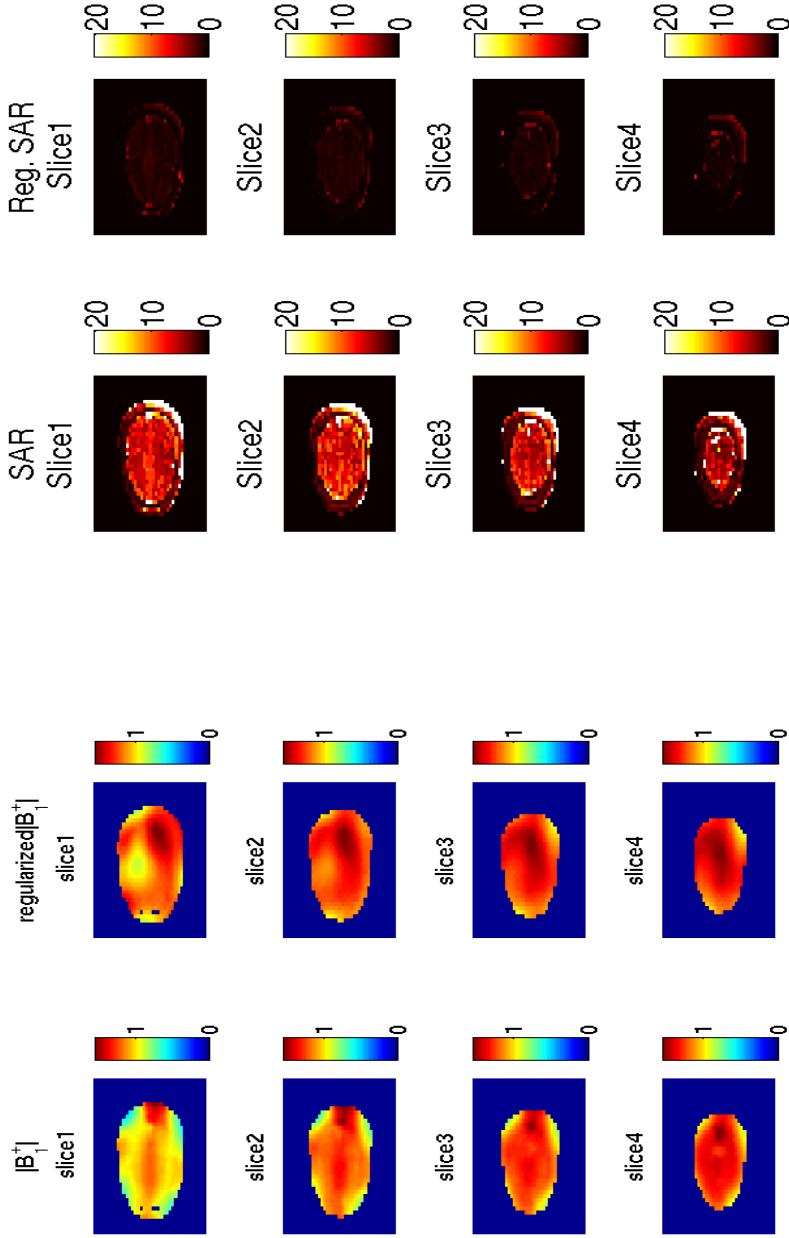
(a) 32 multi-elements coil - $|B_1^+|$ maps

(b) 32 multi-elements coil - SAR maps

Figure 5.23: $|B_1^+|$ *field map (μT) and SAR (watt/Kg) for all four individual axial brain slices using 32 multi-elements coil.*
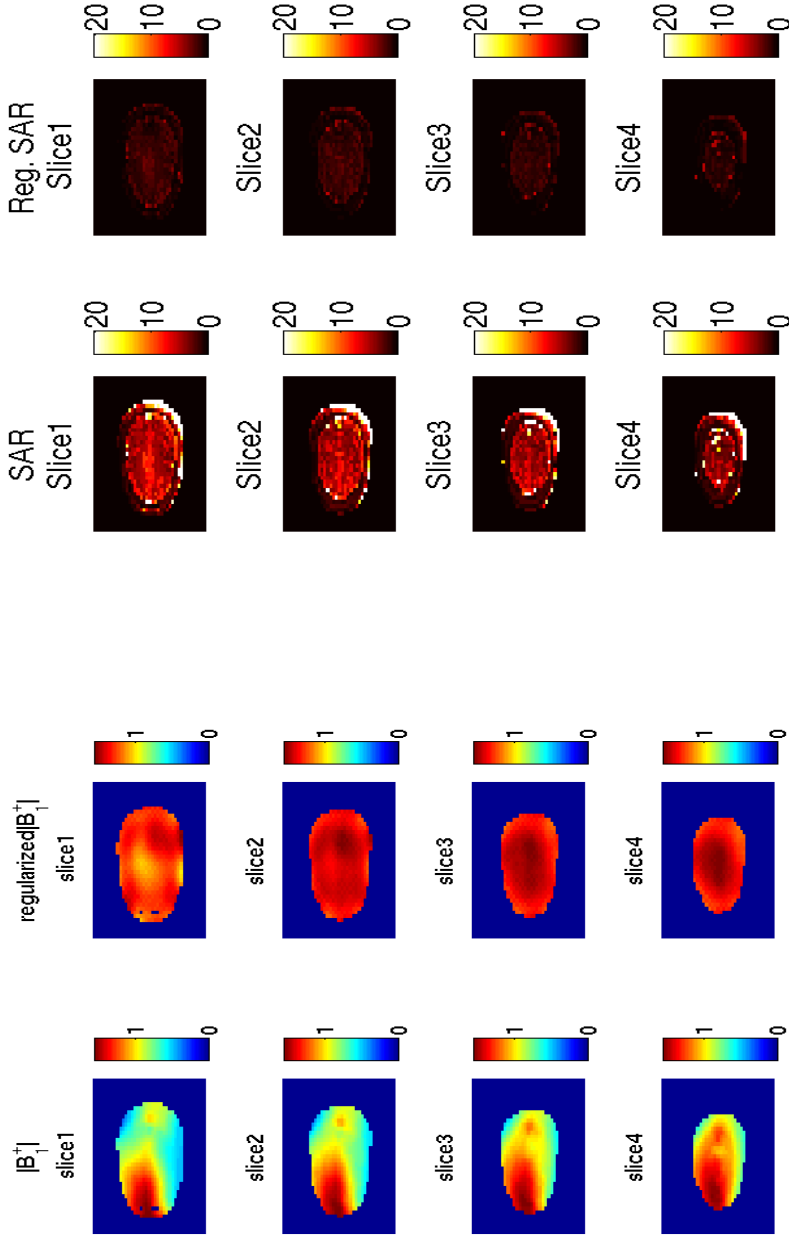
(a) 64 multi-elements coil - $|B_1^+|$ maps

(b) 64 multi-elements coil - SAR maps

Figure 5.24: $|B_1^+|$ *field map (μT) and SAR (watt/Kg) for all four individual axial brain slices using 64 multi-elements coil.*

SAR	8 rungs BC		16 rungs BC		32 multi-elements		64 multi-elements	
	UnReg.	Reg.	UnReg.	Reg.	UnReg.	Reg.	UnReg.	Reg.
1gm	24.25	5.0	28.84	1.22×10^9 *	274.6	30.66	19.46	7.25
10gm	253.78	74.205	288.21	1.56×10^9 *	26.75	3.327	207.85	65.92

Table 5.6: *1gm and 10gm SAR calculations in (Watt/Kg) for all four coils: the 8 and 16 rung birdcage-like coil, 32 and 64 multi-elements coils comparing the optimised (Reg.) to the none optimised values. * the solution is not converged.*

5.6 Summary

The results shown in this chapter demonstrate the use of Tikhanov regularisation technique in conjunction with TLM method results to optimise rotational transmit field uniformity and minimise the SAR values for two and three dimensional birdcage coils. First, a 2-dimensional 8 and 16 rungs birdcage-like coil were simulated using an in-house TLM code to generate the transmit field sensitivity maps for four different slices. For each individual slice, field maps were used in Tikhonov optimisation routine with four different proposed target field maps. The results show that shimming is more difficult for slices where there is a high diversity in tissue types, especially at air (sinus)-tissues, such as slice 1 and slice 2. It is also concluded that the best uniformity results from shimming using TG1 in the optimisation routine for all for slices in both coils. Therefore, TG1 was used subsequently in the 3-dimensioal optimisation.

Second, the 2D TLM simulation and shimming was carried out in 3-dimention for a full physical representation of the problem in hand. Four RF coils have been simulated in this work: 8 rung birdcage coil, 16 rung birdcage coil, 32 multi-elements birdcage coil and 64 multi-element birdcage coil. RF shimming was then preformed for the same four individual slices used in the 2D optimisation. Field maps and currents phases and amplitudes and field uniformity was compared for all four coils. Figure 5.25 shows a summary for the standard coils images and the corresponding optimised images. It was found that the transmit field uniformity increased as the number of coil elements increase. Moreover, the uniformity of a slice is also affected by the degree at which tissue are varied within the same slice. Tissues that are highly varied in properties are more difficult to optimise (shimmed).
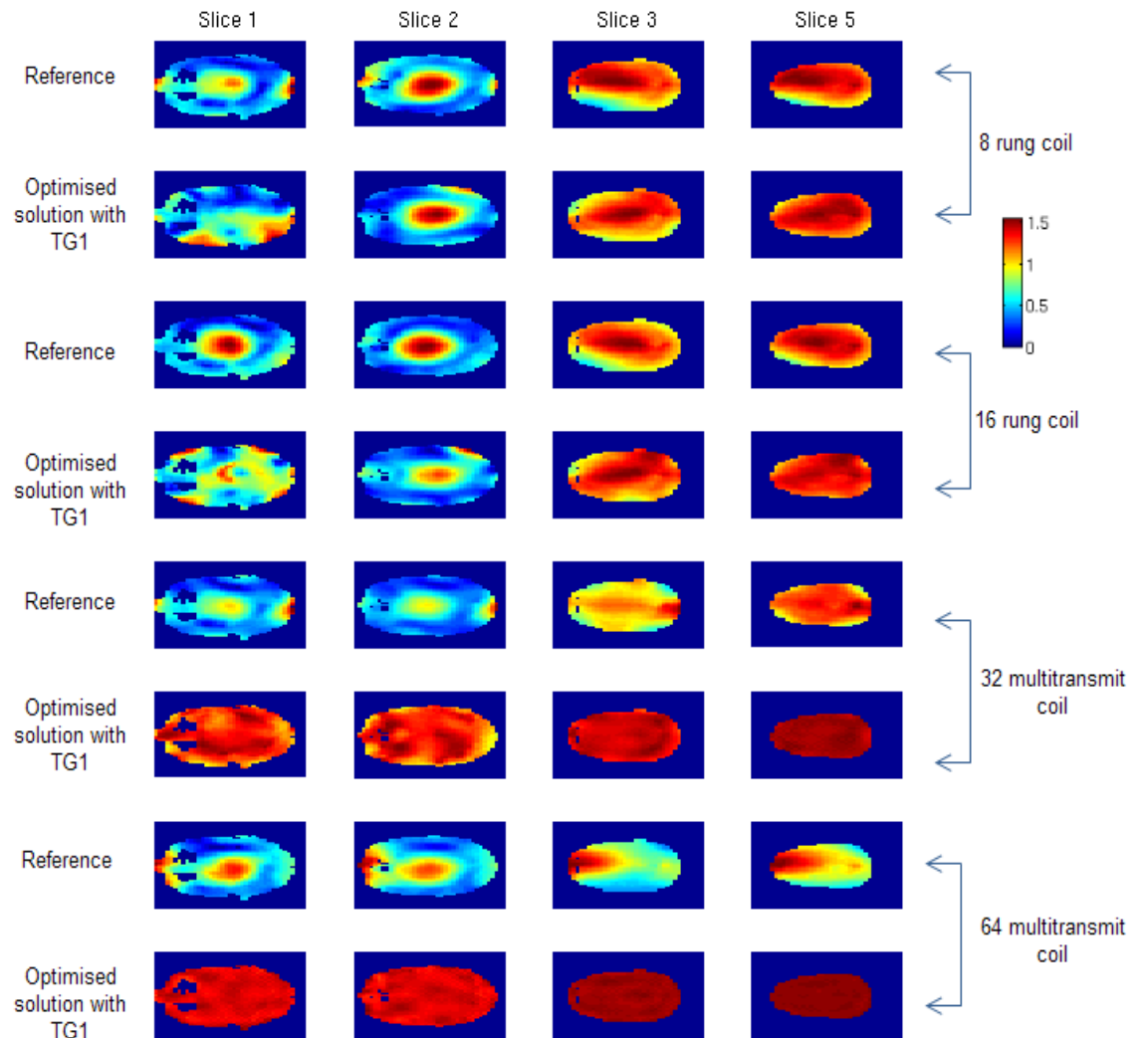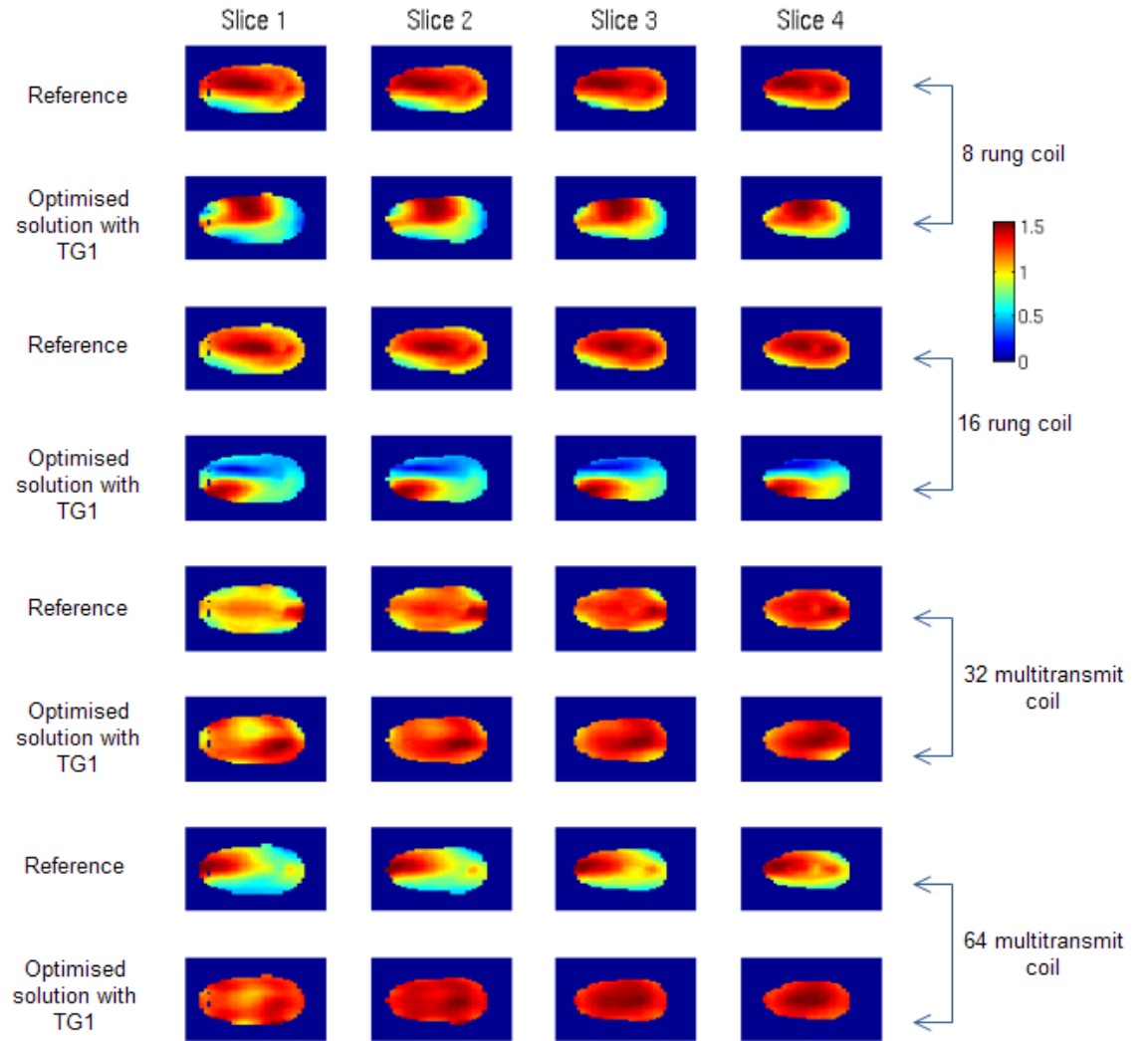
Figure 5.25: *The standard and optimised Rotational field map (μT) for slices (1,2,3 and 5) using 8-rung coil, 16-rung coil, 32 multi-elements coil and 64 element coil.*

Finally, the possibility of optimising RF shimming was also investigated for an assigned volume. The optimisation was carried out for four neighbouring brain slices. The optimisation was done to minimise field inhomogeneity and SAR values. It was found that when the solution is not converged, with a poor L-curve fit, optimisation results are poor. This is evident at low number of rung

coils (8 and 16 rung coils) as highlighted in table 5.6. The rotational field maps for all four successive slices in figure 5.26 show the effect of poor convergence in optimised solutions using 8 and 16 rung coils where fields distribution are non-uniform. The figure also indicates that using higher number of elements improves field distribution in the selective volume of interest in the brain. Similarly, figure 5.27 shows high SAR values for 8 and 16 rung coils where improvement can be noticed for 32 and 64 multi-element coils.

Figure 5.26: *The standard and optimised Rotational field map (μT) for slices (1,2,3 and 5) using 8-rung coil, 16-rung coil, 32 multi-elements coil and 64 element coil.*
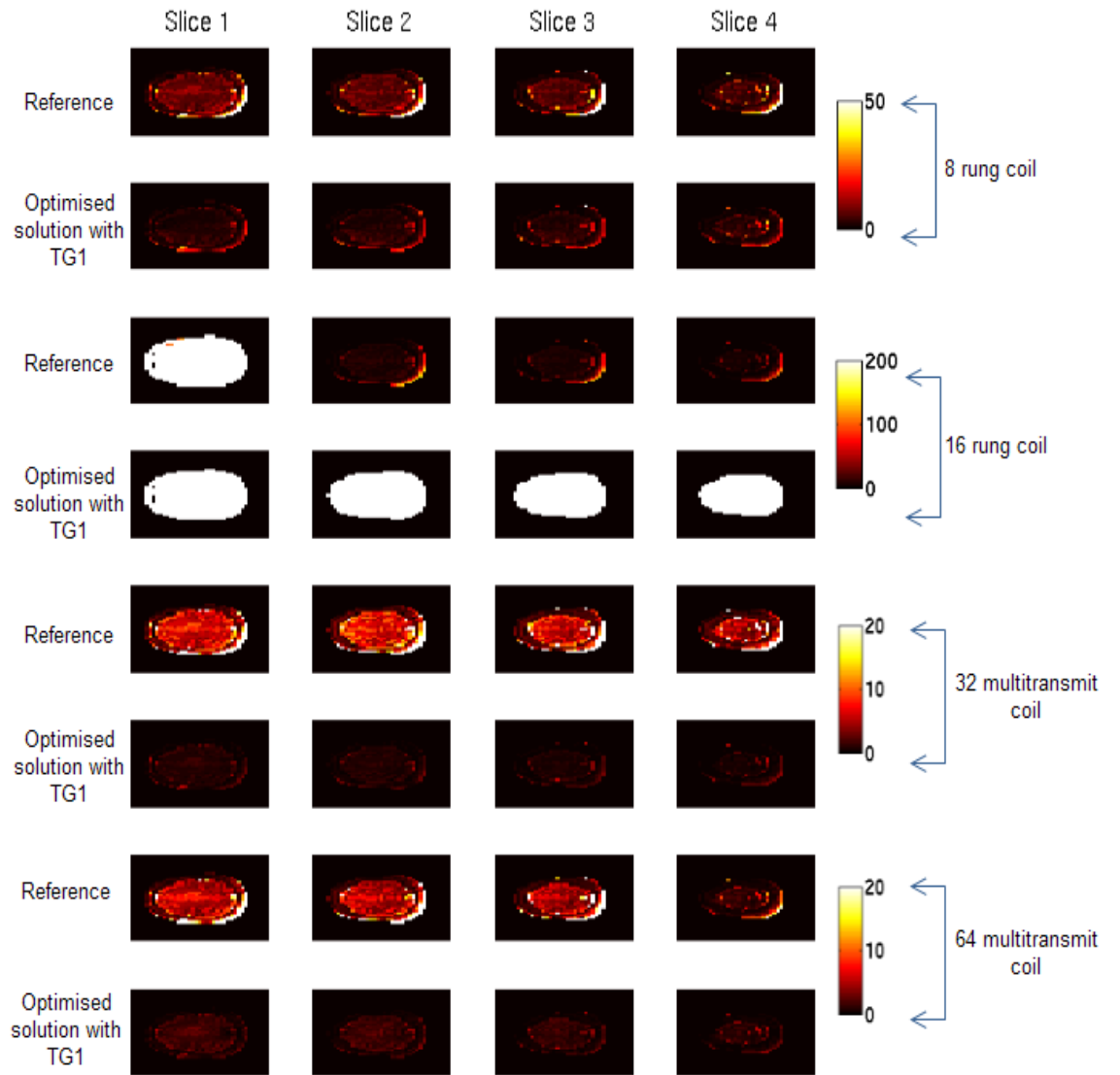
Figure 5.27: *The standard and optimised SAR map (μT) for slices (1,2,3 and 5) using 8-rung coil, 16-rung coil, 32 multi-elements coil and 64 element coil.*

Bibliography

[1] Federal Communications Commision. Tissue dielectric properties. `http://www.fcc.gov/oet/rfsafety/dielectric.html`.

[2] C. Gabriel and S. Gabriel. Compilation of the dielectric properties of body tissues at rf and microwave frequencies. Technical report, United States Air Force, 1996.

[3] P. C. Hansen. Analysis of discete ill-posed problems by means of the l-curve. *SIAM Rev.*, 34(4):561–580, 1992.

[4] P. C. Hansen. The l-curve and its use in the numerical treatment of inverse problems. In *in Computational Inverse Problems in Electrocardiology, ed. P. Johnston, Advances in Computational Bioengineering*, pages 119–142. WIT Press, 2000.

[5] P. C. Hansen. Regularization tools: A matlab package for analysis and solution of discrete ill-posed problems. Technical Report version 4, Informatics and Mathmatical Modelling, Technical University of Denmark,DK-2800, Lyngby, Denmark, 2007.

[6] W. E. Heinz, H. Martin, and N. Andreas. *Regularization of Inverse Problems.* Kluwer Academic Publisher, Netherlands, 2000.

[7] T. S. Ibrahim, R. Lee, B. A. Baertlein, A. Kangarlu, and P. L. Robitaille. Application of finite difference time domain method for the design of birdcage rf head coils using multi-port excitations. *Magn. Res. Imaging*, 18:733–742, 2000.

[8] U. Katscher, P. Boerner, C. Leussler, and J. S. Van den Brink. Transmit sense. *Mag. Reson. Med.*, 49:144–150, 2003.

[9] F. Liu, B. L. Beck, J. R. Fitzimmons, S. J. Blackband, and S. Crozier. A theoretical comparison of two optimization methods for radiofrequency drive schemes in high frequency mri resonators. *Physics in Medicine and Biology*, 50:5281–5291, 2005.

[10] W. Mao, M. B. Smith, and C. M. Collins. Exploring the limits of rf shimming for high-fields mri of the human head. *Magn. Res. Imaging*, 156:918–922, 2006.

[11] W. Mao, Z. Wang, M. B. Smith, and C. M. Collins. Note: Calculation of sar for transmit coil arrays. *Concepts in Magnetic Resonance Part B*, 31B:127–131, 2007.

Chapter 6

Travelling Wave MRI for 7T System

6.1 Introduction

Tremendous advantages have been made in RF coil design, for both body and head coils, to maximize the efficiency. By controlling the coil design a uniform RF transmit field can be achieved. At first, analytical approaches were used in the limits of quasistatic regime for low resonant frequencies. Then, as a result of the breakdown of the circuit models at high field numerical full wave methods were used to design and develop RF coils, the FDTD, FEM and TLM methods. Head coils such as TEM resonators and Birdcage coils have been investigated and designed. Most recently the development of new solutions such as phased arrays concepts have been introduced [5], which are now commercially implemented as multiple receive element coils. With any new technology, the cost versus benefit is always a considerable issue when commercially implemented. The travelling wave approach developed by Brunner et al. [3] is based on replacing the RF coils by an antenna, this is placed at a distance from the region of interest so the tissue is coupled to a travelling wave

NMR signal rather than to standing wave NMR signal as in an RF resonator. It is believed that such system set up will improve the spatial field distribution among the imaged subject and thus provide a high SNR. Such a set up has the advantages of being of lower cost and freeing up space within the magnet bore.

In this chapter, the FDTD method is used to investigate the travelling wave NMR approach. A patch antenna excitation in a loaded 7T scanner is simulated to study the behaviour of the travelling rotating magnetic field in the magnet bore as well as the body, especially the head. The effect of having different matching loads on the head are also considered. Finally, an end tapered waveguide (ETWG) design is suggested for the local imaging. The effect of mode impedances and miss-match of the excitation waveguide and the body loaded magnet bore is then considered. A practical waveguide has been built and demonstrated.

6.2   The Travelling Wave NMR Approach

In terms of transmitting power for RF communications, the waveguide has always been a crucial component for engineering of transmission systems. It has applications in optical communications technology, such as optical fibres, ultra low-loss THz guides, photonic crystal guides and, meta-material guides. Waveguides in their RF form are simply hollow metal pipes mostly of rectangular or circular cross section and which propagate electromagnetic energies with two different modes below the cut-off frequencies. In the case of the TWNMR approach, the transmission and reception of electromagnetic waves is done by transmit and receive coupled antennas which are positioned at the ends of the guide. The modes of operation of the guide is determined by the excitation configuration of the waveguide. Accordingly, the two modes of operation for

any hollow metal waveguide are: a transverse electric mode TE, where the electric field component in the direction of propagation is zero, usually E_z and a transverse magnetic mode, for which the magnetic field component along the direction of the wave propagation is zero, usually H_z.

By solving Maxwell's equations for linear, isotropic and homogeneous medium subject to the boundary conditions at the walls of the guide one can get the electric and magnetic fields distributions (modes). The normal component of the magnetic field at the walls of the conducting tube should vanish to zero and also the electric field component tangential to the walls should also vanish. The general form of Maxwell's equation for the transverse electric mode in term of the longitudinal component H_z in the Cartesian coordinate is given as,

$$\nabla_t^2 H_z + \left(\gamma^2 + \omega^2 \mu \varepsilon\right) H_z = 0 \,. \tag{6.1}$$

For transverse magnetic waves the general form of Maxwell's equation in term of the longitudinal component E_z is given by, [6]

$$\nabla_t^2 E_z + \left(\gamma^2 + \omega^2 \mu \varepsilon\right) E_z = 0 \,. \tag{6.2}$$

6.3   Circular Wave Guides

For circular cross section waveguides which are of concern to this work, Maxwell's equations (6.1, 6.2) in cylindrical polar coordinate are given as

$$\frac{1}{\rho}\frac{\partial}{\partial \rho}(\rho\frac{\partial \psi}{\partial \rho})\varepsilon + \frac{1}{\rho^2}\frac{\partial^2 \psi}{\partial \phi^2} + \kappa^2 \psi = 0 \,, \tag{6.3}$$

where $\kappa^2 = \gamma^2 + \omega^2 \mu \varepsilon$, ψ represents either E_z or H_z. The solution of this equation can be given in term of Bessel function as

$$\psi = J_m(\kappa \rho)cos(m\phi) \,, \tag{6.4}$$

where $J_m(\kappa\rho)$ is Bessel function of the first kind. For a TM mode $\psi = E_z$ has to vanish at the walls $(a = \rho)$,That is

$$J_m(\kappa\rho) = 0 \; or \; \kappa\rho = t_{mn} \quad (m = 0, 1, 2, .., n = 1, 2, 3, ..)\,. \tag{6.5}$$

t_{mn} is the root of the Bessel function, so the longitudinal field component is,

$$E_z = AJ_m(\kappa\rho)\cos(m\phi)\,. \tag{6.6}$$

Accordingly, the propagation constant is given as,

$$\gamma^2 = -\omega^2\mu\varepsilon + (t_{mn}/a)^2\,. \tag{6.7}$$

Below the so called the cut-off frequency of the wave guide the electromagnetic waves bounced back and forth in the guide in a standing wave pattern; consequently, no wave will propagate down the waveguide and the power will rapidly dissipate. The TM mode cut-off frequency can be calculated to be

$$f_{mn} = \omega_{mn}/2\pi = t_{mn}v/2\pi a\,. \tag{6.8}$$

On the other hand, for a TE mode where $\psi = H_z$, equation (6.3), it is the derivative of the field component that has to vanish,

$$J'_m(\kappa\rho) = 0 \; or \; \kappa\rho = s_{mn} \quad (m = 0, 1, 2, .., n = 1, 2, 3, ..)\,, \tag{6.9}$$

where s_{mn} is the root of the Bessel function derivative.

The longitudinal magnetic field component along the guide and the propagation constant of the wave are given as

$$H_z = AJ_m(\kappa\rho)\cos(m\phi)\exp(-\gamma z)\,, \tag{6.10}$$

and,

$$\gamma^2 = -\omega^2\mu\varepsilon + (s_{mn}/a)^2\,, \tag{6.11}$$

respectively. As for the TM modes the operating frequency has to exceed the cut-off frequency for the waves to propagate and is given as, [6]

$$f_{mn} = \omega_{mn}/2\pi = s_{mn}v/2\pi a\,. \tag{6.12}$$

The guide wavelength along the direction of propagation of the modes is given by

$$\lambda_g = \frac{\lambda}{\sqrt{1 - (\frac{f_c}{f})^2}} \, . \qquad (6.13)$$

The lowest cut-off frequency is the TE_{11} which makes a uniform axial magnetic field along any MRI magnet bore. For the 7T MRI system where the magnet bore is of 58 cm diameter it has a cut-off frequency which is 5 MHz above the resonance frequency of the hydrogen atom (298 MHz). Tables (6.1) and (6.2) give the first three TE and TM modes of excitation for the 7T magnet bore and their corresponding cut-off frequency. It is well seen from equation (6.8) and equation (6.12) that a wide magnet bore is needed to bring the cut off frequencies below the RF NMR frequencies at high fields [3]. However, it is believed that having the scanner loaded with the body which is considered as inhomogeneous dielectric reduces the cut off frequency below 303.1 MHz to the Hydrogen resonant frequency.

(m,n)	s_{mn}	f_{mn} MHz
TE_{11}	1.841	303.1
TE_{12}	5.331	877.7
TE_{01}	3.832	630.78

Table 6.1: *The first three TE modes for the 7T magnet bore*

(m,n)	t_{mn}	f_{mn} MHz
TM_{01}	2.405	395.8
TM_{11}	3.832	630.7
TE_{02}	5.520	908.5

Table 6.2: *The first three TM modes for the 7T magnet bore*

6.3.1   Power Flow and Dissipation

The power flow is, in general the rate at which an electromagnetic wave travel through a surface and is calculated by the Poynting vector $\mathbf{S} = \mathbf{E} \times \mathbf{H}$. In wave guides, the total power flow within these guides is the sum of all modes propagating power and is usually given as the total average power of the real part of the complex Poynting vector over the guide's cross section , [4, 6],

$$P_{flow} = \frac{1}{2} \int Re[\mathbf{E} \times \mathbf{H}^*] \cdot d\mathbf{S} \, . \tag{6.14}$$

The divergence of the average power flow can represents the energy transformed per unit volume per second into heat, which can interpreted as the power dissipated in the medium,

$$P_{dissp} = \frac{1}{2} \int \mathbf{E}^* \cdot \mathbf{J} dV \, . \tag{6.15}$$

Based on energy conservation this means that the energy flow out of a surface of closed volume equivalent to the time rate of decrease of energy stored in electric and magnetic fields in the volume and the ohmic power dissipated as a heat within that same volume.

For an unloaded wave guide the power flow for the TM_{mn} mode is

$$P = |A|^2 \omega \mu \beta a^4 B_{mn} \, ; \tag{6.16}$$

While the power flow for the TE_{mn} is calculated as

$$P = |A|^2 \omega \mu \beta a^4 A_{mn} \, , \tag{6.17}$$

where B_{mn} and A_{mn} depend on mode indices,[6].

6.3.2   Input and Receiving Energy in Waveguides

Mostly, there are three devices that are used to inject and receive energy from guides. These are probes, loops and slots. The later is also called an aperture or a window. In a rectangular waveguide, the centre of the widest dimension

of the guide is where the probe is mostly located and it is at a quarter-wave length distance from the short end of the guide based on the dominant mode frequency. At this position the E lines detach from the guide at its highest intensity where energy coupling is at its maximum. Energy also can be injected in the guide by introducing a magnetic field, when a high current with frequency in the permitted range of the waveguide is carried by the loop, energy is transferred. When apertures are used, E lines expand through the slot to the entire guide. Choosing the proper size of the slot is crucial in minimizing energy reflection.

In NMR travelling wave experiments, patch antennas have been used to generate a rotating RF magnetic fields that can couple to the nuclear magnetization with in the region of interest in the 7T system magnet bore [1, 2, 3, 7].

6.4 Patch Antenna Design:The Effect of different dielectric matching on the field homogeneity in the head and neck

6.4.1 Patch Antenna Design and Simulation

The xFDTD Bio Pro(Remcom Inc.) was used to run simulations of the magnet bore loaded with a standard body model and patch antenna in order to study the effect of different matching loads on the head. The magnet bore is modelled as a 58 cm diameter cylindrical tube of 3 cm thickness and 220 cm long. The body model is reduced to the half in order to reduce the simulation time which is approximately 7 hours for half of the body. Moreover, field interactions in the head are of the only interest in this part of the study. A patch antenna consists of three parts: dielectric substrate, ground plate and the patch, figure 6.1(a). The dielectric constant of the substrate ε_r, the height of the substrate h and the resonance frequency of the circular patch dominant mode f_r determine the radius of the patch a as,

$$a = \frac{F}{\sqrt{1 + \dfrac{2h}{\pi \varepsilon_r F} \left[\ln \left(\dfrac{\pi F}{2h} \right) + 1.7726 \right]}} \tag{6.18}$$

$$F = \frac{8.791 \times 10^9}{f_r \sqrt{\varepsilon_r}}.$$

A patch antenna was simulate with a 23 cm diameter ground plate; a substrate of 1.1 cm thickness and 20 cm diameter and $\varepsilon_r = 2$; and a 18.3 cm diameter patch. Two orthogonal driving ports 11 cm away from the antenna centre were used. The patch antenna was positioned 55 cm away from the head. First, in order to calculate the resonant frequency of the patch antenna a 32-time step length Gaussian pulse was applied across one port and, the field calculation were set for 38000 time step. The patch antenna was 'tuned' to 297 MHz.

Figure 6.1(b) shows the resonant frequency for the patch antenna.

In order to calculate the rotational field maps and study the effect of adding
matching loads on fields homogeneity and SAR values, two orthogonal coaxial
feeds were driven by 1 A sinusoidal current, 50 Ω to generate a circular po-
larized field at 296.9 MHz. Four different matching loads were tested in this
study, cylindrical load, tapered cylinder, mask and a combination of a mask
and a tapered cylinder, figure 6.2. Each matching load was tested at three
different dielectric values $\varepsilon_r = 43.5, 54.5, 60$. Table (6.3) gives the description
of each matching load.
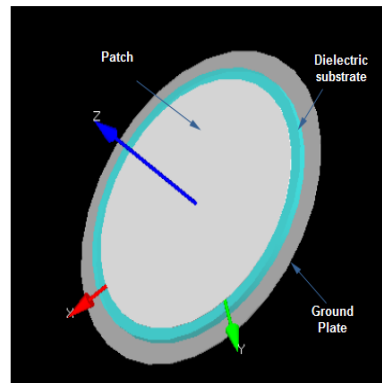
(a)
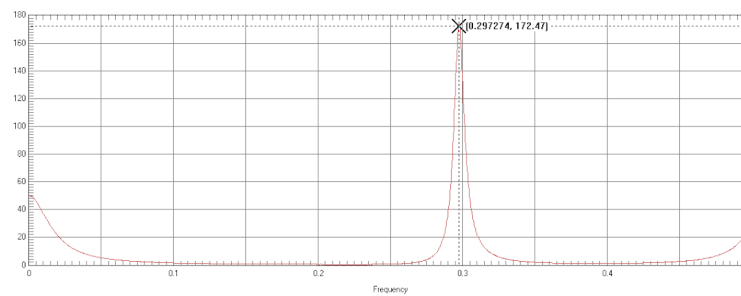
(b)
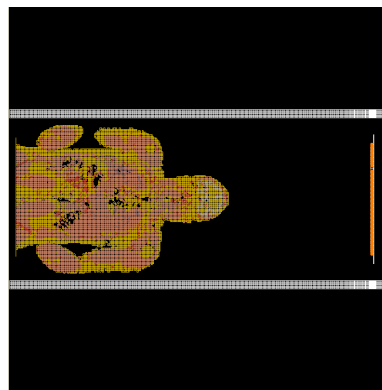
(c)

Figure 6.1: *(a) shows the patch antenna geometry, (b) shows the patch antenna tuned at 297 MHz, and (c) shows the patch and body set up*
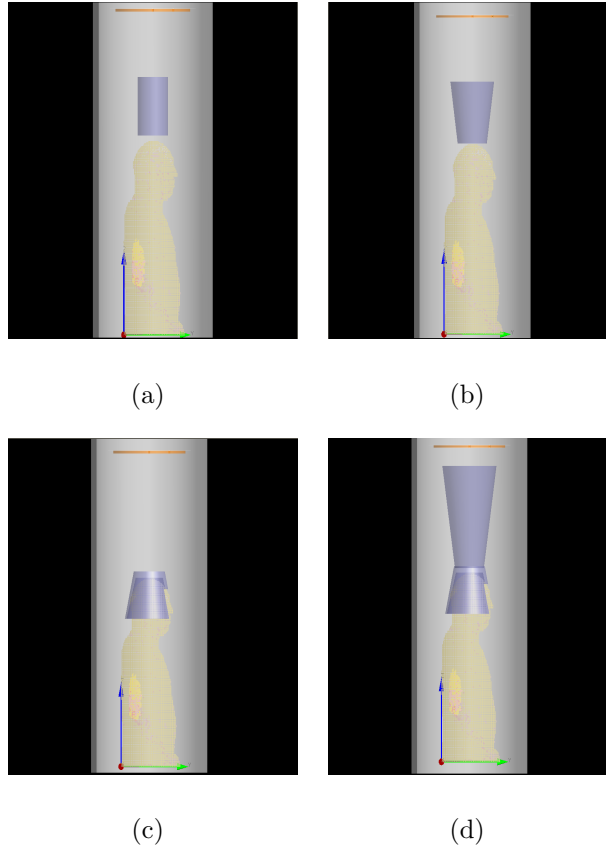
Figure 6.2: *Shows the different matching loads geometry: (a) cylindrical match; (b) tapered cylinder; (c) mask load and; (d) mask and Tapered cylinder.*

Matching load	description
Cylinder	hight = 25 cm, base radius= 8 cm
Tapered cylinder	hight = 25 cm, small base radius= 8 cm, wide base radius= 12 cm
Mask	two tapered cylinders subtracted from each other with and opening made for the face; hight= 18 cm, inner small base radius= 8.5 cm, inner wider base radius = 13.5 cm and thickness = 1 cm.
Mask with tapered cylinder	The tapered cylinder is of 45 cm hight, small base radius = 8 cm and large base radius =12 cm.

Table 6.3: *Geometry of matching loads used in simulations. Each load has three different dielectric values $\varepsilon_r = 43.5, 54.5, 60$.*

6.4.2 Simulation Results: Power Flow and SAR Values

For all four matching loads the rotational fields were calculated for two axial slices and compared to the those of the patch antenna without a matching load. first slice passes through the brain and the second passes through the eyes, figure 6.3(a) and 6.3(b) respectively . The power flow was calculated using the transverse component of equation (6.14) and the root mean square fields values over the last time cycle.

Any RF probe used in an MR experiment will generate an electric field associated with B_1 rotational magnetic field. The electric field in tissues causes tissue heating. Therefore, knowing SAR values that a probe produces for specific input power help to set deposited power limits for RF probes. The 7T Philips system software calculates the safe input power of a specific conventional coil using a scaling factor K_{sar} for any specified pulse sequence. The scaling factor is defined as the local SAR (10gm Avg.) in tissue to the square of the B_1 field.

$$ K_{sar} = \frac{Max\,10gm\,Avg\,SAR}{B_1^2}, \qquad W/kg/\mu T^2. \qquad (6.19) $$

The xFDTD software calculates max. avg. 10 gm SAR in tissues. SAR safety parameter K_{sar} is first calculated using equation (6.19) for the software input power. Theses values are then used to calculate the safety parameter for a field strength of $5.9\,\mu T$ which is the field strength necessary for tipping spins 90° with a 1 ms rectangular RF pulse. Finally, the energy deposition into the body for 120 of the (1 ms) 90° RF pulse/second is calculated and averaged over 6 min.

Figure (6.3(c) - 6.3(f)) shows graphs of the power flow and the corresponding SAR values for all matching loads compared to the patch-body set-up only. For slice 1, graph 6.3(c) shows that the highest power flow is for the mask and tapered cylinder with $\varepsilon_r = 54.5$. SAR value for the same matching loads

and dielectric value, see graph 6.3(e), is the second lowest value in all set-ups and is as twice as high as SAR value for same matching configuration with $\varepsilon_r = 43.5$. In addition, the uniformity measures in graph 6.3(g)) shows that the highest uniformity is for the mask and tapered cylinder configuration with $\varepsilon_r = 54.5$. In general, mask and tapered cylinder configuration with all dielectric values under study has the highest power flow, relatively low SAR and high uniformity for slice 1. The graphs (6.3(d),6.3(f), 6.3(h)) for slice 2 confirm the results from the first slice. The mask and tapered cylinder with $\varepsilon_r = 54.5$ gives the best uniformity but 32.25 % higher SAR and 12 % lower power flow than the same configuration with $\varepsilon_r = 60$ gives. The graphs also shows that adding a head mask or pads around the head will not necessarily improve uniformity or decrease heating as sometimes used with conventional head coils. The average field in-homogeneity of a slice 1 with a mask matching load is 55 % on average for all dielectric values while it is 66.76 % on average for all dielectric values for slice 2.
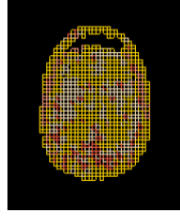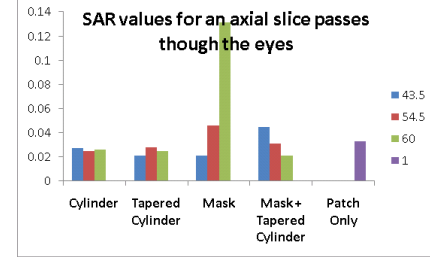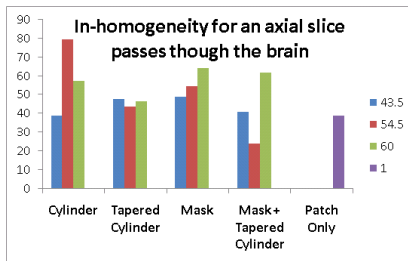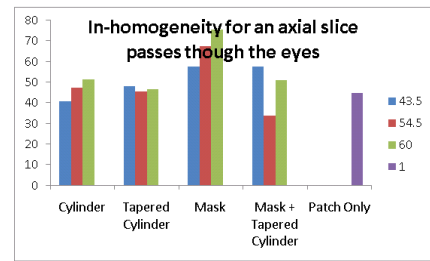
(a) Slice 1
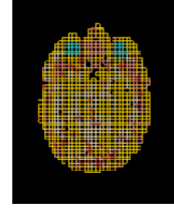
(b) Slice 2
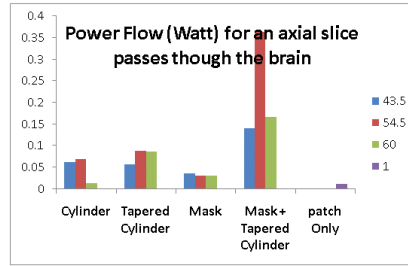
(c)
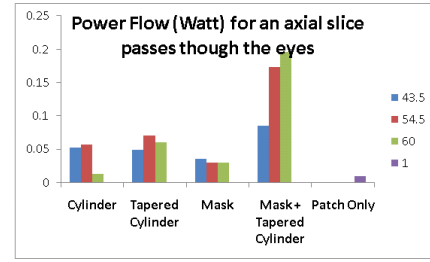
(d)
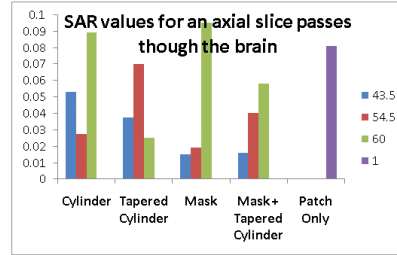
(e)

(f)

(g)

(h)

Figure 6.3: *The two axial slices and their corresponding charts; charts (c, d) are for the power flow (Watt); charts (e, f) are for SAR (Watt/kg) and; charts (g, h) are for field inhomogeneity (%) for all four different matching loads in compare to the patch-body only. Mask and tapered cylinder load with $\varepsilon_r = 54.5$ give high power flow, low SAR value and low field inhomogeneity for both slices.*

6.4.3   Simulation Results: Transmit Rotational Field B_1 Maps

Figure 6.4 shows the transmit field distribution normalized to 1 Watt input power in an axial slice passing through the brain when a tapered cylinder is combined with a mask positioned between the head and the patch antenna in comparison to that of a mask load only used to match the head. The results are for dielectric values $\varepsilon_r = 43.5, 54.5$ and 60. In both cases the field maps are compared to the maps obtained when no load is used for matching. The images show how the field pattern changes for the same matching load as the dielectric values are changed. Using a tapered cylinder combined with mask with, $\varepsilon_r = 43.5$, shows a hot spot field pattern which is a usual pattern of conventional coil operating at ultra high field. The field distribution with patch antenna shows a more even field distribution than tapered cylinder with mask of $\varepsilon_r = 43.5$ but the transmit rotational field value is smaller by a factor of 4. However, using a dielectric value of $\varepsilon_r = 54.5$ in the matching taper improves the field pattern where the field becomes less focused in the brain tissues. In comparison to that, using a mask only as a matching load does not improve the field distribution for all dielectric values. Hot spots are evident for all dielectric values. Moreover, in-homogeneity in the slice for all three dielectric values are better than that when patch only have been used.

Figure 6.5 shows the transmit field patterns normalized to 1 Watt input power for a slice passing through the eyes for two matching loads, tapered cylinder with mask and mask only with different dielectric values $\varepsilon_r = 43.5, 54.5$ and 60. The field patterns are compared to that of the patch antenna only. Looking at the transmit field pattern for the tapered cylinder with mask, the fields are localised to form a hot spot for a dielectric value of $\varepsilon_r = 43.5$ in comparison to field pattern of patch and body only. Moreover, the transmit field values

for 1 Watt input power is 2 half that of the patch and body only. Using a
dielectric value of $\varepsilon_r = 54.5$ will also reduce field localising and increases the
transmit field values 2.5 times that of the patch and body only. Using a mask
only as a matching load localise field values to form a hot-spot in the brain
and increases the field values by a factor of 2 in compare to the field values of
patch and body only.

In general looking into the results of the two axial slices that are 3 cm a part,
there is consistency in the result in term of field distribution and uniformity.
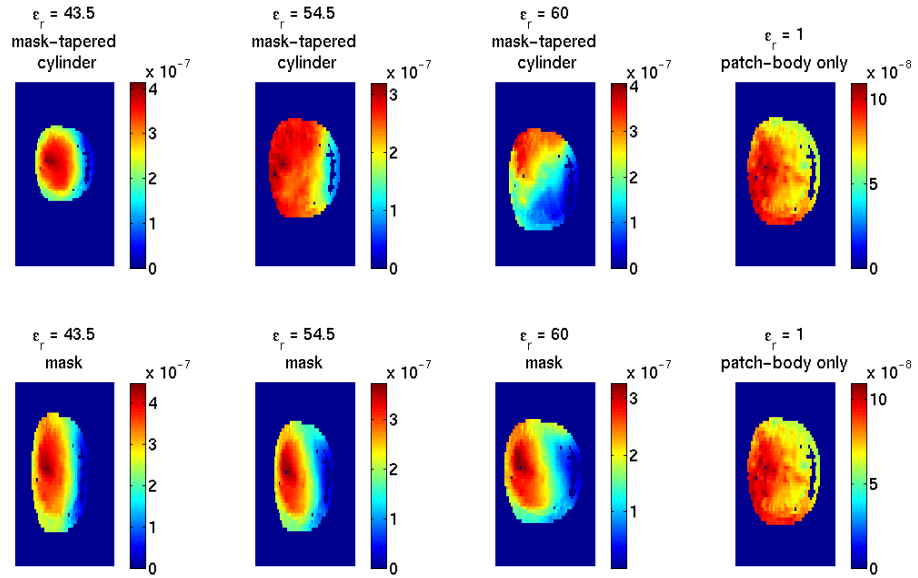
Figure 6.4: *Field maps of a slice passing through the brain; top: for tapered
cylinder with match $\varepsilon_r = 43.5, 54.5, 60$ and; bottom: for mask match with
the same dielectric values both compared to the field maps of the same slice
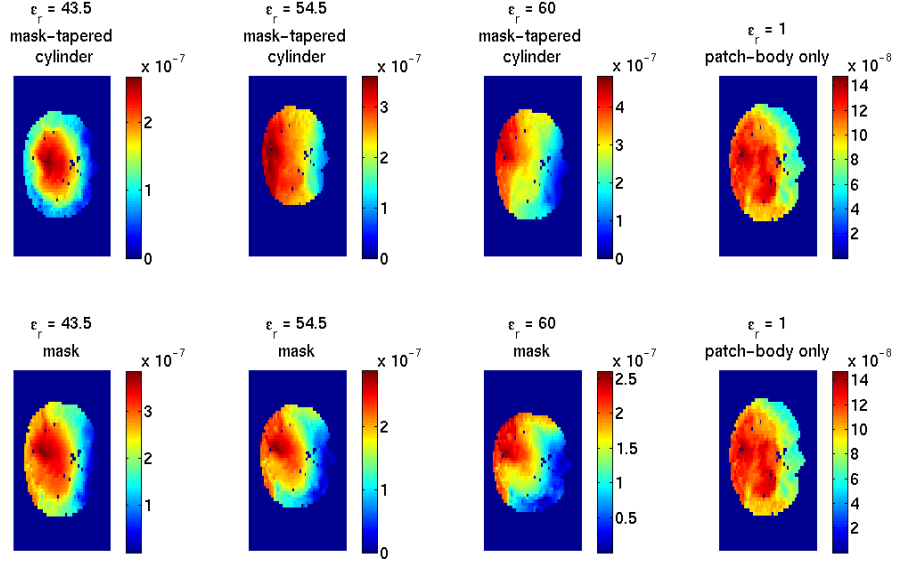with no matching load.*

Figure 6.5: *Field maps of a slice passing through the eyes; top: for tapered cylinder with match $\varepsilon_r = 43.5, 54.5, 60$ and; bottom: for mask match with the same dielectric values both compared to the field maps of the same slice with no matching load.*

6.5   Waveguide design for local Imaging

Most of the travelling wave studies have concentrated on head/foot images and have used antennas or designs that are difficult to move around in the scanner for local imaging, such as, for abdominal or cardiac images. In this section an end-tapered wave guide is proposed for local imaging. An xFDTD simulation was first conducted to test the feasibility of the design. The power flow and dissipation and SAR value is calculated in tissues as well as the B_1 field maps. The wave guide is built and tested and further optimisation is suggested.

6.5.1   Simulations: End Tapered Waveguide Design

Travelling wave NMR was numerically investigated for the 7T MRI system using the finite Difference Time Domain method , xFDTD(RemCom) software with 5 mm per cubic cell standard man model (HUGO). The body model is accommodated in a 58cm diameter and 190cm length waveguide which is of the same diameter length of the 7T(298 MHz) magnet bore, also included is a plastic shield of 50 cm diameter and 2.5 dielectric constant, which is modelled to account for the gradient casing and the bed in the real 7T system. The total grid size is $164 \times 164 \times 415$ cells.

In order to study the field distribution and penetration in a local imaging region (abdominal), a simple end tapered circular waveguides (ETWG) have been proposed. The choice of such a design might improve the quality of the images, reduce the space usage within the scanner, increase the comfort of patients and reduce sample losses due to coil-sample coupling. The end tapered wave guide was designed as a circular wave guide of 10 cm diameter and $\approx 1.5\lambda_g$ length, tapered diagonally over $\approx \lambda_g/2$ length from the opening of the guide and filled with dielectric material $\varepsilon_r = 54$, in which $\lambda_g = 22.5$ cm. These criteria are chosen such that the cut off frequency is 20% below the

excitation frequency of the wave guide which is 298 MHz, the NMR frequency necessary for the excitation of the TE_{11} mode of the loaded 7T magnet bore. The wave guide was driven by one port, 1 volt, 50 Ω, 298 MHz sinusoidal voltage. Figure 6.6 shows the simulation geometry of the loaded scanner. The simulation results shows an impedance of 1.17 + j15. A matching circuit will be built for matching the end-tapered wave guide to 50Ω cables while field maps will be post processed and scaled.
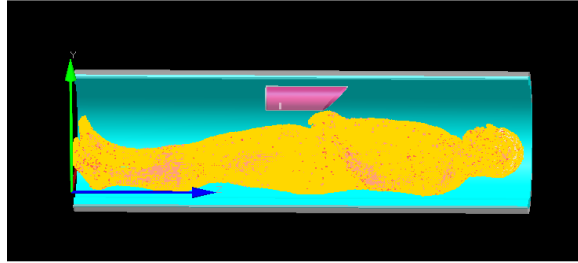
Figure 6.6: *End Tapered Waveguide Geometry.*

6.5.2   Simulations Results: B_1 fields, SAR values and Power flow

The complex fields data produced by the xFDTD program were post processed by matlab program developed for MRI calculations. Figure 6.7 shows field maps for an axial body slice 3.5 cm distance from the end tapered waveguide (ETWG), coronal slice 7 cm below the ETWG and a sagittal slice passing through the middle of the body. All field maps are normalized to 1 Watt input power. In general, there is a non-uniform field distribution in all slices across the whole body slices. As the fields penetrate deeper in tissue the field intensity decreases as expected. Reducing the field of view to a certain region, for example the abdominal region, might increase the overall homogeneity. The xFDTD program calculates local SAR values, 10 gm average SAR, according to equation (4.28) in chapter four. Figure 6.8 shows local SAR distribution over an axial slice of the body at 3.5 cm away from the tip of the end tapered waveguide (ETWG), over the abdominal region at 3 cm depth in the body and, over a sagittal slice passes the middle of the body. Both axial and sagittal slices show higher SAR values near the abdominal region which decreases as the field wave penetrates deeper into tissue. The high SAR in neck and head is as a result of the TE_{11} mode propagation down the magnet bore.

The transverse component of the power flow was calculated by equation (6.14) using the root mean square fields values over the last time cycle. Figure 6.9, bottom shows the normalized power flow in the body only at distances of (3.5, 7, 9.5, 12, 15, 21) cm in foot-head direction. Overall, the normalized power flow shows a decreasing trend. At 3.5 cm away from the waveguide the power flow is less than 3.5 cm later in distance then the values continue decreasing. This is a result of the area in the body model which corresponds to the air gap in body tissue; hence, the power flow is zero. Figure 6.9, top: shows power

flow trend in anterior-posterior direction at (7, 9, 11, 19, 21)cm depth in torso region. The power flow decreases as B_1^+ penetrates deeper into tissues.
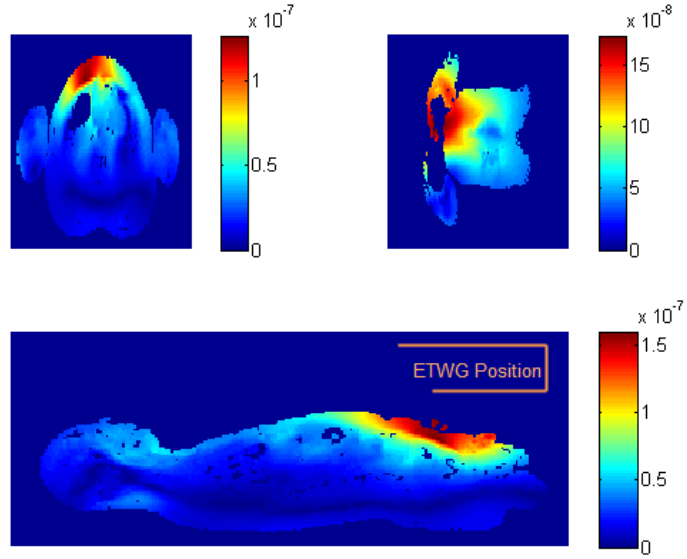

Figure 6.7: B_1^+ *Field maps; Top left: axial slice; top right: coronal slice; bottom: sagittal slice.*
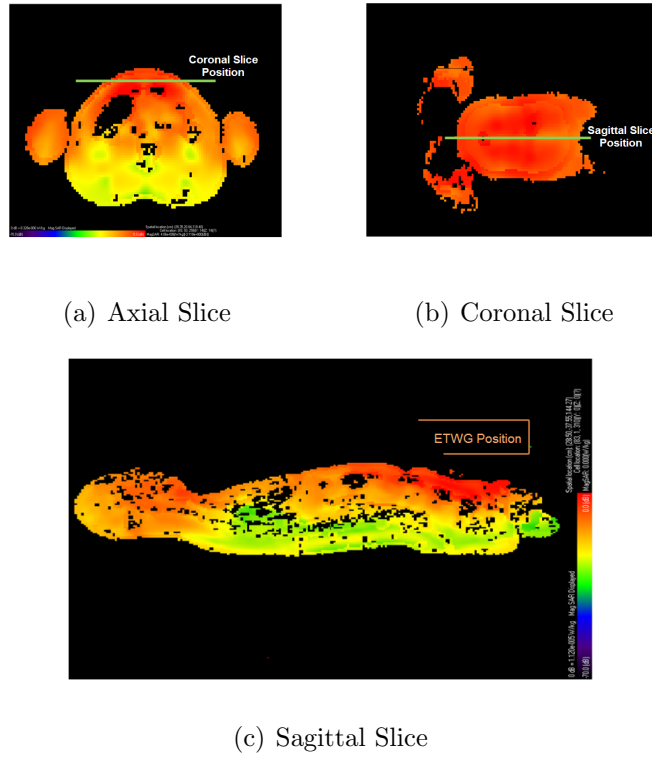
(a) Axial Slice   (b) Coronal Slice

(c) Sagittal Slice

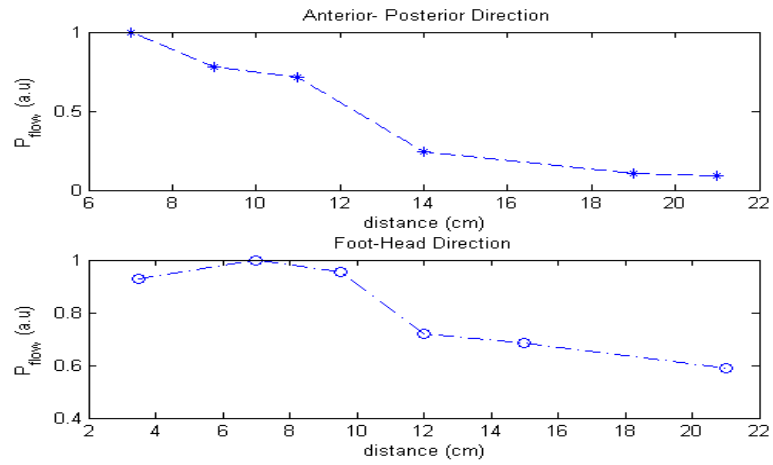**Figure 6.8:** *Local SAR distribution in the body, in axial, coronal and, sagittal slices*


Figure 6.9: *The power flow as a function of distance ; Top: the normalized power flow with distance in the anterior-posterior direction; Bottom: the normalized power flow with distance in the foot-head direction.*

6.5.3 Bench Test

The waveguide was constructed as a Perspex hollow tube covered with a copper sheet and filled with a Methanol water mixture. Two dipoles 90° apart from each other were used as quadrature driving ports. The position of the driving ports was found by adjusting the distance to the backplate until the frequency tuned to 295 MHZ at 5.5 cm distance from the backplate. Two screws 2 cm away from the driving ports were also used to fine tune the waveguide to 298 MHz. Figure 6.11 shows a diagram of the end tapered waveguide (ETWG). To summarise, tuning the wave guide was a result of changing probe position, dielectric concentration, and screw lengths. In order to match the end tapered waveguides' driving ports to 50 Ω cable, two quarter wavelength lines and associated matching networks were used. The quarter wavelength cable is constructed as 16.6 cm length RG223 coaxial cable attached to an N-type connector. Ceramic trimmer capacitors were used first to find the necessary capacitance values to match each probe to 50Ω cable. Then they were exchanged for high voltage fixed capacitors. The first and second port measured an impedance of $50.46 - j1.5\Omega$ and $50.38\Omega - j445m\Omega$ at 298 MHz, respectively. Figure 6.10 shows the matching circuit for the end tapered waveguide (ETWG).
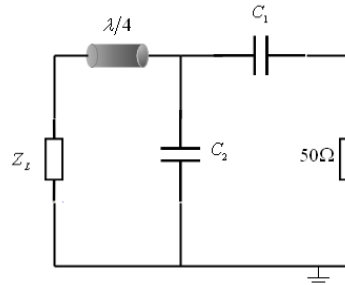
(a) Matching Network
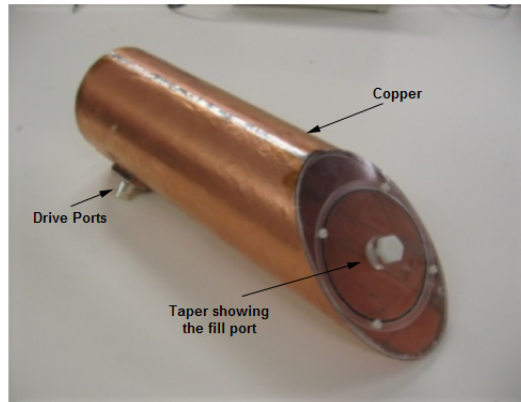
(b) End Tapered Waveguide

Figure 6.10: *End tapered waveguide:(a) matching Network where Z_l represents the waveguide and,(b) End teapered waveguide prototype.*

6.5.4   Experimental Evaluation of the Probe

The end tapered waveguide was tested on a 7T Acheiva system to image a small cylindrical phantom. The phantom was filled with (KCl and CuSO4) solution and is of 5.5 cm diameter and 10 cm long. The end tapered waveguide was used as a transmitter positioned 42 cm from the centre of the phantom and a wrist surface coil was used as a receiver, figure 6.11 show a diagram describing the end tapered waveguide (ETWG) and the imaging set up in the 7T system. The phantom was imaged using a standard GE survey with TR/TE=100/3.2, ACQ Vx. =1.02,1.35,6 at two flip angles: 15 and 30. Figure 6.12 shows axial and sagittal images for the phantom at two different flip angles, 15 and 30 degrees.
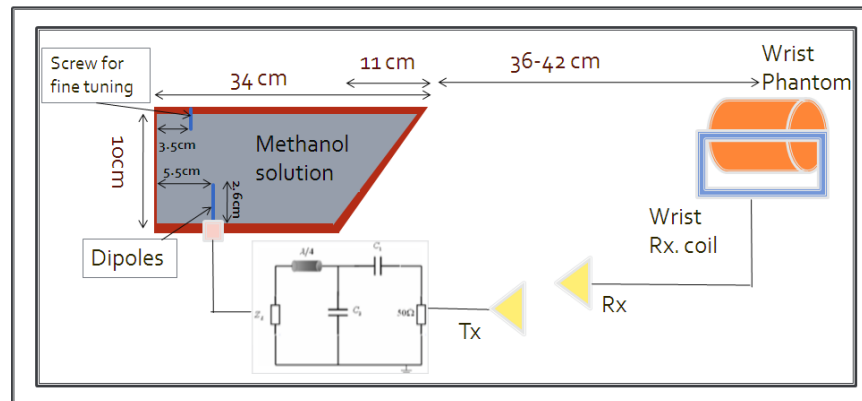

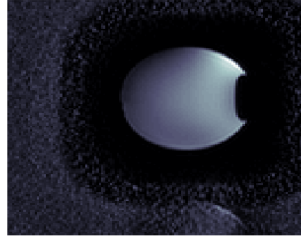**Figure 6.11:** *Diagram represent the imaging setup for 7T Philips Achieva system*
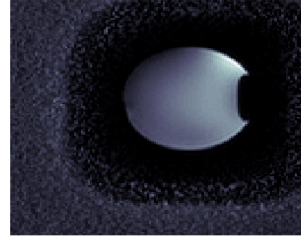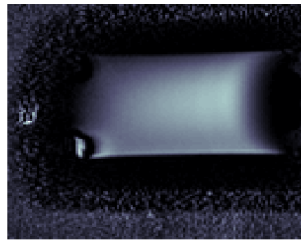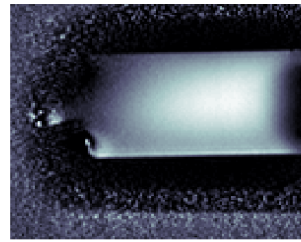
(a) Axial slice - 15°

(b) Axial slice - 30°

(c) Sagittal slice - 15°

(d) Sagittal slice - 30°

Figure 6.12: *Central slices imaged by end tapered waveguide and wrist receive coil :axial slice at (a) 15° flip angle, (b) 30° flip angle; sagittal slices (c) 15° flip angle and, (d) 30° flip angle.*

6.5.5   Optimizing the ETWG Power Scale and Flip Angle

The ETWG coil file in the 7T Acheiva system was optimized to acquire better images at higher flip angle. There are four important parameters in the coil file that adjust the level of power delivered by the amplifier to the transmit interface box and, therefore to the coil. They are: Ref. B_1, maximum B_1 available, maximum average power and, Ref. scale. The maximum average power was fixed to 400 Watt, the maximum B_1 available was fixed to 10 μT, the Ref. B_1 was set to 7 μT and the Ref. scale scale value was set first to 0.66. A standard Gradient Echo Survey was used for imaging the wrist phantom with TR/TE = 5.9/2.0 ms, ACQ Vx.= 1.02,1.35,6 mm. Philips 16 channel head receive coil with sense reconstruction method was used as a receiver and the ETWG as a transmitter. About 38 cm distance was between the phantom and the tip of the ETWG. Starting with a 10° flip angle, images where acquired for the coil file and then flip angle was incremented by 10°; when power is exceeded maximum limit for the system, the Ref. scale value reduced and the imaging process is repeated for different flip angles until the upper limit of flip angle reached 150°. For each process the signal from the highest intensity region in the image (chosen field of view) versus flip angles is plotted in order to define the actual 90 degree flip angle. The maximum flip angle is achieved with Ref, scale value of 0.14. Figure 6.13 shows the signal intensity as a function of flip angle for an axial, coronal and sagittal slices pass throgh the centre of the phantom over a region of interest of about 5×5 pixels.
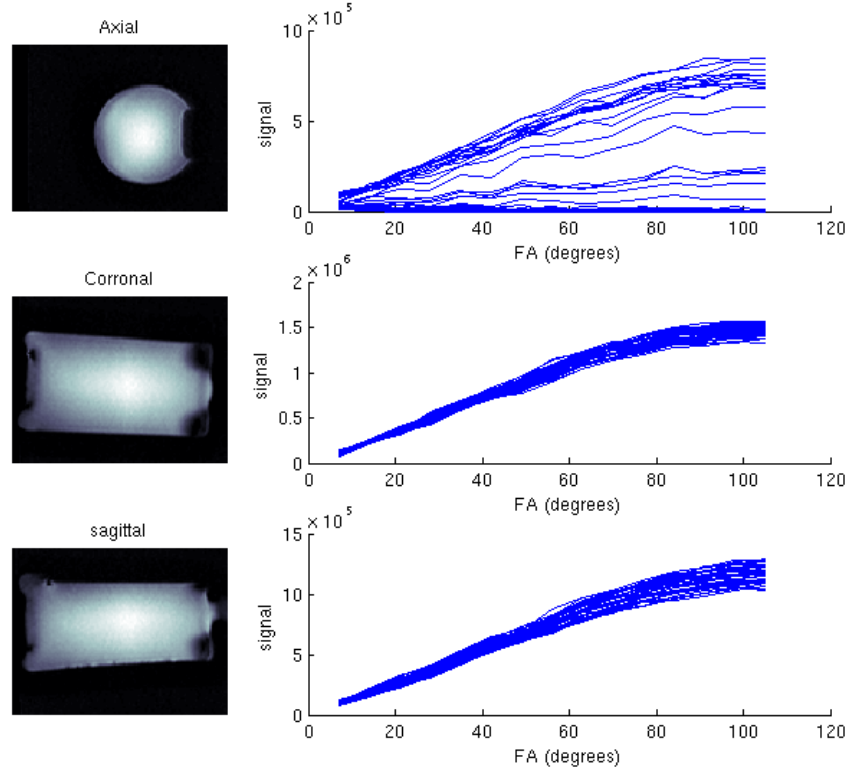
Figure 6.13: *Diagram represent the imaging setup for 7T Philips Achieva system*

For comparison, images of the same phantom was obtained with T/R Philips Volume head coil using the same imaging parameter and Survey. Figure 6.14 shows images for axial and saggital slices for comparing the performance of ETWG to the T/R Philips volume coil. The ETWG shows a good performance as a transmit coil in comparison to other travelling wave devices. However, the ETWG draws more power from the amplifier in comparison to the conventional RF coil.

The same imaging setup was modelled using the xFDTD software to calculate maximum 10 gm average SAR values scaled to 1 Watt input power. Hence, calculate SAR safety parameter K_{sar} for a reference B_1 value. The maximum 10 gm average SAR value is 2.72×10^{-2} Watt/kg gives $K_{sar} = 1.8\,Watt/kg \cdot \mu T$ for $B_1 = 0.123\,\mu T$. Figure (6.14(e) and 6.14(f)) show the B_1^+ distribution in

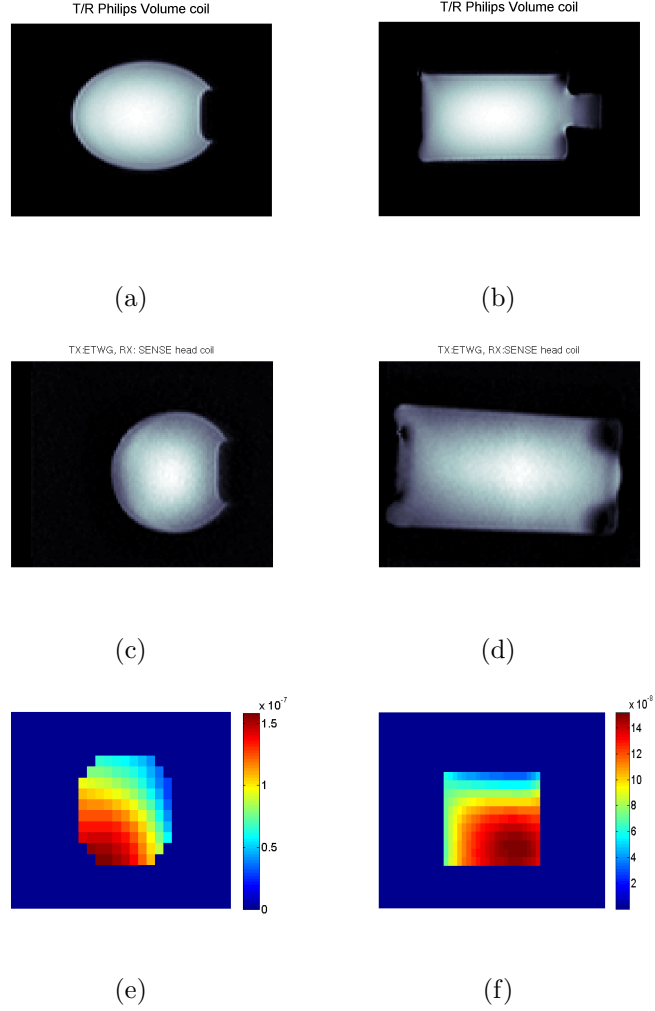the same phantom normalized to 1 Watt input power.

Figure 6.14: *Top: images of the phantom obtained with T/R Philips Volume head coil; top left (a): axial slice, and top right (b): Sagittal slice. Middle images are for the same phantom with ETWG as transmitter and Philips head receiver coil; middle left image (c): Axial images, middle right image (d): sagittal slice. Bottom images are the xFTDT simulation images for the same wrist phantom; bottom left (e) is for an axial image through the phantom and bottom right (f) is for a sagittal slice through the phantom*

6.5.6 SAR and Power Flow Calculations for a Body Model

The end tapered wave guide ETWG is a travelling wave device. Hence, a different approach will be considered in order to assess it's safety level. Different xFDTD simulations were carried out with the waveguide moved closer to the body in the anterior-posterior direction. For each simulation at each distance, rotational B_1 fields were calculated at a reference point in a coronal slice 3 cm deep into the abdominal region using matlab code, figure is a schematic description for the body and ETWG showing the direction of waveguide movement.Then, the SAR safety parameter K_{sar} was calculated using equation (6.19) for the software input power. Theses values were used to calculate the safety parameter for a field strength of $5.9\,\mu T$. That is the field strength necessary for tipping spins $90°$ with a 1 ms rectangular RF pulse. Finally, the energy deposition into the body for 120 RF pulse/second is calculated and averaged over 6 min time, where each RF pulse is of 1 ms duration. Table 6.4 shows SAR calculations at several distance from the body. The xFDTD calculations are based on linear drive excitation while the end tapered waveguide is driven in quadraturare. In quadrature excitation only half of the power is required. Therefore, for the designed ETWG only half of SAR values will be considered and compared to the standard SAR limit, 10 W/kg average over 6 min time. The table shows that positioing the ETWG at a distance between 3 and 5 cm yields SAR at about the safety level of 10 W/kg and that reducing the number of the RF pulses to less than 120 pulses will bring the values to below 10 W/kg. Figure 6.16, top row shows a plot of the driving port impedance, both real and imaginary values, as the waveguide moves closer to the body in the anterior-posterior direction. bottom row: shows the power flow through a coronal plane at 3 cm depth into abdominal region as the waveguide brought

to proximity to the body as well as SAR values normalized to the standard 10 gm average SAR value (10 W/kg). The plots indicate a weak coupling between the waveguide and body with distance. At 5 cm away from the body, the real impedance is $18.95\,\Omega$ and the imaginary value is $49.96\,\Omega$. Looking into the bottom plot it is clear that this reflects back on the power flow and normalized SAR values where this distance gives the maximum power flow and minimum SAR. The plot also shows that the waveguide can be brought to as close as 3 cm with out exceeding the standard limits. However, the large fluctuation of the impedance values at a small distance such as 6 cm causes concern as to the available distance for moving the waveguide in the anterior-posterior direction. The next section will introduce a possible solution for controlling the variation in impedance by introducing an adjustment to the existing design.
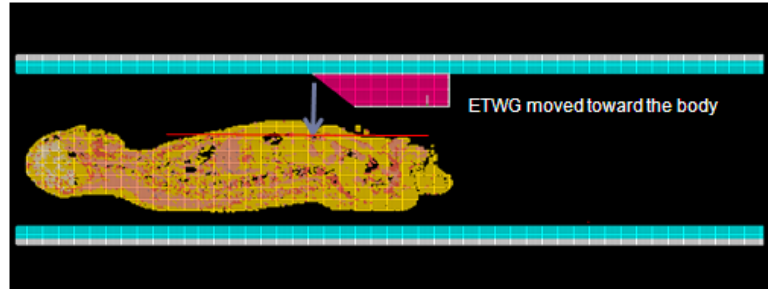

Figure 6.15: *Shows the direction of the ETWG movement inside the magnet bore.*

Distance (cm)	$SAR_{10gm} \times 10^{-4}$ W/kg	$B_1^+ \times 10^{-3}$ μT	K_{sar} $W/kg/\mu T^2$	$SAR_{120pulse}$ W/kg
2	4.498	6.278	11.4134	47.6761
3	1.365	9.58	1.4882	6.2164
4	3.43	10.55	3.0817	12.8728
5	7.96	14.99	3.5432	14.8007
6	1.142	2.391	19.9759	83.4434

Table 6.4: *SAR calculations for end tapered waveguide at different distances.*
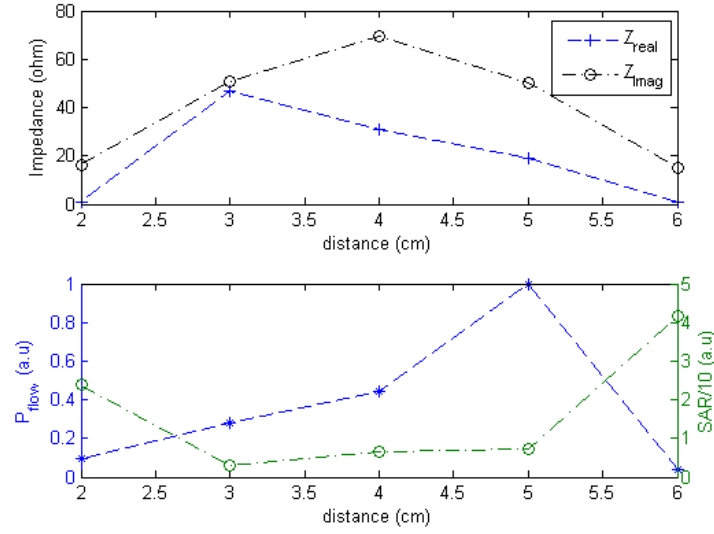
Figure 6.16: *Top: the real and imaginary impedances for the ETWG as a function of distance; Bottom: the power flow and normalized 10 gm SAR values for the ETWG as a function of distance*

6.6 Wave Guide design for local Imaging: Further Optimization

The magnet bore can be considered as a circular wave guide partially loaded with heterogeneous load (body). Therefore, the waveguide impedance varies at different location in the magnet bore and is difficult to calculate explicitly. Reflections might occur near the excitation device and at the imaged body part as a result of mode impedance mismatching. It is believed that there could be an impedance miss-match between the magnet bore mode impedance and the excitation waveguide (ETWG) mode impedance which in turn affect the electromagnetic transition to the waveguide. Figure 6.17 shows the TE_{11} mode distribution in three different cases; the magnet bore unloaded, the magnet bore loaded with spherical phantom and, the magnet bore loaded with the body model. The figure shows how the complexity of the TE_{11} increases as

more complex loads are introduced to the magnet bore and, hence the mode impedance. In this section, xFDTD is used to assess the feasibility of improving the end tapered waveguide for best power transmission and SAR reduction. In order to do that, three different simulations were used. All three have the same magnet bore geometry described in subsection (6.5.1). The magnet bore is loaded with a circular phantom of 20 cm diameter, ($\varepsilon_r \approx 60$, $\sigma \approx 0.5$ S/m). In the first setup, the end tapered waveguide (ETWG) was used as an excitation wave guide; it was positioned so that the tip of the waveguide is 5.5 cm away from the phantom. In the sceond setup, the tapered end of the waveguide was removed to give a circular exit waveguide (CWG) of 22.5 cm long. The phantom was positioned 11 cm away from the opening of the excitation circular waveguide. In the third setup, a dielectric transformer, ($\varepsilon_r \approx 21.5$, $length = 5\,cm$), was attached to the circular waveguide (CWG) to give a circular waveguide with transformer (CWGT). The phantom was positioned 6 cm away from the transformer. Figure 6.18 shows the geometry of the three systems.
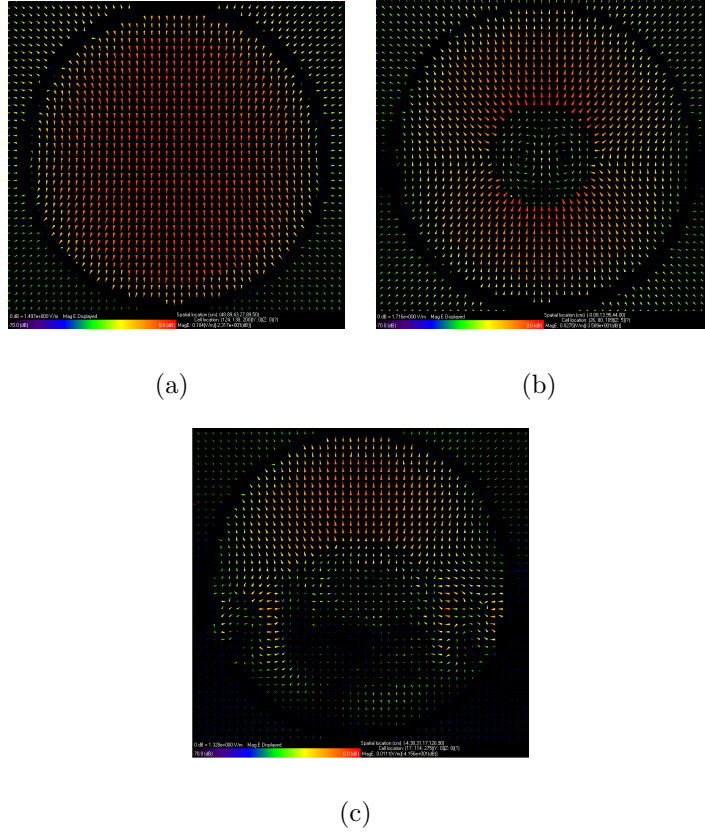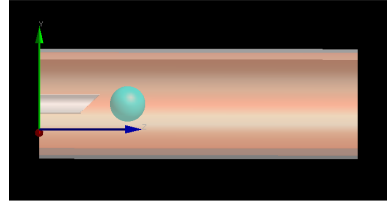
(a)

(b)

(c)

Figure 6.17: TE_{11} *mode distribution: (a) in unloaded magnet bore; (b) in a loaded magnet bore with spherical phantom and (c) in the magnet bore loaded with HUGO body model.*
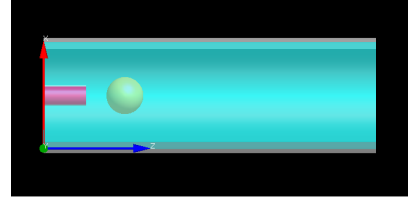
(a) First Setup - ETWG   (b) Second Setup - CWG
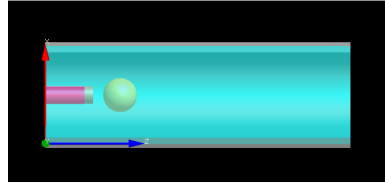
(c) Third Setup - CWGT

Figure 6.18: *The geometry of the three different simulations: (a) end tapered waveguide (ETWG); (b) circular waveguide (CWG); (c) circular waveguide with transformer (CWGT).*

6.6.1 Simulations Results: Impedance Matching, Power flow and SAR

Table 6.5 shows both real and imaginary impedance values, normalized power flow through a central plane and SAR values normalized to 10 W/kg. The mismatch between the mode impedances between both waveguides, magnet bore and excitation waveguide reflects back on the waveguide driving port impedance. Therefore, the port impedance is considered as a measure of how well the two mode impedances are matched.

Graph 6.19(a) shows that TE_{11} mode impedances change for all three systems, the end tapered wave guide shows an impedance mismatch between the excitation waveguide wave impedance and the magnet bore impedance although the waveguide was tapered to gradually introduce the end tapered impedance to the magnet bore. Using a circular waveguide improves the matching. However, the matching can be improved further by introducing a dielectric transformer. The dielectric value is simulated a set of values as the magnet bore impedance is very difficult to calculate analytically.

The graph 6.19(b) shows that the circular waveguide (CWG) with impedance transformer has a maximum power flow and a minimum SAR value of less than 10 W/kg. The end tapered WG has a minimum power flow while the SAR value is about 3 times greater than the standard 10gm avg. SAR. Figure (6.20(a) to 6.20(e)) shows the field maps for a slice passes the centre of the phantom for all three set-ups. The end tapered WG, figure 6.20(a), has the highest B_1 produced for 1 Watt input power while the lowest value is for waveguide with no transformer, see figure6.20(c), and, almost half of the B_1 field is generated for the circular waveguide with transformer, see figure6.20(e). Figure 6.20(b,d,f) show 1 gm SAR maps for the same central slice scaled to 1 Watt for all the three simulations. A central point on all the three maps has

been chosen to compare SAR values for all set-ups. The circular waveguide without transformer have the lowest value of 0.0043 W/kg. This is due to the miss-matching between the CWG and magnet bore. The circular waveguide with transformer is 0.0184 W/kg lower than the end tapered waveguide.

	Z_{Re}	Z_{Im}	Normalized P_{flow}	Normalized SAR
	Ω	Ω	a.u.	a.u.
ETWG	2.394	-7.1	0.1839	2.972
CWG	9.166	20.4	0.1485	2.385
CWGT	39.05	10	0.9998	0.8412

Table 6.5: *Real and Imaginary impedances ; normalized power flow and; normalized SAR*
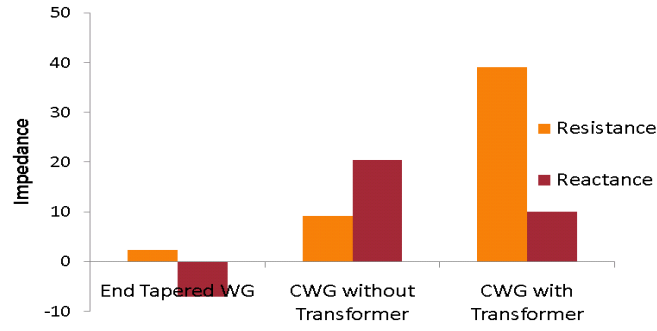
(a)
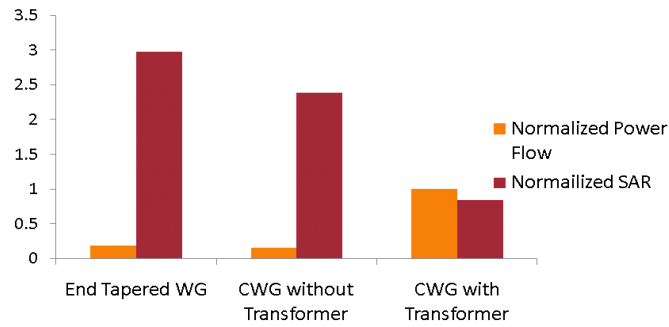
(b)

Figure 6.19: *Charts for the three set up 6.19(a) shows real and imaginary components of the excitation ports' Impedances; 6.19(b) shows the power flow across a 3cm depth coronal slice verses the normlalized SAR values to a reference B_1 field point at the same plane.*
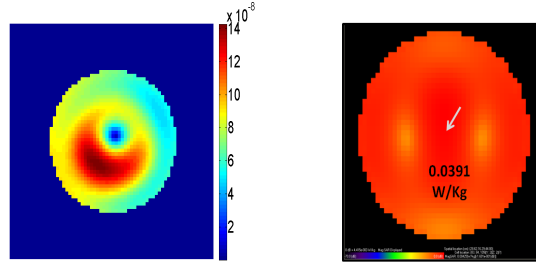
(a) ETWG - $|B_1^+|$ (b) ETWG - 1gm SAR
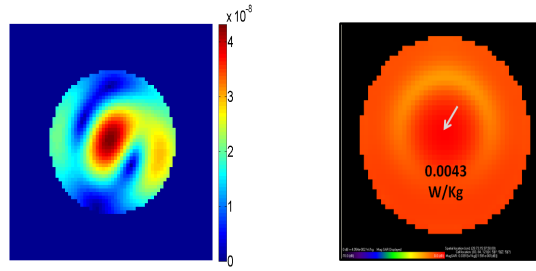
(c) CWG - $|B_1^+|$ (d) CWG - 1gm SAR
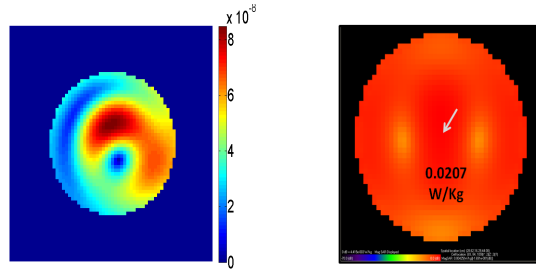
(e) CWGT - $|B_1^+|$ (f) CWGT - 1gm SAR

Figure 6.20: *Top Three images are the simulated $|B_1^+|$ field maps for all three systems for 1 Watt input power: (a) end tapered WG, (c) circular WG and, (e) circular WG with transformer; the three bottom images are the 1gm SAR maps scalled to 1Watt input power: (b) for end tapered WG, (d) circular WG and, (f) circular WG with transformer.*

6.6.2   Circular Waveguide Antenna and Transformer Coupling to body model

Loading the magnet bore with different loads changes the magnet bore impedance; for example, the transformer that used to match a 20 cm diameter phantom no longer matches the excitation wave guide to the body. Therefore, in this section we used different xFDTD simulations using a range of dielectric values to match the excitation waveguide to the body.

The same system setup used in previous sections is used. The magnet bore is of 58 cm diameter and 190 cm length. The 7T bed and the bore casing is modelled as a 50 cm diameter cylinder and dielectric of 2.5 . The scanner loaded with the 5 mm grid standard body model. The total grid size was of $164 \times 164 \times 415$ cells.

The excitation wave guide is of 10 cm diameter and 22.5 cm long load with dielectric material of $\varepsilon_r \approx 54$. The waveguide positioned at about 7 cm distance above the abdominal region, just next the top of the bore. It was driven by 1 volt, 50 Ω and, 298 MHz sinusoidal voltage. A transformer of about 5 cm long was attached to the opening of the excitation waveguide. Different simulations were done for a range of dielectric values($\varepsilon_r \approx 3.2, 7, 10, 12, 13, 14 \, and \, 22.5$) to find the best impedance matching. This method is used because the magnet bore is a circular wave guide loaded with highly inhomogeneous dielectric (body) and it wave impedance is difficult to calculate explicitly.

The power flow across a coronal plane at 3 cm depth in the abdominal region is calculated using equation (6.14). SAR values for 120 (1 ms)RF pulse averaged over 6 min time were also calculated to a reference B_1 field at the same coronal plane. The SAR values then normalized to the standard 10 W/kg value.

## 6.6.3 Simulation Results: Impedance Matching, Power Flow and SAR

Figure 6.21(a) shows excitation port impedance changes with transformer dielectric, this is an indication of how well the excitation waveguide mode impedance is matched to the body loaded magnet bore mode impedance when using a specific dielectric. The best impedance matching is for ($\varepsilon_r \approx 14$). The matching is also acceptable around this values, for the range ($\varepsilon_r \approx 7\,to\,14$); however, for extremely low and high ($\varepsilon_r \approx 3.2\,and\,22.5$) values there is a high mismatching. In comparison to that, the power flow and SAR values follow an opposite trend to each other as the dielectric values change. At ($\varepsilon_r \approx 14$), the power flow is high and normalized SAR has the lowest value, this continue for a range of values, ($\varepsilon_r \approx 7\,to\,14$). For transformers with, ($\varepsilon_r \approx 3.2$) and ($\varepsilon_r \approx 22.5$), SAR values are high while power flow values are low.

In order to gain more insight in to how well the transformer is coupling with body, the transformer, ($\varepsilon_r \approx 14$), with the best matching, used to carry out different xFDTD simulations with the excitation waveguide moved closer toward the body at distances of 2, 3, 4, 5, 6 cm. Figure 6.22(a) shows how the impedance changes as the excitation wave guide move closer to the abdominal region over total distance of 6cm for a transformer with ($\varepsilon_r \approx 14$). The real resistance varies between 60 and 80 Ω and, the reactance varies between 14 and 30 Ω. This shows that the transformer coupled waveguide is better suited to the body in comparison to the ETWG in Figure 6.16. Figure 6.22(b) shows that SAR values at about the recommended value over a distance of 4 to 5.5 cm away from the body while it is about 4.5 the recommended value at a close distance of 2 cm. In comparison to that, the normalized power flow are of high values between 0.89 a.u and 0.81 a.u at the rang of distance between 4 and 5.5 cm. Moreover, positioning the excitation waveguide at 6 cm distance gives

1.22 times the standard SAR values and 0.91 times the maximum power flow.
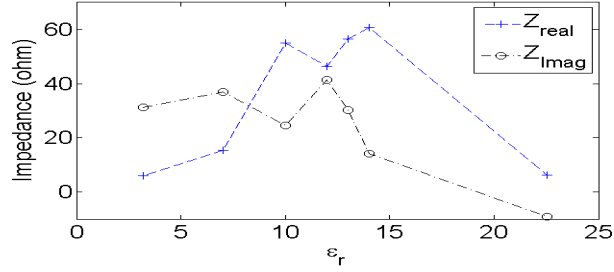
(a) Impedance Matching
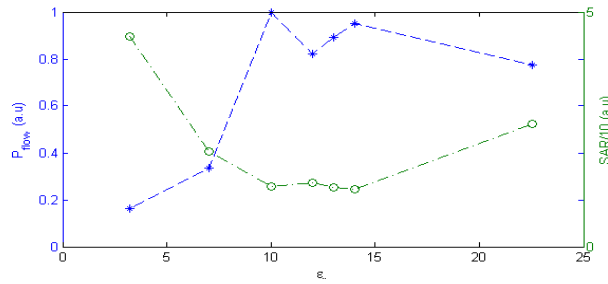
(b) Power flow and SAR

Figure 6.21: *Circular waveguide with different dielectric transformers: (a) Impedance matching: real and imaginary impedance for different dielectric transformers values; (b) Normalized power flow across a coronal slice and normalized SAR for different transformer values.*
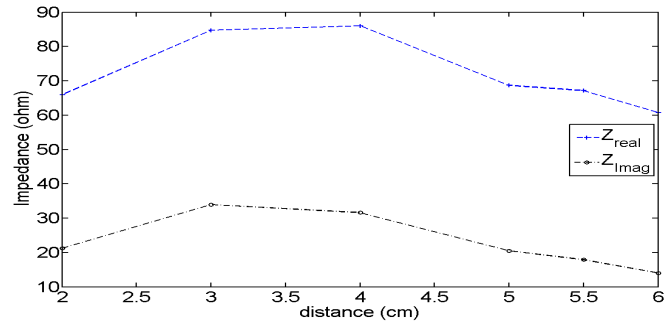
(a) Impedance Matching
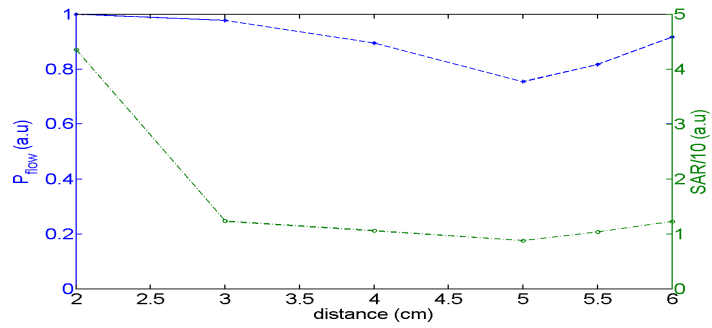
(b) Power flow and SAR

Figure 6.22: *Circular waveguide with a dielectric transformer moved toward the body:(a) Impedance matching: real and imaginary impedance as a function of distance; (b) Normalized power flow across a coronal slice and normalized SAR values as a function of distance.*

6.7 Summary

In this chapter the xFDTD Bio Pro software (Remcom Inc.) was used to investigate the travelling wave MRI. First, a patch antenna was designed and the effect of having different matching loads on improving brain imaging was investigated. Four different matching loads with three different dielectric values (43.5, 54.5 and 60) were positioned between the head and the patch antenna. They are: a cylinder, tapered cylinder, mask, and mask with tapered cylinder. It was found that using a mask with tapered cylinder had resulted in the higher uniformity, low SAR value and high power flow value across two different head slices.

Second, an end tapered waveguide (ETWG) was designed for local imaging, especially abdominal and cardiac imaging. The ETWG was first assessed using the xFDTD software for B_1 field maps, power flow, field uniformity and SAR values. It was found that the ETWG can be brought to as close as 3 cm to the body without exceeding the safety limit for 120 RF pulses at a duration of 1 ms and averaged over 6 min time. A proto-type of the ETWG was built with quadrature drive ports. Two quarter wavelength cables and matching circuits were used to match the antenna to the 50 Ω cable. The ETWG was then tested on 7T Acheiva system to image a cylindrical phantom. The system the calibrated to achieve a 90° flip angle images.

For further optimisation a circular waveguide with transformer dielectric. The circular waveguide is of the same dimensions as the ETWG but with the tapered end removed. The transformer dielectric is 5 cm long and have the values ($\varepsilon_r \approx 3.2, 7, 10, 12, 13, 14 \, and \, 22.5$). Looking into the excitation port impedance, power flow and SAR values, it was found that the better the impedance matching the higher the power flow and the lower the SAR value. Moreover, a range of dielectric between 7 and 14 was found to be suitable for

different body masses where best results are given at a dielectric value of 14. It was found that circular waveguide with transformer can be brought as close as 4 cm to the body without exceeding the safety limit for 120 RF pulses at a duration of 1 ms and averaged over 6 min time.

Bibliography

[1] David O. Brunner, Jan Paska, and Klaas P. Pruessmann. Travelling-wave: Initial results of in-vivo head imaging at 7 t. In *Proc. Intl. Soc. Mag. Reson. Med.*, volume 17, page 500, 2009.

[2] David O. Brunner and Klaas P. Pruessmann. Reciprocity relations in travelling wave mri. In *Proc. Intl. Soc. Mag. Reson. Med.*, volume 17, page 2943, 2009.

[3] David O. Brunner, Nicola De Zanche, Jrg Frhlich, Jan Paska, and Klaas P. Pruessmann. Travelling-wave nuclear magnetic resonance. *Nature*, (457):994–998, 2009.

[4] Robert E. Collin. *Field Theory of guided Waves.* IEEE, 1991.

[5] W. Mao, M. B. Smith, and C. M. Collins. Exploring the limits of rf shimming for high-fields mri of the human head. *Magn. Res. Imaging*, 156:918–922, 2006.

[6] K. F. Sander and G. A. Reed. *Transmission and propagation of electromagnetic waves.* Cambridge University Press, second edition edition, 1986.

[7] G. Wiggins, B. Zhang, Q. Duan, and D. K. Sodickson. Travelling-wave imaging of the human head at 7 tesla: Assessment of snr. homogeneity and b_1^+ efficiency. In *Proc. Intl. Soc. Mag. Reson. Med.*, volume 17, page 2942, 2009.

Chapter 7

Conclusions

The work presented in this thesis was to investigate feasibility of overcoming the in-homogeneity issues through controlling each excitation element independently in an RF coil. The focus in this work was first to use electromagnetic simulations, full wave methods, in combination with a standard regularization technique to predict the optimal shimming for volume coils. The second part of the thesis focused on the travelling wave MRI approach as a novel method which brought promises to overcoming high field MRI homogeneity issues. This chapter analyses the work that has been done and describes the potential further work on this project.

7.1 Optimisation of Elementary Drive Currents Elements for RF Coils

Transmission Line Modelling (TLM) in-house software was used in combination with the Tikhonov regularisation method for determining the optimal drive RF shimming currents. In 2-dimensional problem, 8 and 16 rungs birdcage-like coils were modelled and optimisation have been done using four different proposed target fields for four different head slices. The 2-dimensional

results show that there is an overall improvement in uniformity for all four slices. However, the optimal currents' amplitude show a three to four times increase in some of the drive elements where the majority kept at about their original values. Taking into consideration the fact that the 2-dimensional problem does not fully represent a physical RF coil, the work progressed to 3-dimensional modelling and optimisation.

The 3-dimensional 8 and 16 rungs birdcage-like coil were modelled and, results were compared to that of 32 and 64 multi-elements coils. The optimisation was done first for four selective head slices. The results show that as the number of drive elements increases, the field homogeneity improved largely with shimming; however, this is done at the expense of more current drawn for some elements.

The optimisation was carried out next for a region of interest for high field uniformity and low SAR values. The 8 and 16 rungs birdcage-like optimisation did not give the expected result, the regularised rotational fields and SAR maps deteriorated as a result of the optimal regularised parameter values poor fitting. The L-curve plots did not shows a defined L-curve and hence results have been affected. However, the 32 and 64 multi-elements coils did show an improvement in the magnetic field distribution and reduction in SAR values in agreement with the selective slice optimisation but also at the expense of high current in some of the elements. Moreover, it was found that the current draw for both coils is for elements that have the same physical position on the coil. To conclude, using Tikhonov regularisation method for optimal shimming improves field uniformity and reduce SAR values but it is recommended to be used in conjunction with inverse design algorithm to optimise coil shape to minimum current draw for a practical use. Moreover, it is believed that combining the RF shimming with pulse design for low SAR values and high field uniformity is more effective.

7.2   Travelling Wave MRI for 7T System

The travelling wave MRI approach has been investigated in this work as a novel method for ultra-high systems, 7T systems in particular. The xFDTD method was used to model coupling between a body loaded magnet bore and patch antenna. Four different matching loads have been introduced to investigate the possibility of maximising the power flow toward the head with high uniformity at low SAR values. These are: cylindrical dielectric match, tapered cylinder, mask and mask with tapered cylinder with three different dielectric values (43.5, 54.5 and 60). It was found that introducing a mask with tapered cylinder improves homogeneity and has the highest power flow and relatively low SAR value. However, having such a system set up is not appropriate for practical use and it is restricted for only the extreme ends of the magnet bore due to the patch antenna size.

The End Tapered Wave Guide have been designed for localised imaging volumes. The feasibility of the design was conducted first in simulations before it was bench tested. The End Tapered Wave Guide was then experimentally evaluated with a cylindrical phantom and the coil parameters in the 7T scanner was set up for the travelling wave imaging. It is found that power optimisation and calibration for travelling wave devices is more difficult to achieve than the conventional coils as they draw more power. The travelling wave devices excite fields in magnet bore as a whole while in conventional coils spins is excited in a confined region of interest only. Nevertheless, the end taper waveguide small size give it the virtue of being the most flexible travelling wave device for RF transmitting to any part of the body, especially, the cardiac and abdominal region. A four element array coil was designed in order to be used as a receive coil with the end tapered waveguide for body imaging. The array coil can be used for wrist and knee imaging as well as its geometric flexibility to be used

as an abdominal receive array coil. The design of this coil is outside the scope of this thesis.

Adjusting the end tapered waveguide to a circular waveguide with transformer simulation results show that optimising the waveguide coupling will reduce the power to deliver a 90^0 flip angle. Moreover, a range of dielectric values between 7 and 17 is proven to give a good mode impedance matching between the circular waveguide and the magnet bore. This added an extra degree of freedom in term of the body size to be imaged with such devices. Therefore, it is recommended to put this new development into practice for body imaging and test it against the simulation results and end tapered waveguide.

The end tapered wave guide also can be adopted to a multi-transmit MRI system to form a travelling wave MRI parallel transmit system. The 7T magnet bore can accommodate up to three waveguide of the size designed in this thesis. The number of the waveguide can always increases by designing smaller size waveguides. However, this depends on the availability of the dielectric material used in the design. Using such a system is believed to provide a uniform flip angle maps over a large field of view.

Bibliography

[1] *Fundamental of physics.* New York: John Wiley and Sons, 1974.

[2] *NMR Probeheads for Biophysical and Biomedical Experiments.* Imperial College Press, 2006.

[3] Technical Report IEC 60601-2-33:2002. Medical electrical equipment part 2-33: Particular requirement for the safety of magnetic resonance equipment for medical diagnosis. Technical report, International Electrotechnical Commission, 2002.

[4] David O. Brunner, Jan Paska, and Klaas P. Pruessmann. Travelling-wave: Initial results of in-vivo head imaging at 7 t. In *Proc. Intl. Soc. Mag. Reson. Med.*, volume 17, page 500, 2009.

[5] David O. Brunner and Klaas P. Pruessmann. Reciprocity relations in travelling wave mri. In *Proc. Intl. Soc. Mag. Reson. Med.*, volume 17, page 2943, 2009.

[6] David O. Brunner, Nicola De Zanche, Jrg Frhlich, Jan Paska, and Klaas P. Pruessmann. Travelling-wave nuclear magnetic resonance. *Nature*, (457):994–998, 2009.

[7] J. Chen, Z. Fen, and J. Jin. Numerical simulation of sar and b_1-field inhomogeneity of shielded rf coils loaded with the human head. *Mag. Reson. Med.*, 45(5):690–695, 1998.

[8] N. Chen, D. I. Hoult, and V. I. Sank. Quadrature detection coils - a further improvement in sensitivity. *J. Magn. Reson.*, 54:324–327, 1983.

[9] C. Christopulous. *The Transmission-Line Modelling (TLM) Method in Electromagnetics.* Morgan and Claypool Publishers, 2006.

[10] Robert E. Collin. *Field Theory of guided Waves.* IEEE, 1991.

[11] C. M. Collins, S. Li, and M. B. Smith. Spatial resolution of numerical models of man and calculated specific absorption rate using the fdtd method: A study at 64 mhz in a magnetic resonance imaging coil. *Journal of Magnetic Resonance Imaging*, 40:847–856, 1998.

[12] C. M. Collins, W. Liu, J Wang, R. Gruetter, T Vaughan, K. Ugurbil, and M. B. Smith. Temperature and sar calculations for a human head within volume and surface coils at 64 and 300 mhz. *Journal of Magnetic Resonance Imaging*, 19:650–656, 2004.

[13] C. M. Collins and M. B. Smith. Calculations of b_1 distribution, snr and sar for a surface coil adjacent to an anatomically-accurate human body model. *Mag. Reson. Med.*, 45:692–699, 2001.

[14] C. M. Collins and M. B. Smith. Spatial resolution of numerical models of man and calculated specific absorption rate using the fdtd method: A study at 64 mhz in a magnetic resonance imaging coil. *J. Magn. Reson. Imag.*, 18:383–388, 2003.

[15] Federal Communications Commision. Tissue dielectric properties. http://www.fcc.gov/oet/rfsafety/dielectric.html.

[16] A. H. Compton and O. Rognley. Is the atom the ultimate magnetic particle. *Phys. Rev.*, 16:464–476, 1921.

[17] P. J. Dimbylow and S. M. Mann. Sar calculation in anatomically realistic model of the head for mobile communication transceivers at 900mhz and 1.8ghz. *Phys. Med. Biol.*, 39:361–368, 1994.

[18] R. Gabillard. Measurement of relaxation time t_2 in the presence of an

inhomogeneity in the magnetic field more important than the width of the line. *C. R. Acad. Sci.*, 232:1551–1552, 1951.

[19] C. Gabriel and S. Gabriel. Compilation of the dielectric properties of body tissues at rf and microwave frequencies. Technical report, United States Air Force, 1996.

[20] O. P. Gandhi and J. Y. Chen. Numerical dosimetry at power-line frequencies using anatomically based models. *Bioelectromagnetics*, 1:43–60, 1992.

[21] O. P. Gandhi, G. Lazzi, and C. M. Furse. Electromagnetic absorption in the human head and neck for telephone at 835 and 1900 mhz. *IEEE Transactions on Microwave Theory and Techniques*, 44:1884–1897, 1996.

[22] P. Hagmann, L. Jonasson, P. Maeder, J. Thiran, V. Wedeen, and R. Meuli. Understanding diffusion mr imaging techniques: From scaler diffusion-weighted imaging to diffusion tensor imaging and beyond. *RadioGraphics*, 26:S205–S223, 2006.

[23] P. C. Hansen. Analysis of discete ill-posed problems by means of the l-curve. *SIAM Rev.*, 34(4):561–580, 1992.

[24] P. C. Hansen. The l-curve and its use in the numerical treatment of inverse problems. In *in Computational Inverse Problems in Electrocardiology, ed. P. Johnston, Advances in Computational Bioengineering*, pages 119–142. WIT Press, 2000.

[25] P. C. Hansen. Regularization tools: A matlab package for analysis and solution of discrete ill-posed problems. Technical Report version 4, Informatics and Mathmatical Modelling, Technical University of Denmark,DK-2800, Lyngby, Denmark, 2007.

[26] W. N. Hardy and L. A. Witehead. Split-ring resonator for use in magnetic resonance from 200-2000 mhz. *Rev. Sci. Instrum.*, 52:213–216, 1981.

[27] W. N. Hardy and L. A. Witehead. A double- tuned probe for metabolic nmr studies. *Mag. Reson. Med.*, 23:367–371, 1992.

[28] Roger F. Harrington.

[29] C. E. Hayes, W. A. Edelstein, W. A. Schenck, O. M. Mueller, and M. Eash. An efficient, highly homogeneous radiofrequency coil for whole-body nmr imaging at 1.5t. *J. Magn. Reson.*, 63:622–628, 1985.

[30] W. E. Heinz, H. Martin, and N. Andreas. *Regularization of Inverse Problems.* Kluwer Academic Publisher, Netherlands, 2000.

[31] D. I. Hoult. The principle of reciprocity in signal strength calculations: a mathematical guide. *Conc. Magn. Reson.*, 12(4):173–187, 2000.

[32] D. I. Hoult and R. Deslauriers. A high-sensitivity, high-b_1 homogeneity probe for quantitation of metabolites. *Mag. Reson. Med.*, 16:411–417, 1990.

[33] D. I. Hoult and R. E. Richards. The signal-to-noise ratio of the nuclear magnetic resonance experiment. *J. Magn. Reson*, 24:71–85, 1976.

[34] Scott A. Huttel, Allen W. Song, and Gregory McCarthy. *Functional Magnetic Resonance Imaging.* Sinauer Associates Inc., second edition edition, 2009.

[35] T. S. Ibahim, R. Lee, B. A. Baertlein, A. Kangarlu, and P. M. L. Robitaille. Comparison between linear, quadrature and 4-port excitations from 1.5 t to 4.7 t. ISMRM, 1999.

[36] T. S. Ibrahim, R. Lee, B. A. Baertlein, A. Kangarlu, and P. L. Robitaille. Application of finite difference time domain method for the design of birdcage rf head coils using multi-port excitations. *Magn. Res. Imaging*, 18:733–742, 2000.

[37] J. Jevtic. Ladder networks for capacitive decoupling in phased-array coils. 2001.

[38] J. Jin and J. Chen. On the sar and field inhomogeneity of birdcage coils loaded with human head. *Mag. Reson. Med.*, 38:953–963, 1997.

[39] J. M. Jin, J. Chen, W. C. Chew, H. Gan, R. L. Magin, and P. J. Dimbylow. Computation of electromagnetic fields for high-frequency. *J. Magn. Reson. Imag.*, 40:847–856, 1998.

[40] A. Kangarlu, T. Ibrahim, and F. Shellock. Effects of coil dimensions and field polarization on rf heating inside a head phantom. *Magn. Res. Imag.*, 2005.

[41] U. Katscher, P. Boerner, C. Leussler, and J. S. Van den Brink. Transmit sense. *Mag. Reson. Med.*, 49:144–150, 2003.

[42] A. Kumar, D. Welti, and R. R. Ernst. Nmr fourier zeugmatography. *J. Magn. Reson*, 1975.

[43] P.C. Lauterbur, D.M. Kramer, W.V. House, Jr., and C.-N. Chen. Zeugmatographic high resolution nuclear magnetic resonance spectroscopy. images of 243 chemical inhomogeneity within microscopic objects. *J. Am. Chem. Soc.*, 97:6866–6868, 1975.

[44] L. Libby. Special aspects of balanced shielded loops. In *Proceeding of the I. R. E. and Waves and Electrons*, pages 641–646, 1945.

[45] F. Liu, B. L. Beck, J. R. Fitzimmons, S. J. Blackband, and S. Crozier. A theoretical comparison of two optimization methods for radiofrequency drive schemes in high frequency mri resonators. *Physics in Medicine and Biology*, 50:5281–5291, 2005.

[46] Arthur W. Magill. *Ultra-High Frequency Magnetic Resonance Imaging.* PhD thesis, School of physics and Astronomy, University of Nottingham, 2006.

[47] P. Mansfield. Multi-planar image formation using nmr spin echoes. *J. Phys. C. Reson*, 1977.

[48] P. Mansfield and P. K. Grannell. Nmr 'diffraction' in solids? *J. Phys. C*, 6:L422–L426, 1973.

[49] W. Mao, M. B. Smith, and C. M. Collins. Exploring the limits of rf shimming for high-fields mri of the human head. *Magn. Res. Imaging*, 156:918–922, 2006.

[50] W. Mao, Z. Wang, M. B. Smith, and C. M. Collins. Note: Calculation of sar for transmit coil arrays. *Concepts in Magnetic Resonance Part B*, 31B:127–131, 2007.

[51] J. Mispelter, M. Lupu, and A. Bringuet. *NMR probheads for biophysical and biomedical experiments: theoretical principles and practical guidelines.* Imperial College Press, 2006.

[52] M. A. Ohliger and D. K. Sodickson. An introduction to coil array design for parallel mri. *NMR in Biomedicine*, 19:300–315, 2006.

[53] J. Paul, C. Christopoulos, and D. Thomas. *A 3-D time-domain TLM electromagnetic field solver: regSolve.cc.* The George Green Institute for Elec-

tromagnetics Research (GGIEMR), School of Electrical and Electronic Engineering, University of Nottingham, 2000. In house manual.

[54] W. Pauli. Zur frage der theoretischen deutung der satelliten einiger spektrallinien und ihrer beeinflussung durch magnetische felder. *Die Naturwiessenschaften*, 12:741, 1924.

[55] R. G. Pinkerton, E. A. Barberi, and R. S. Menon. Noise properties of a nmr transceiver coil array. *J. Magn. Reson.*, 171:151–156, 2004.

[56] K. P. Pruessmann, M. Weiger, M. B. Scheidegger, and Peter Boesiger. Sense: Sensitivity encoding for fast mri. *Mag. Reson. Med.*, 42, 1999.

[57] E. M. Purcell, H. C. Torrey, and R. V. Pound. Resonance absorption by nuclear magnetic moments in a solid. *Phys. Rev.*, 69:37–38, 1946.

[58] Simon Ramo, John R. Whinnery, and Theodore Van Duzer. *Fields and Waves in Communication Electronics*. John Wiley and sons Inc., 1994.

[59] P. B. Roemer, W. A. Edelstein, C. E. Hayes, S. P. Souza, and O. M. Muller. The nmr phase array. *Mag. Reson. Med.*, 16:192–225, 1990.

[60] Matthew N. O. Sadiku. *Numerical Techniques in Electromagnetics*. CRC Press, 2001.

[61] K. F. Sander and G. A. Reed. *Transmission and propagation of electromagnetic waves*. Cambridge University Press, second edition edition, 1986.

[62] H. J. Schneider and P. Dullenkopf. Slotted tube resonator: A new nmr probe head at high observing frequencies. *Rev. Sci. Instrum.*, 48:68–73, 1977.

[63] J. Vaughan, G. Adriany, E. Yacoub, T. Duong, L. DelaBarre, P. Andersen, and K. Ugurbil. A detunable tem volume coil for high field mri. *Mag. Reson. Med.*, 47:990–1000, 2002.

[64] J. Wang, O. Fujiwara, Sachiko Kodera, and Socichi Watanabe. Fdtd calculation of whole-body average sar in adult and child models for frequencies from 30 mhz to 3 ghz. *Physics in Medicine and Biology*, 51:4119–4127, 2006.

[65] G. Wiggins, B. Zhang, Q. Duan, and D. K. Sodickson. Travelling-wave imaging of the human head at 7 tesla: Assessment of snr. homogeneity and b_1^+ efficiency. In *Proc. Intl. Soc. Mag. Reson. Med.*, volume 17, page 2942, 2009.